ZH-153

FLAPPED HYDROFOILS IN SMOOTH WATER

SUBCAVITATING FLOW

Report submitted to Bureau of Ships
Department of the Navy

GENERAL DYNAMICS | CONVAIR

FLAPPED HYDROFOILS IN SMOOTH WATER SUBCAVITATING FLOW

C. E. Jones, Jr.

November 1961

Report submitted to Bureau of Ships
Department of the Navy

Contract Nonr 3180(00)
Task NR 062-252

GENERAL DYNAMICS | CONVAIR

a correction sheet, Figure 17,

F.V. 11/3/64.

SUMMARY

Results of towing-tank tests on a 4-inch chord, 24-inch span, single-strut mounted, plain-flapped hydrofoil model, having an NACA 16-309 wing section, are reported. The hydrofoil model was constructed to permit tests to be conducted on four flap sizes.

Results are presented in coefficient form. Comparisons are made with aerodynamic data and theory. Results include curves of hydrofoil lift, drag, and pitching moment coefficient; flap normal, and chord force coefficient; hinge moment coefficient; and flap effectiveness.

FOREWORD

This report was prepared by General Dynamics/Convair, under the direction of S. M. Lum of the Bureau of Ships, Department of the Navy.

The experimental part of this study was directed by T. E. Sladek, and the computer programing was accomplished under the direction of J. T. Byrne. A. C. Conolly assisted in data analyzing and presentation of results. The hydrofoil model was manufactured and instrumented by Convair's Low-Speed Wind Tunnel staff. The entire program was performed under the general supervision of H. E. Brooke, Chief of Hydrodynamics. The study was conducted, and the report was written,by C. E. Jones, Jr.

CONTENTS

SUMMARY iii

FOREWORD v

INTRODUCTION 1

MODEL DESCRIPTION AND INSTRUMENTATION 3

Test Facility 3

Model Description 3

Instrumentation 4

TEST PROCEDURES 7

RESULTS 9

Lift 9

Flap Effectiveness 10

Drag 16

Pitching Moment 18

Flap Forces 19

Effect of Speed 22

Lift, Drag, Pitching Moment, With Flaps Cycled 22

CONCLUSIONS 23

BIBLIOGRAPHY 25

SYMBOLS 27

FIGURES 1 THROUGH 56 31

TABLES I THROUGH IV 73

DISTRIBUTION LIST 77

INTRODUCTION

The fully-submerged hydrofoil with zero dihedral has the highest lift-drag ratio of all known hydrofoils. However, the desire to use this type of hydrofoil on large seacraft has pointed to the need for trailing-edge flaps which are necessary for lateral control and pitch control, as well as for reducing sea-state gust loads.

The trailing-edge flap should be regarded as a control device which can cause a seacraft to roll, pitch, or yaw, as the human pilot or mechanical autopilot dictates. This controllability of the flap is a result of a change in the pressure distribution on the wing surface of which the flap is a part. For example, when the trailing-edge flap is deflected downward, the hydrofoil becomes, in essence, a new hydrofoil of increased camber. The increased camber generates a considerable negative pressure increase over the top surface, and an increase in positive pressure over the bottom surface of the hydrofoil. This results in an increase in lift coefficient which causes a change in the balance of the seacraft, and a subsequent angular movement of the craft about one of its axes.

With few exceptions, past seacraft designs have not used flaps. Control problems have caused area-submergence configurations to be favored; therefore, experimental information on flapped hydrofoils is virtually non-existent. The program covered by this report had the following objectives:

1. Obtain experimentally the characteristics of a flapped hydrofoil.
2. Compare experimental results with aeronautical data-theory to determine to what extent aerodynamic data may be used in the design of subcavitating hydrofoils.

In the Results section of this report, brief comments are made on the theory, followed by discussion and comparison of each result. It is pointed out that the comparisons were not always made with theory, as some comparisons were made with empirically-based formulas generally favored by aeronautical designers.

The NACA 16-309 wing section was chosen for this study, based upon the Bureau of Ships specified requirement of supporting approximately 20 percent of the weight of a 100-ton seacraft. The 16-series sections are well-known aerodynamically, for a number of them (including the -309) have been thoroughly documented by computational studies, wind-tunnel tests, and tank tests. They are cambered to a uniform mean line, and their designed minimum pressure position is 60 percent of the chord aft of the leading edge. Consequently, when operating at their design lift coefficient, all members of the 16-series have a uniform chordwise pressure distribution, a feature which makes them well suited for hydrofoils.

The plain trailing-edge flap was recommended for this study because it is the only one which can perform as an aileron capable of deflecting to negative flap angles and, in addition, it is not as susceptible to fouling as the other types. There are others (such as the split type and the zap type) which, although effective in increasing lift, are considered objectionable for subcavitating flow. Ambitious types (such as the Fowler, the slotted, and venetian-blind types), which have promised very high lift increments, involve an increase in effective wing area because they extend rearward when deflected. This feature requires sophisticated mechanical linkage resulting in additional weight and increased maintenance.

MODEL DESCRIPTION AND INSTRUMENTATION

TEST FACILITY

The entire test program was conducted at the Convair Hydrodynamic Towing Tank, which is 300 feet long, 12 feet wide, and 6 feet deep. A description of this tank is given in Reference 1. Figure 1 shows the model mounted on the base of the high-speed carriage.

MODEL DESCRIPTION

The hydrofoil model has an aspect ratio -6 (4 x 24 inches) wing rectangular in planform, with zero dihedral, and with thickness and planform taper ratios of 1.0. Both wing and flaps were made of Armco 17-4 PH stainless steel. A profile sketch of the 16-309 section, and a table of hydrofoil model ordinates, are shown in Figure 2.

The model was constructed to allow the testing of four different flaps which are identified in this report as:

	c_f/c	b_f/b
Model Flap Configuration 1	0.3	0.6
Model Flap Configuration 2	0.3	0.8
Model Flap Configuration 3	0.2	0.6
Model Flap Configuration 4	0.2	0.8

Steel inserts, cut to conform to the hydrofoil wing surface, were fastened to the model wing when it was desired to test configurations having either $c_f/c = 0.2$ or $b_f/b = 0.6$ dimensions. Figure 3 is a photograph of the model mounted on the test bench. The figure shows a flap with a chord insert mounted.

Figure 4 is a schematic of the model installation showing the hydrofoil mounted to a structural strut. This strut served to transmit all of the wing

forces to the strain gage balances mounted at its upper end. The figure also shows an ogive strut fairing enclosing the structural strut. The strut fairing was designed to be mounted directly to the carriage so as not to touch either the structural strut or the model. This method of mounting the strut fairing eliminated strut drag from the drag results.

INSTRUMENTATION

All of the instrumentation necessary to record foil and flap forces, distance, time-analog velocity, and flap position, was mounted directly on the carriage. The main balance of the foil sensed normal force, axial force, and pitching moment. The flap balance sensed normal force, axial force, and hinge moment. All wing and flap forces were measured by means of moment-type strain gages, which were mounted for single-gage readout in order to minimize gage interaction. The moment due to drag of the foil was cancelled electrically to allow direct reading of the wing pitching moment on the oscillograph trace. Figure 5 is a schematic of the strain gage instrumentation for measuring the flap forces.

For flap cycling tests an electric motor, mounted below the main balance, was used to drive the flaps through an eccentric, push rod, bellcrank, and flap torque shaft mechanism. Flap position was recorded by a strain gage element which followed the bellcrank displacements (see Figure 4).

All seven strain gage channels incorporated a Consolidated Electrodynamics Corporation (CEC) 3-kc carrier amplifier with an amplifier output calibration circuit, and a variable attenuation and galvanometer damping circuit with outputs recorded on a CEC oscillograph, type 5-114-P3-26. With the use of the amplifier calibration circuit, and the variable attenuation circuit, amplifier output was maintained within one percent. The analog velocity readout generated by a carriage-mounted direct-current generator, driven by a drum riding on the carriage rails, was also recorded on the oscillograph

record. Precise velocity was obtained from a distance-time history originating from a carriage-mounted photocell signal. Interrupters, spaced every five feet along the length of the carriage rails, broke the light path to the photocell, and caused a sharp trace deflection on the oscillograph record.

Photographic instrumentation consisted of a 16mm Eyemo motion picture camera. The camera was mounted on the carriage, above the model, and trained aft to observe the flow phenomena. Figure 6 is a photograph taken from the motion-picture film showing the flow pattern.

TEST PROCEDURES

All tests were conducted with the model mounted to the No. 2 carriage, using the hydraulic drive. The operating procedure consisted of testing the model over a range of velocities at a fixed depth of submergence of four inches, measured above the wing quarter-chord. Wing angles of attack were -5, 0, 2, 5, and 10 degrees. Flap deflection angles were fixed at -5, 0, 2, 5, 10 and 20 degrees. Data for these tests is tabulated in Tables I through IV.

During the latter part of the study program some tests were conducted with the flaps cycled at 0.5, 0.83, and 1.66 cycles per second. Depth of submergence was maintained at four inches, and wing angle of attack was fixed at 0 degrees. Flap deflection amplitudes ranged between 0 and 10 degrees.

Strut-interference tests consisted of operating the model with supporting struts at the wing tips. A series of runs was made in which the midspan strut was removed. These were repeated, with the midspan strut fairing mounted in place, but not touching the model. All runs were made with flaps neutral and at two wing angles of attack - 0 and 10 degrees. Depth of submergence was kept at 4 inches.

Photo-coverage and visual observations were made throughout the program to ensure that no air entrainment occurred.

Average test velocity throughout the study was 24 feet per second. Tank temperature was observed to be steady at 70°F, for which the density was 1.94 slugs/ft^3.

RESULTS

The results of this investigation are presented in coefficient form using NASA absolute coefficients.

LIFT

The flap-neutral lift curve is calculated from

$$C_L = (\alpha-\alpha_o)C_{L_\alpha} \tag{1}$$

where $(\alpha-\alpha_o)$ is the wing angle of attack measured from zero lift and

$$C_{L_\alpha} = c_{\ell_\alpha} \frac{k_t a}{E_c a + 2k_t(\tau+1)} . \tag{2}$$

All terms are those used in aeronautical practice. Figure 7 is a comparison plot between the experimental lift curve and the computed lift curve, using Equations 1 and 2 with the section data on the 16-309 wing from Reference 2. The figure shows Stack's lift curve for the 16-309, obtained from wind-tunnel tests, having a $C_{L_\alpha} = 0.1$/degree. His curve was three-dimensionalized and corrected for the effect of depth, using the empirical approximation in Reference 3, i.e.,

$$\frac{C_L}{C_{L_\infty}} = 1 - 0.422\, e^{-1.454\frac{h}{c}} . \tag{3}$$

The resulting lift curve had a slope of $C_{L_\alpha} = 0.059$/degree. The experimental curve, also shown in the figure, had a lower slope, namely, $C_{L_\alpha} = 0.05$/degree. The difference in the angle of zero lift of the experimental lift curve, with the calculated, amounts to about 0.2 of a degree.

The variation of lift-drag ratio with angle of attack, when the hydrofoil has neutral flap and is at a depth of submergence of one chord, is shown in Figure 8. The peak lift-drag ratio of 17 occurs at $\alpha = 2.8$ degrees, thereafter falling off as angle of attack increases beyond 2.8 degrees.

FLAP EFFECTIVENESS

Figures 9 through 12 present the curves of lift coefficient at various flap deflections for the four flap configurations. They show that a straight line relationship between C_L and α exists at all flap deflections over the tested range of angles of attack.

Figure 13 is a plot of flap effectiveness based on the experimental results for all four model configurations at $\alpha = 2°$, and at a depth of submergence of one chord. The figure shows that flap effectiveness varies with c_f/c and b_f/b, having an approximate linearity for values of δ_f between $-5°$ and $5°$.

The lift coefficient of a flapped wing can be written as

$$C_L = C_{L_\alpha} (\alpha - \alpha_o) + C_{L_{\delta_f}} \delta_f \tag{4}$$

where $C_{L_{\delta_f}}$ is the flap effectiveness. Following aeronautical practice, flap effectiveness is written:

$$C_{L_{\delta_f}} = f\left(\frac{c_f}{c}\right) f(\delta_f) f\left(\frac{b_f}{b}\right) f(\bar{h}) \tag{5}$$

where the functions $f\left(\frac{c_f}{c}\right)$, $f(\delta_f)$ and $f\left(\frac{b_f}{b}\right)$ are corrections for flap geometry (4) (5). The function $f(\bar{h})$ is a depth correction and it accounts for the fact that the hydrofoil is not operating in an infinite fluid. Inasmuch as the assessing of the flap's ability as a lift generator is the principal concern of this study, it is important that $f(\bar{h})$ be computed. This can be done by a simplification of

Prandtl's lifting line theory as applied to the biplane.

Figures 14 and 15 show the hydrofoil and its image operating as a biplane having a gap distance of 2h and no wing stagger. Figure 14 shows the vortex lifting lines, which, to a first approximation, replace the wings and flaps. Figure 15 shows the location of the wing and flap bound vortices. The wing vortex at (0, -h) has a strength Γ. The flap vortex at $(c_w + \frac{1}{4} c_f, -h)$ has a strength Γ_f. Corresponding image vortices, having the same strengths, are positioned at (0, h) and $(c_w + \frac{1}{4} c_f, h)$ respectively. Arranging the vortices in this manner, the problem then is one of finding the strengths of these vortices that induce a total downwash $\Sigma(v)$ at $(\frac{3}{4} c_w, -h, 0)$ and $(c_w + \frac{3}{4} c_f, -h, 0)$ which when added vectorially to the free stream velocity, U, produce a resultant flow that does not penetrate the chord line representing the wing and the flaps at these points. The two boundary equations are,

$$\frac{\Sigma(v)\left(\frac{3}{4} c_w, -h\ 0\right)}{U} = \tan \alpha \cong \alpha \tag{6}$$

$$\frac{\Sigma(v)\left(c_w + \frac{3}{4} c_f, -h, 0\right)}{U} = \tan (\alpha + \delta_f) \cong \alpha + \delta_f . \tag{7}$$

To set up Equation 6 the downwash at $(\frac{3}{4} c_w, -h, 0)$ due to the wing bound vortex is computed by using the Biot-Savart law,

$$v = -\frac{\Gamma}{2\pi} \frac{1}{\frac{c_w}{2}} \left(\frac{\frac{b}{2}}{\sqrt{\left(\frac{c_w}{2}\right)^2 + \left(\frac{b}{2}\right)^2}} \right)$$

where the minus sign denotes a downward flow.

The downwash at $(\frac{3}{4} c_w, -h, 0)$ due to the wing image bound vortex is

$$v = -\frac{\Gamma}{2\pi} \frac{\frac{c_w}{2}}{\left(\frac{c_w}{2}\right)^2 + (2h)^2} \left[\frac{\frac{b}{2}}{\sqrt{\left(\frac{c_w}{2}\right)^2 + (2h)^2 + \left(\frac{b}{2}\right)^2}} \right] .$$

The downwash at $(\frac{3}{4} c_w, -h, 0)$ due to the wing trailing vortices is

$$v = -\frac{\Gamma}{2\pi} \frac{2}{b} \left(1 + \frac{\frac{c_w}{2}}{\sqrt{\left(\frac{c_w}{2}\right)^2 + \left(\frac{b}{2}\right)^2}} \right)$$

The downwash at $(\frac{3}{4} c_w, -h, 0)$ due to the image wing trailing vortices is

$$v = -\frac{\Gamma}{2\pi} \frac{\frac{b}{2}}{(2h)^2 + \left(\frac{b}{2}\right)^2} \left(1 + \frac{\frac{c_w}{2}}{\sqrt{(2h)^2 + \left(\frac{b}{2}\right)^2 + \left(\frac{c_w}{2}\right)^2}} \right) .$$

The downwash at $(\frac{3}{4} c_w, -h, 0)$ due to the flap bound vortex is

$$v = \frac{\Gamma_f}{2\pi} \frac{1}{\frac{c_w + c_f}{4}} \left[\frac{\frac{b_f}{2}}{\sqrt{\left(\frac{c_w + c_f}{4}\right)^2 + \left(\frac{b_f}{2}\right)^2}} \right] .$$

The downwash at $(\frac{3}{4} c_w, -h, 0)$ due to the flap image bound vortex is

$$v = \frac{\Gamma_f}{2\pi} \frac{\frac{c_w + c_f}{4}}{\left(\frac{c_w + c_f}{4}\right)^2 + (2h)^2} \left[\frac{\frac{b_f}{2}}{\sqrt{\left(\frac{c_w + c_f}{4}\right)^2 + \left(\frac{b_f}{2}\right)^2 + (2h)^2}} \right] .$$

The downwash at $(\frac{3}{4} c_w, -h, 0)$ due to the flap trailing vortices is

$$v = \frac{\Gamma_f}{2\pi} \frac{1}{\frac{b_f}{2}} \left[1 - \frac{\frac{c_w}{4}}{\sqrt{\left(\frac{c_w}{4}\right)^2 + \left(\frac{b_f}{2}\right)^2}} \right] .$$

The downwash at $(\frac{3}{4} c_w, -h, 0)$ due to the flap image trailing vortices is

$$v = -\frac{\Gamma_f}{2\pi} \frac{\frac{b_f}{2}}{\left(\frac{b_f}{2}\right)^2 + (2h)^2} \left[1 - \frac{\frac{c_w + c_f}{4}}{\sqrt{\left(\frac{c_w + c_f}{4}\right)^2 + (2h)^2 + \left(\frac{b_f}{2}\right)^2}} \right] .$$

Now adding the foregoing downwash contributions from each vortex in the real wing and setting this sum equal to the product $U\alpha$, Equation 6 results. Equation 7 can be derived in a similar manner. To summarize then, the equations for which we may solve for Γ and Γ_f, after some rearrangement of terms, are:

$$\Gamma \left\{ B + \frac{1}{1 + 16\bar{h}^2 k^2} B_1 + k\frac{c}{b} + \frac{1}{2} kcB_2 \right\} - \Gamma_f \left\{ B_3 + \frac{1}{64\bar{h}^2 + 1} B_4 - \frac{1}{2}\frac{c}{b_f} - \frac{1}{4} c B_5 \right\} 2k = U\pi kc\alpha \qquad (8)$$

$$\Gamma \left\{ \frac{1}{3} B_6 + \frac{3}{9 + 64\bar{h}^2} B_7 + \frac{1}{2}\frac{c}{b} + \frac{1}{4} c B_8 \right\} 2k + \Gamma_f \left\{ B_9 + \frac{1}{1 + 16\frac{\bar{h}^2}{E^2}} B_{10} + E\frac{c}{b_f} + \frac{E}{2} c B_{11} \right\} \frac{k}{E} = U\pi kc(\alpha + \delta_f) \qquad (9)$$

where the B – coefficients are

$$B = \frac{\frac{b}{2}}{\sqrt{\left(\frac{c_w}{2}\right)^2 + \left(\frac{b}{2}\right)^2}}, \quad B_1 = \frac{\frac{b}{2}}{\sqrt{\left(\frac{c_w}{2}\right)^2 + (2h) + \left(\frac{b}{2}\right)^2}},$$

$$B_2 = \frac{\frac{b}{2}}{(2h)^2 + \left(\frac{b}{2}\right)^2}, \quad B_3 = \frac{\frac{b_f}{2}}{\sqrt{\left(\frac{c}{4}\right)^2 + \left(\frac{b_f}{2}\right)^2}},$$

$$B_4 = \frac{\frac{b_f}{2}}{\sqrt{\left(\frac{c}{4}\right)^2 + \left(\frac{b_f}{2}\right)^2 + (2h)^2}}, \quad B_5 = \frac{\frac{b_f}{2}}{\left(\frac{b_f}{2}\right)^2 + (2h)^2},$$

$$B_6 = \frac{\frac{b}{2}}{\sqrt{\left(\frac{3}{4}c\right)^2 + \left(\frac{b}{2}\right)^2}}, \quad B_7 = \frac{\frac{b}{2}}{\sqrt{\left(\frac{3}{4}c\right)^2 + (2h)^2 + \left(\frac{b}{c}\right)^2}},$$

$$B_8 = \frac{\frac{b}{2}}{\left(\frac{b}{2}\right)^2 + (2h)^2}, \quad B_9 = \frac{\frac{b_f}{2}}{\sqrt{\left(\frac{b_f}{2}\right)^2 + \left(\frac{c_f}{2}\right)^2}},$$

$$B_{10} = \frac{\frac{b_f}{2}}{\sqrt{\left(\frac{c_f}{2}\right)^2 + (2h)^2 + \left(\frac{b_f}{2}\right)^2}}, \quad B_{11} = \frac{\frac{b_f}{2}}{(2h)^2 + \left(\frac{b_f}{2}\right)^2}.$$

By substituting the various values for the coefficients, B, B_1, B_2, etc., Equations 8 and 9 may be solved for Γ and Γ_f. The total downwash at ($\frac{3}{4}c_w$, -h, 0) and ($c_w + \frac{3}{4}c_f$, -h, 0) for conditions of finite submergence and infinite submergence can then be obtained by substituting the values of Γ and Γ_f in each of the appropriate downwash formulas and adding the results. The depth function $f(\bar{h})$ can then be computed by ratioing the infinite submergence downwash to the finite submergence downwash. This function expresses the ratio of vorticity generated at infinite submergence to the greater vorticity generated at finite submergence in order to produce the same lift. Inasmuch as the vorticity is a measure of the lift of the foil, the function $f(\bar{h})$ can be regarded as the ratio of lift at finite submergence to the lift at infinite submergence.

Equations 8 and 9 were solved for Γ and Γ_f for $\frac{h}{c}$ = 0.25, 0.50, 0.75, 1.0, and ∞ for δ_f = 2, 0, 5, 10, and 20 degrees at α = 2 degrees and $\frac{b_f}{b}$ = 0.8 and $\frac{c_f}{c}$ = 0.3. The velocities were summated, the depth function was determined, and a plot of it is shown in Figure 16. The figure indicates that for any given flap deflection there is a variation in lift with δ_f, as previous experiments have indicated, (see References 4 and 5). Further it indicates that at a fixed depth the effect of the flap is greater at low flap angles than at high flap angles. The foregoing derivation of $f(\bar{h})$ makes the assumption of constant spanwise vorticity which is not a physical reality. However, as $f(\bar{h})$ is a ratio of two conditions of submergence, it is felt that the assumption of constant spanwise vorticity is not gross.

Using the information presented in Figure 16, plots of ΔC_L versus δ_f for Model Configuration 2 (c_f/c = 0.3, b_f/b = 0.8) are presented in Figure 17, for $\frac{h}{c}$ = 0.5, 1.0, and ∞, using Equation 5 and the charts in Reference 4. The figure indicates that aeronautical theory predicts considerably higher values of lift coefficient for a given flap angle than were obtained in this study.

The effect of depth was assessed experimentally using Model Configuration 2. Plots of C_L versus submergence are presented for a range of flap angles in Figure 18.

DRAG

The drag coefficient of a subcavitating hydrofoil having rectangular planform and zero dihedral can be written as

$$C_D = C_{D_i} + C_{D_o} . \tag{10}$$

The induced drag coefficient, C_{D_i}, is made up of two terms:

$$C_{D_i} = \frac{C_L^2}{\pi a} (1 + \sigma) + \frac{K (\Delta C_L)^2}{\pi a} \tag{11}$$

where the first term on the right is the recognizable form for a non-elliptic planform. The second term contains the lift coefficient increment due to the flap, and K is a function of flap geometry (see References 4 and 6).

The profile drag coefficient, C_{D_o}, is made up of two parts, the sum of the section drag and friction coefficients ($c_d + 2C_f$), plus the change in profile drag coefficient due to flap deflection ΔC_{D_o}.

The change in profile drag coefficient is generally expressed as,

$$\Delta C_{D_o} = d\left(\frac{c_f}{c}\right) \; d(\delta_f) \; d\left(\frac{b_f}{b}\right) \tag{12}$$

where

$$d\left(\frac{c_f}{c}\right) , \quad d(\delta_f) , \quad d\left(\frac{b_f}{b}\right)$$

are corrective functions for variations of flap-chord ratio, flap angle, and flap span, respectively.

Figures 19, 20, 21, and 22 present the experimental curves of drag coefficient for all four model configurations. Figure 23 compares the results for three of the configurations at a fixed angle of attack of 2 degrees, and it is seen that agreement between the test points and the calculated values are reasonably good at low flap angles. At large flap angles, the calculated drag coefficients tend to be slightly higher than those obtained experimentally. No depth correction was incorporated in Equation 11, and it appears that the effect of depth on drag is quite small. Drag coefficients are for foil only, as strut and interference drags have been eliminated.

At the conclusion of the second part of the test program, a series of runs was made in order to determine the effect of strut-wing interference drag. First, a series of runs was made with the wing supported by a strut at each tip and with the normal midspan strut removed. Runs were made with flaps neutral at two wing angles of attack, 0 and 10 degrees, while depth of submergence was kept at four inches. The drag balance was attached to the yoke in which the tip struts were mounted so that the drag of the configuration was

$$D_1 = D_{wing} + D_{struts} .$$

The tests were then repeated with the normal midspan strut fairing in position but not attached to the yoke and not touching the wing. The resultant drag of this configuration was

$$D_2 = D_{wing} + D_{struts} + D_{interference} .$$

The difference in drag results obtained by the two configurations $(D_2 - D_1)$ was attributed to interference of the strut on the foil (assuming, of course, that there was no measurable interference effect between the midspan fairing

and tip struts). Figure 24 shows the mounting arrangement for this test, and Figure 25 is a plot of ΔC_D due to strut wing interference. This was subtracted from the total measured drag to give the data tabulated in Tables I through IV.

PITCHING MOMENT

The pitching moment coefficient for a flapped airfoil with a full-span flap positioned at δ_f degrees is given by

$$C_M = C_{M_o} + \left(\frac{\partial C_M}{\partial \delta_f}\right) \delta_f \tag{13}$$

where C_{M_o} is the pitching moment coefficient for the undeformed section and the partial $\frac{\partial C_M}{\partial \delta_f}$ is a proportionality factor which Reference 7 derives as

$$\frac{\partial C_M}{\partial \delta_f} = \frac{-C_{L_\alpha}}{\pi} (1 - E)\sqrt{E(1 - E)} \ . \tag{14}$$

From empirical data based on accumulated wind tunnel tests, the estimate of C_M about the quarter-chord is generally of the form

$$\Delta C_M = m(E)m\left(\frac{b_f}{b}\right) \Delta C_L \tag{15}$$

because of the close correlationship between ΔC_M and ΔC_L. The two functions m(E) and $m(b_f/b)$ are corrections for flap-chord ratio, and for the effect of partial span. Empirical curves of these functions are given in Reference 4 for calculating ΔC_M. The experimental results presented in Figures 26, 27, 28, and 29, generally confirm aero trends which indicate that the variation in pitching moment coefficient with flap deflection is independent of angle of attack. Figure 30 shows the comparison between aerodynamic

estimates and theory versus the experimental tank results. Although the test data in Figure 30 does show some scatter, all of the test points along the band consistently fall away from Glauert's theoretical curve at large angles of attack. However, the slope of the band of points is generally parallel to the aero estimates from Reference 4.

Thin airfoil theory indicates that there is a fixed relation between pitching moment and lift coefficient increments for a given flap-chord ratio,

$$\left(\frac{\Delta c_m}{\Delta c_\ell}\right)_{\delta_f} = \frac{-\frac{1}{4}\left(\sin\theta_o - \frac{1}{2}\sin 2\theta_o\right)}{\left[(\pi - \theta_o) + \sin\theta_o\right]} \qquad (16)$$

where $\sin\theta_o = 2\sqrt{E(1-E)}$ $\quad \cos\theta_o = 2E - 1$

and $E = c_f/c$

Figure 31 is a plot of $\Delta C_M/\Delta C_L$ against δ_f for Model Configuration 2. The deviation between theory and the test data is illustrated by the magnitude of the slope of the solid line which represents the average curve from test data.

FLAP FORCES

Theoretical expressions for the flap-lift coefficient, and hinge-moment coefficient for a flap on a thin airfoil, are given:

$$C_{L_f} = C_{L_{f_o}} + \left(\frac{\partial C_{L_f}}{\partial C_L}\right) C_L + \left(\frac{\partial C_{L_f}}{\partial \delta_f}\right)\delta_f \qquad (17)$$

$$C_{H_f} = C_{H_{f_o}} + \left(\frac{\partial C_{H_f}}{\partial C_L}\right) C_L + \left(\frac{\partial C_{H_f}}{\partial \delta_f}\right)\delta_f \qquad (18)$$

The partials in Equation 17 were derived by Pinkerton (Reference 8) by integrating the load over the flap of a thin airfoil. They are:

$$\left(\frac{\partial C_{L_f}}{\partial C_L}\right) = \frac{2}{\pi(1+\cos\phi)} (\pi - \phi - \sin\varphi) \tag{19}$$

$$\left(\frac{\partial C_{L_f}}{\partial \delta_f}\right) = \frac{4}{\pi(1+\cos\varphi)} \left[\sin^2\varphi(1+\cos\varphi) + 2\sum_1^n \left(\frac{\sin\varphi \sin n\varphi \cos n\varphi}{n^2-1} - \frac{\cos\varphi \sin^2 n\varphi}{n(n^2-1)}\right)\right] . \tag{20}$$

Where

$$\cos\varphi = -(1-2E)$$

$$\sin\varphi = 2\sqrt{E}(1-E)$$

$$E = \frac{c_f}{c}$$

Approximate values of $\left(\frac{\partial C_{L_f}}{\partial \delta_f}\right)$ were derived by Pinkerton inasmuch as the series term in Equation (20) does not have a general summation. Pinkerton's plot of $\left(\frac{\partial C_{L_f}}{\partial \delta_f}\right)$ and $\left(\frac{\partial C_{L_f}}{\partial C_L}\right)$ is presented in Figure 32 for reference.

Glauert derived expressions for the partials in Equation 18 from thin

airfoil theory. They are:

$$\left(\frac{\partial C_{H_f}}{\partial C_L}\right) = \frac{1}{\pi E^2}\left[\left(\frac{3}{2} - E\right)\sqrt{E(1-E)} - \left(\frac{3}{2} - 2E\right)\left(\frac{\pi}{2} - \cos^{-1}\sqrt{E}\right)\right] \quad (21)$$

$$\left(\frac{\partial C_{H_f}}{\partial \delta_f}\right) = \frac{4(1-E)\sqrt{E(1-E)}}{\pi E^2}\left[\frac{\pi}{2} - \cos^{-1}\sqrt{E} - \sqrt{E(1-E)}\right] \quad (22)$$

Equations 21 and 22 are plotted in Figure 33 for reference.

Flap normal force coefficient and axial force coefficient, using the wing chord as directional reference, are plotted in Figures 34 through 41 for all model configurations. Normal and axial force coefficients were preferred for presentation because it was felt that the data would be more useful for structural design. The figures show the independence of C_{N_f} and C_{A_f} from wing angle of attack, α.

In comparing the experimental results with the theory as derived by Pinkerton and Glauert, the C_{N_f} - data at α = 2 degrees for all four models was converted to C_{L_f} - data, which is presented in Figures 42 and 43. The figures show a linear variation between C_{L_f} and δ_f at low flap angles and the experimental curve parallels the theoretical curve (Reference 8). Beyond δ_f = 4 degrees; however, there is a marked fall-off in the C_{L_f} as δ_f is increased. This is a probable indication that the flow region above the flap has a low velocity.

Figures 44, 45, 46, and 47, are plots of flap hinge moment coefficient against angle of attack, α. Comparison with Glauert's expression (Equation 22) in Figures 48, 49, 50, and 51, generally indicate that the flap hinge moment will be considerably less than predicted theoretically.

EFFECT OF SPEED

Figures 52 and 53 are plots of wing and flap coefficients for Model Configuration 1, covering angles of attack of -5 and 10 degrees, and flap detection angles of -5 to 20 degrees for a range of Reynolds numbers between 0.4×10^6 to 0.9×10^6. These results are typical for all configurations, and indicate that the force coefficients are independent of the velocity of the model within the range of Reynolds numbers considered.

LIFT, DRAG, PITCHING MOMENT, WITH FLAPS CYCLED

All of the hydrofoil model configurations were tested at three flap-cycling rates, 0.5, 0.83, and 1.66 cps. Curves of lift, drag, and pitching moment coefficient are presented in Figures 54, 55, and 56 for Model Configuration 1, inasmuch as it is considered generally representative of the flap-cycled results for all of the models.

The results of this phase of the test program will be included in another report in which the dynamic aspects of the flap cycling will be brought out. Conclusions on this phase are, therefore, reserved for later.

CONCLUSIONS

This study has demonstrated that flapped airfoil data may be used to predict the forces and moments on the wing and flap of a fully-submerged hydrofoil.

The flap-neutral lift curve can be predicted with fair accuracy from aeronautical data incorporating a depth correction.

The hydrofoil lift curve slope is not affected by flap deflection. The lift curve retains its linearity up to very large angles of attack using the maximum size flap of $\frac{c_f}{c} = 0.3$ and $\frac{b_f}{b} = 0.8$.

It has been shown theoretically and experimentally that flap effectiveness varies with depth of submergence. Theory predicts much higher values of flap effectiveness than were obtained in these tests.

Aerodynamic data may be used to predict hydrofoil flap lift coefficient for low flap angles. For the 16-309 section, the experimental values of C_{L_f} fall off sharply at about $\delta_f = 4°$ for all of the models tested.

Flap hinge moment coefficient can be predicted with fair accuracy from aerodynamic theory.

BIBLIOGRAPHY

1. Convair Hydrodynamic Laboratory, Convair Report ZH-114.

2. Stack, J., "Tests of Airfoils Designed to Delay the Compressibility Burble," NACA Report 763, 1943.

3. Tinney, E. R., "Experimental and Analytical Studies of Dihedral Hydrofoils," St. Anthony Falls Hydraulic Laboratory, University of Minnesota Project Report 41, 1954.

4. Young, A. D., "The Aerodynamic Characteristics of Flaps," British ARC, R & M Report 2622, February 1947.

5. Lowry, J. G. and Polhamus, E. C., "A Method for Predicting Lift Increments due to Flap Deflection at Low Angles of Attack in Incompressible Flow," NACA Report TN 3911.

6. Pearson, H. A., "A Method of Estimating the Aerodynamic Effects of Ordinary and Split Flaps of Airfoils Similar to the Clark Y," NACA Report TN 571, June 1936.

7. Glauert, H., "Theoretical Relationships for an Aerofoil with Hinged Flap," British ARC, R & M Report 1095, 1927.

8. Pinkerton, R. M., "Analytical Determination of the Load on a Trailing Edge Flap," NACA Report TN 353, 1930.

9. Wu, Y. T., "A Theory for Hydrofoils of Finite Span," CIT Report 26-8, May 1953.

10. Wadlin, K. L.; Shuford, C. L., Jr.; and McGehee, J. R., "A Theoretical and Experimental Investigation of the Lift and Drag Characteristics of Hydrofoils at Subcritical and Supercritical Speeds," NACA Report 1232, 1955.

11. Wadlin, K. L. and Christopher, K. W., "A Method for Calculation of Hydrodynamic Lift for Submerged and Planing Rectangular Lifting Surfaces," NACA TN 4168, January 1958.

12. Wadlin, K. L.; Fontana, R. E., and Shuford, C. L., "The Effect of End Plates, End Struts and Depth of Submergence on the Characteristics of a Hydrofoil," NACA Report RM L51B13, April 1951.

13. De Young, J., "Theoretical Symmetric Span Loading Due to Flap Deflection for Wings at Subsonic Speeds," NACA Report 1071.

SYMBOLS

α	angle of attack, degrees
δ_f	angular deflection of flap, degrees (+ve when flap deflects downward)
c	chord of hydrofoil, leading edge to flap trailing edge
S	area of hydrofoil
h	depth of the foil 1/4-chord below the free surface
c_w	chord of the wing, less flap
c_f	chord of the flap
S_f	area of the flap
b	foil span
t	thickness of hydrofoil
b_f	flap span
L	lift of hydrofoil including flap
D	drag of hydrofoil including flap
M	pitching moment of hydrofoil with flap
C_L	hydrofoil total lift coefficient, L/qS
C_D	hydrofoil total drag coefficient, D/qS (foils and flaps only)
C_M	hydrofoil total moment coefficient, M/qS_c (about 1/4-chord)
C_{M_o}	pitching moment coefficient for the undeformed section
C_{L_α}	slope of the lift curve for a wing in an infinite fluid, $\left(\frac{\partial C_L}{\partial \alpha}\right)$

c_{ℓ_α}	sectional lift curve, $\left(\frac{\partial c_\ell}{\partial \alpha}\right)$
C_{D_i}	induced drag coefficient
C_{D_o}	profile drag coefficient
c_d	section drag coefficient
C_f	friction drag coefficient (based on ATTC 1947 friction line)
C_{L_f}	flap lift force coefficient, $L_f/q\,S_f$
$C_{L_{f_o}}$	flap lift force coefficient for the unflapped section at zero lift
C_{D_f}	flap drag force coefficient, $D_f/q\,S_f$
C_{N_f}	flap normal force coefficient, N_f/qS_f
C_{A_f}	flap axial force coefficient, $A_f/q\,S_f$
$\left(\frac{\partial C_M}{\partial \delta_f}\right)$	rate of change of pitching moment coefficient with flap deflection
c_m	section moment coefficient about 1/4-chord
c_ℓ	section lift coefficient
C_{L_α}	lift coefficient at infinite submergence
$C_{L_{\delta_f}}$	rate of change of lift coefficient with flap deflection, $\left(\frac{\partial C_L}{\partial \delta_f}\right)$
C_{H_f}	hinge moment coefficient of flap, $H_f/q\,S_f\,c_f$
$C_{H_{f_o}}$	hinge moment coefficient for the unflapped section at zero lift
α_o	angle of zero lift of hydrofoil, deg
a	aspect ratio (b^2/A)
$f(\bar{h})$	correction to the slope of the section lift curve for the presence of the free surface

U	foil velocity, (ft/sec)
Γ	strength of wing vortex at 1/4 c_w, (wing less flap 1/4-chord)
Γ_f	strength of flap vortex at c_w + 1/4 c_f, (flap 1/4-chord)
E_c	Jones edge correction $\left(\frac{\text{wing semi-perimeter}}{\text{wing span}}\right)$
E	c_f/c
$\bar{h}$	h/c
k	c_w/c
K	function of flap geometry
σ	induced drag correction for a non-elliptic wing
v	downwash velocity
$\left(\frac{\partial C_{H_f}}{\partial C_L}\right)_{\delta_f}$	rate of change of flap hinge-moment coefficient with change in fixed-surface angle of attack, flap deflection held constant
$\left(\frac{\partial C_{H_f}}{\partial \delta_f}\right)_{C_L}$	rate of flap hinge-moment coefficient with change in angle of surface deflection, angle of attack of fixed surface constant
ρ	density, slugs/ft^3
k_t	$\frac{1+\epsilon}{1+\epsilon^2}$ where $\epsilon = \frac{4}{3\sqrt{3}} \times \frac{t}{c}$
τ	correction for non-elliptical planform

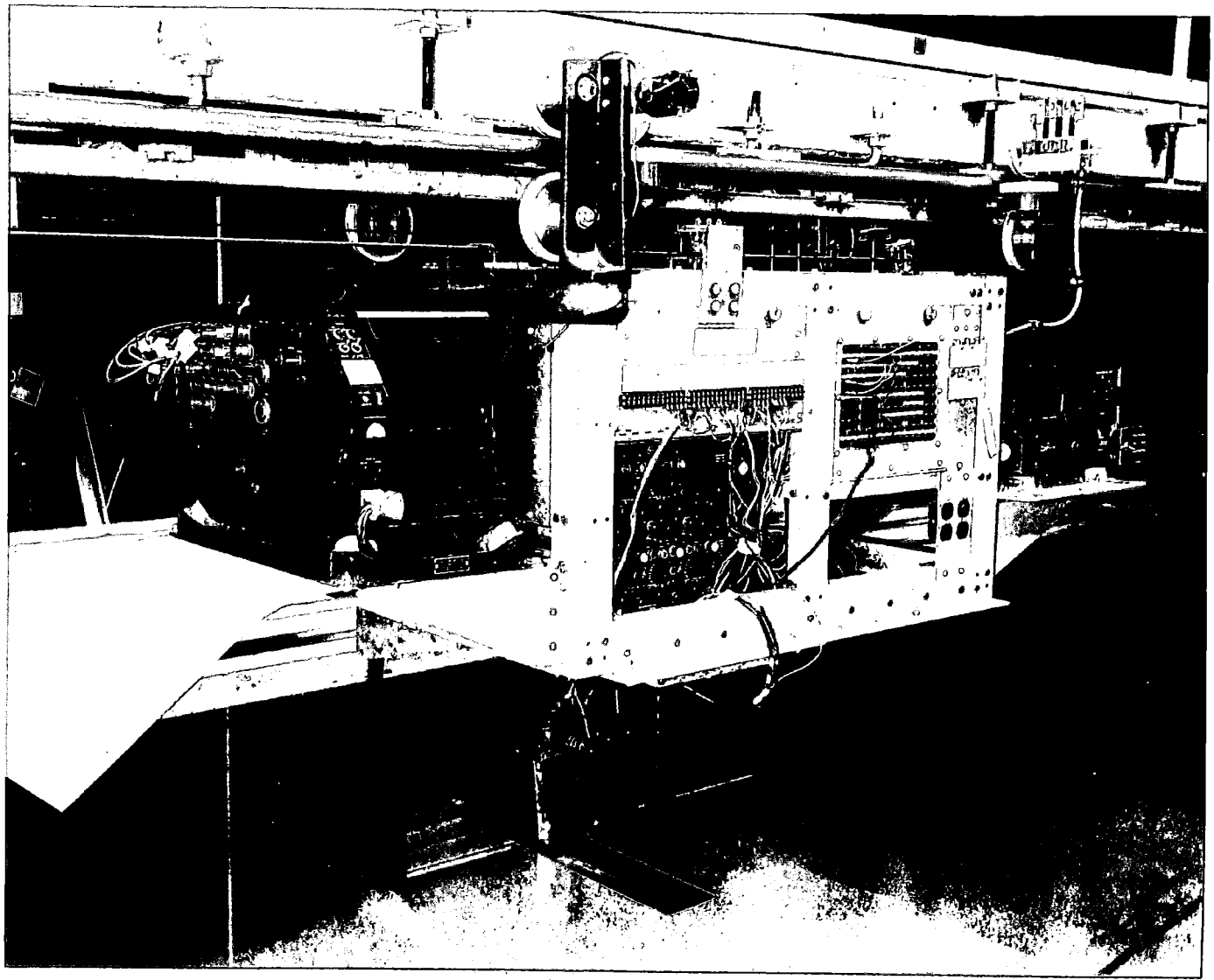

Figure 1. MODEL MOUNTED ON HIGH-SPEED CARRIAGE

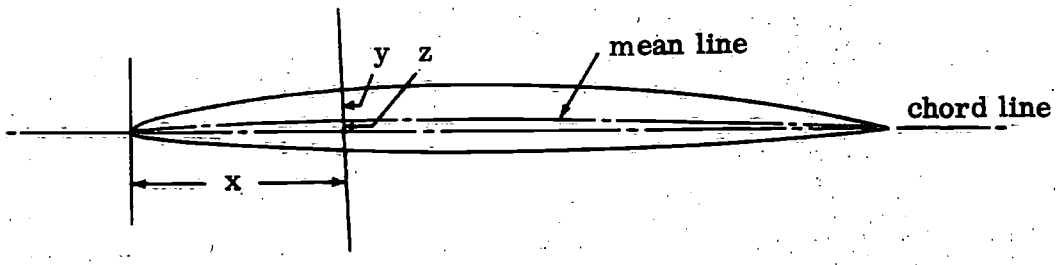

x in.	Basic half thickness Ordinate for 9% section y in.	Mean Line Ordinate for design $C_L = 0.3$ z in.
0.0	0.0	0.0
0.05	0.039	0.006
0.10	0.054	0.011
0.20	0.075	0.019
0.30	0.091	0.025
0.40	0.104	0.031
0.60	0.124	0.040
0.80	0.140	0.048
1.20	0.163	0.058
1.60	0.176	0.064
2.00	0.180	0.066
2.40	0.175	0.064
2.80	0.158	0.058
3.20	0.126	0.048
3.60	0.076	0.031
3.80	0.043	0.019
4.00	0.0	0.0

Notes:
1. Data taken from Reference 5.
2. Leading-edge radius = 0.016 in.
3. All ordinates based on 4.0-inch chord.
4. Ordinates (y) are superimposed on the mean line (z), and one measured perpendicular to the mean line.

Figure 2. HYDROFOIL MODEL ORDINATES (HYDROFOIL, NACA 16-309)

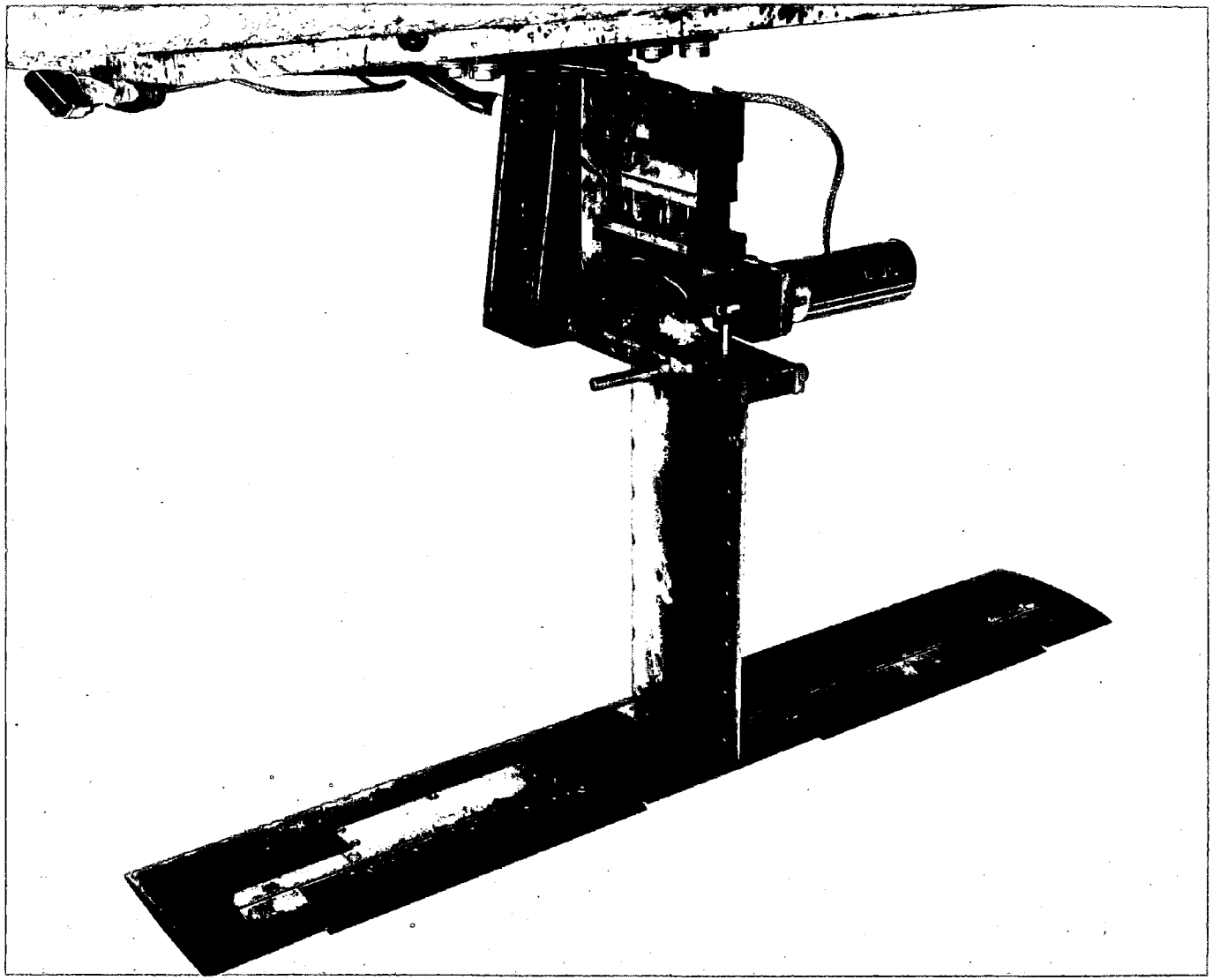

Figure 3. MODEL WITH $c_f/c = 0.2$, $b_f/b = 0.6$, FLAPS INSTALLED

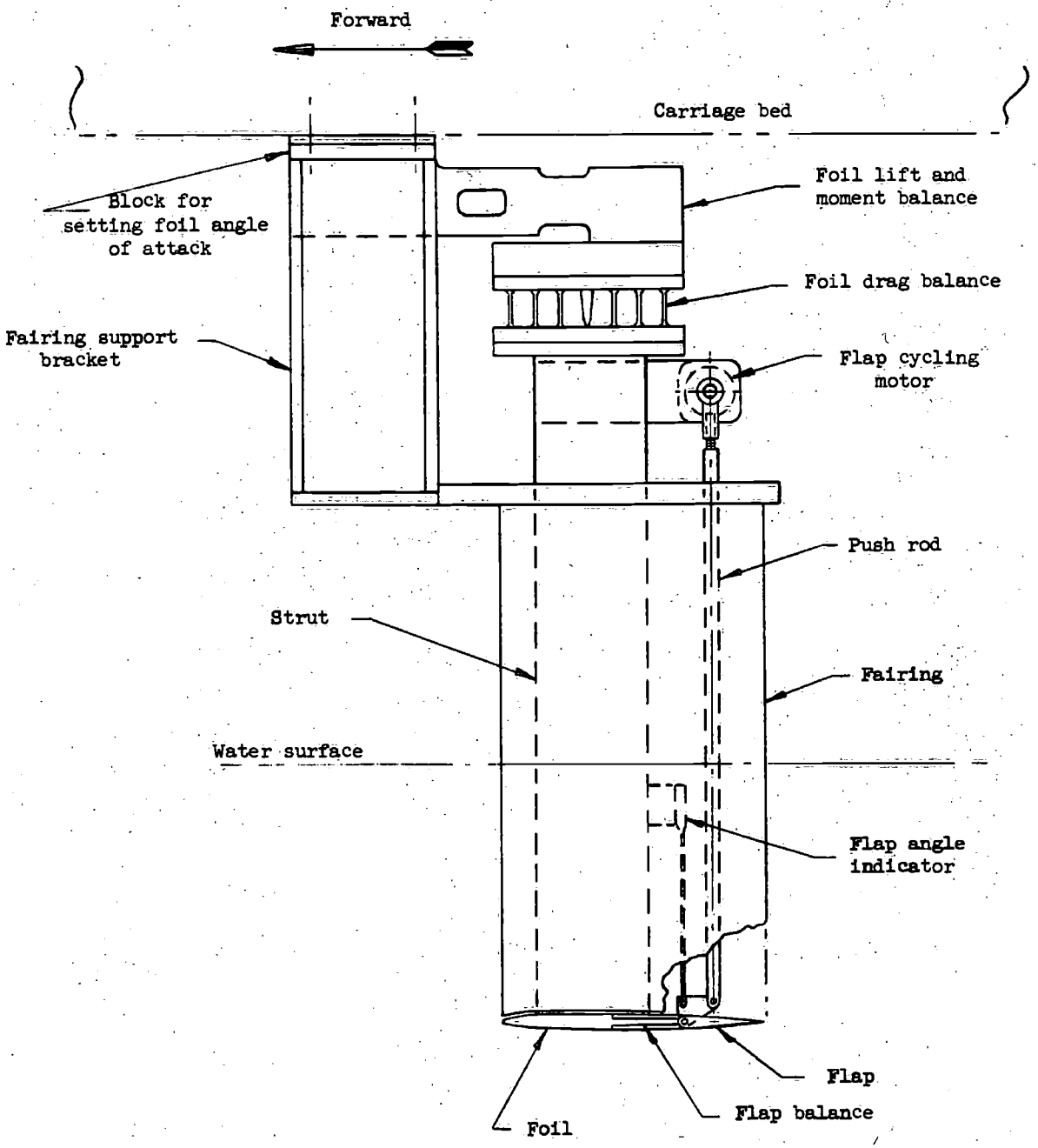

Figure 4. SCHEMATIC DRAWING OF MODEL AND BALANCES

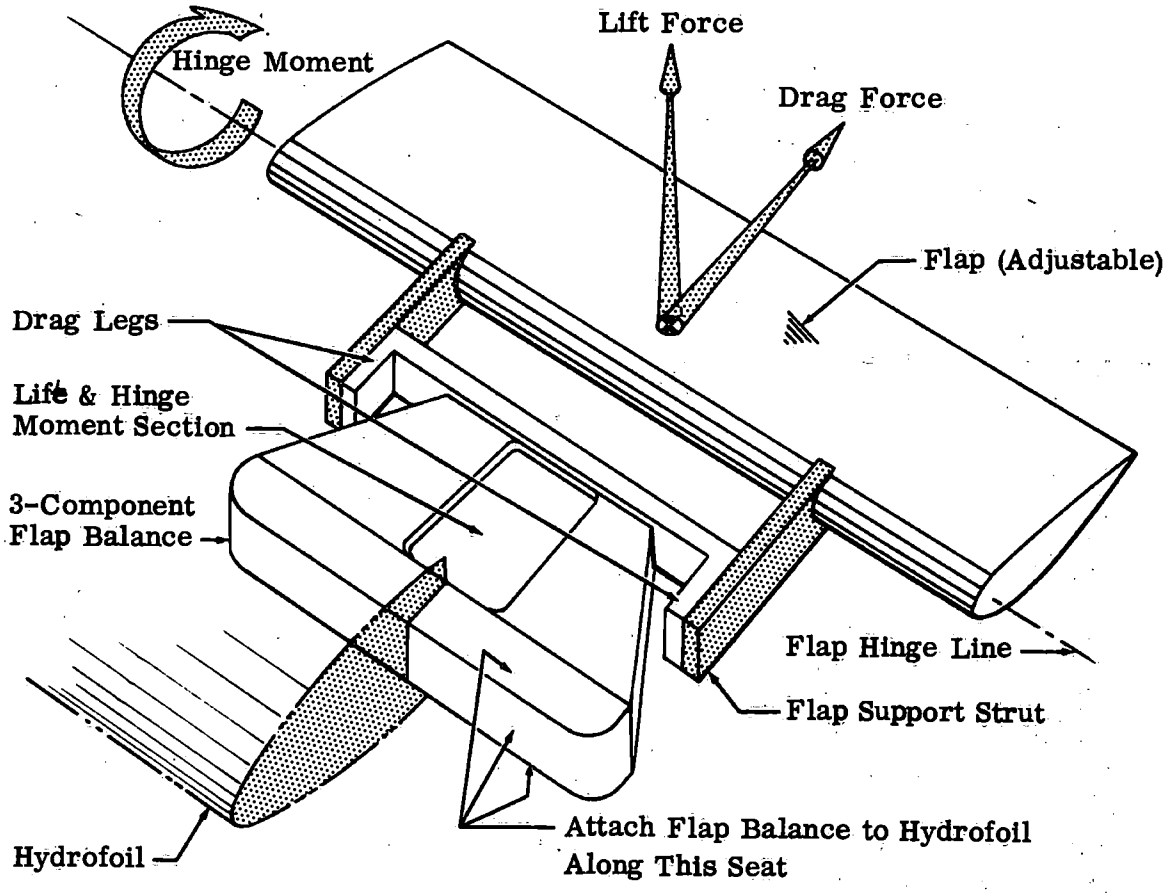

Note: Strain gages were bonded to the drag legs and lift and hinge moment sections in such a way as to give maximum output from lift and drag forces, while reducing interactions and combine load effects that were present in this load-measuring system. The strain gages were picked by means of a special digital computer program.

Figure 5. STRAIN GAGE INSTRUMENTATION FOR MEASURING FLAP FORCES

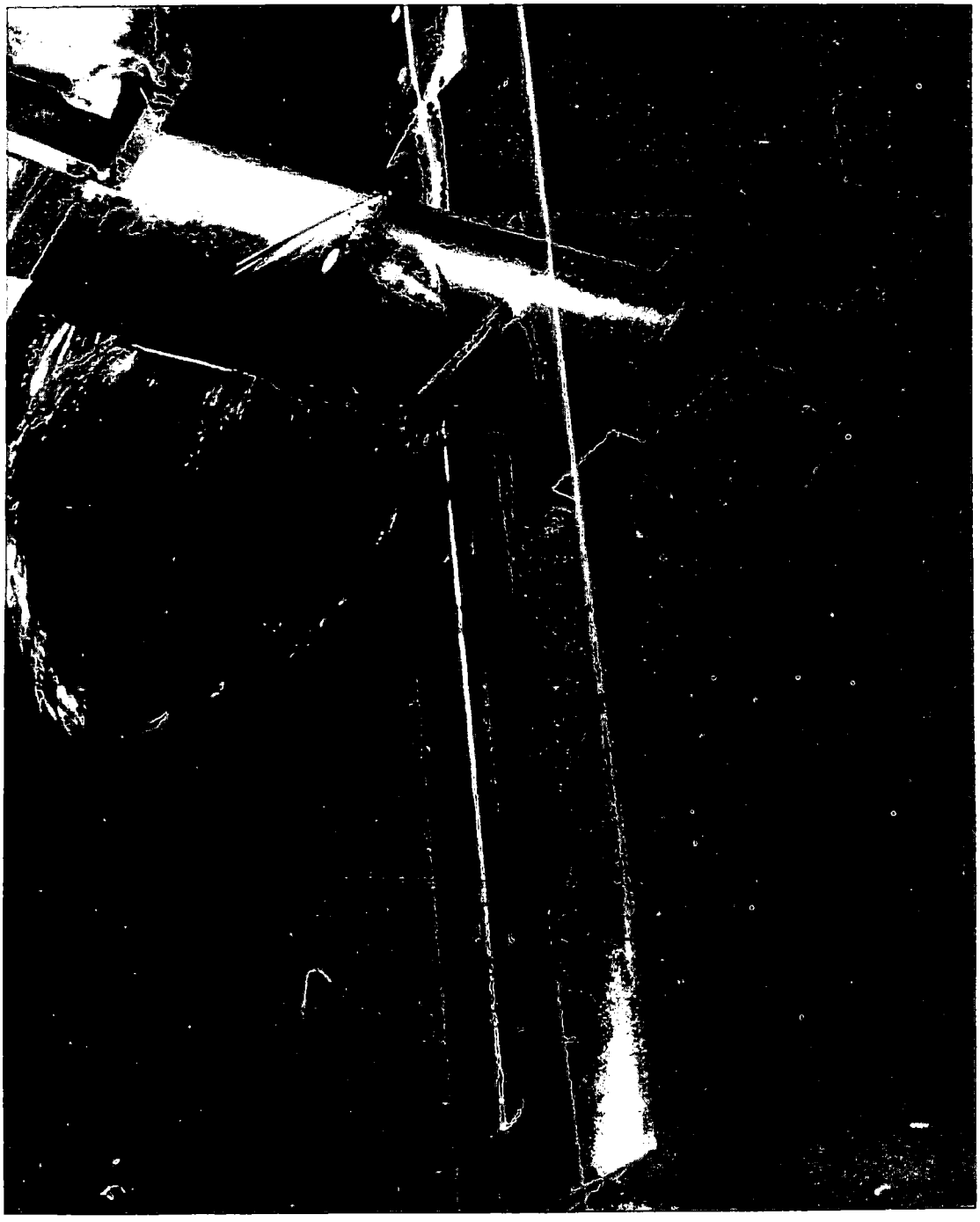

Figure 6. FLOW AROUND THE MODEL

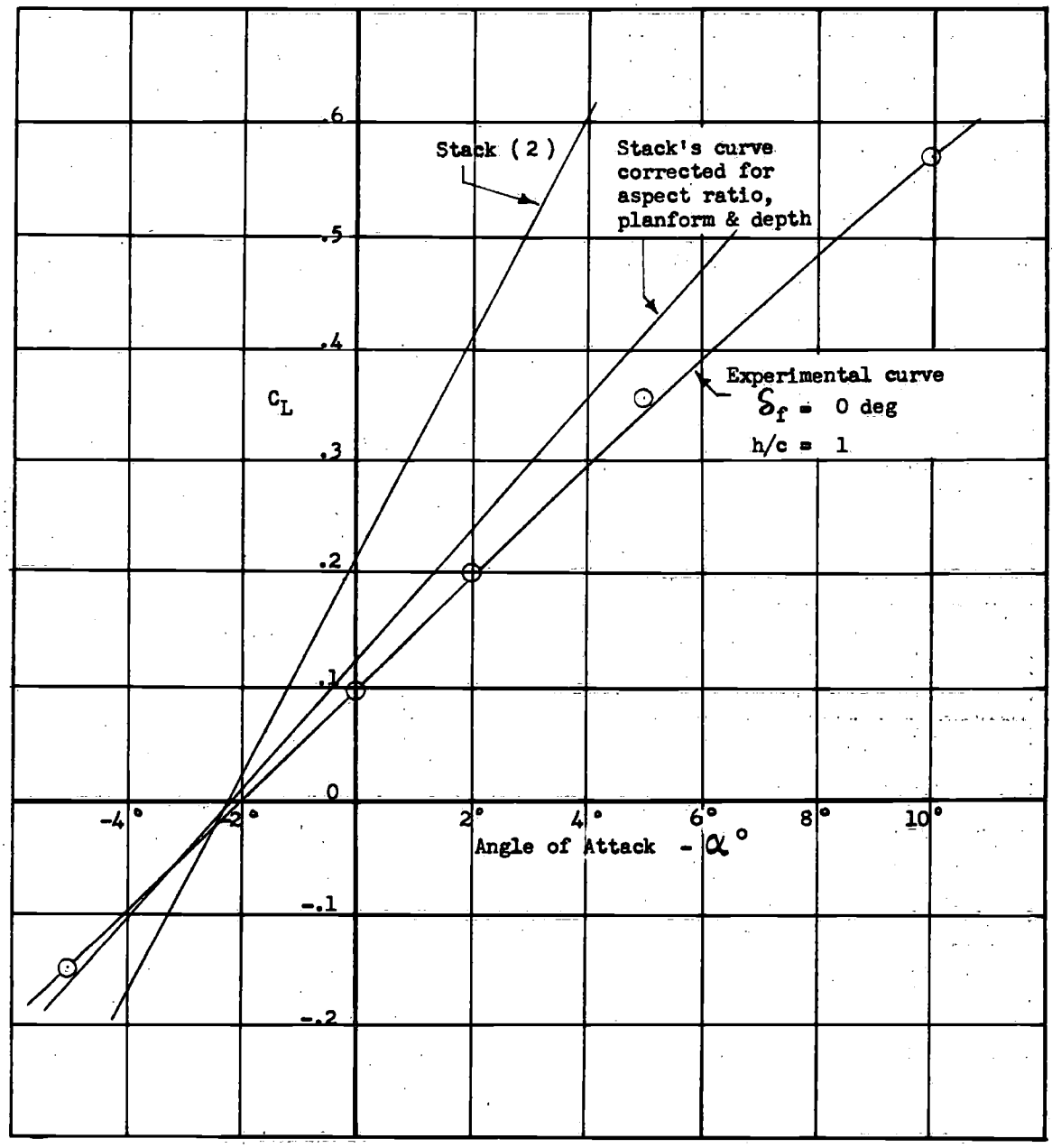

Figure 7. COMPARISON BETWEEN EXPERIMENTAL LIFT CURVE AND AERODYNAMIC DATA

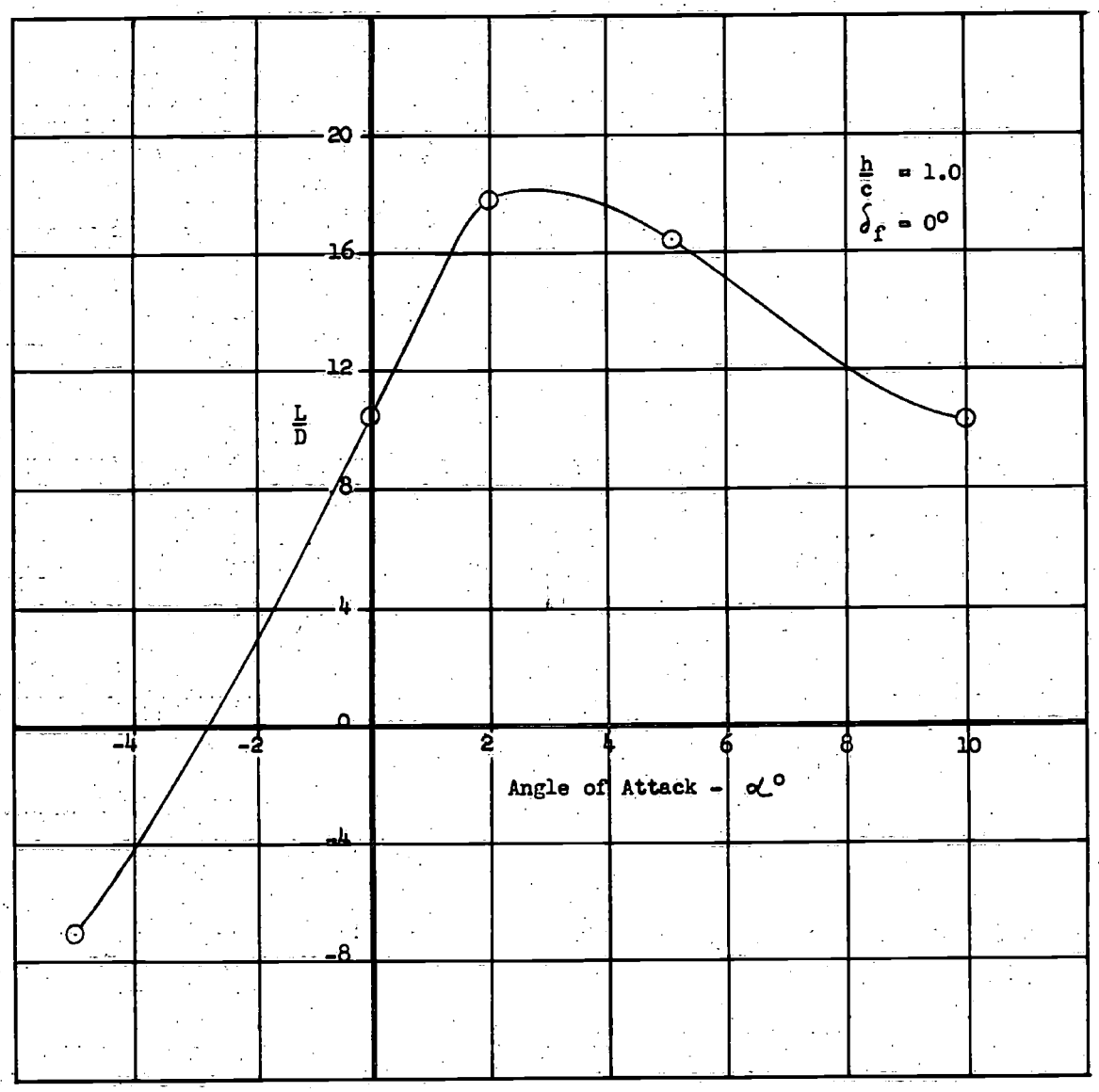

Figure 8. VARIATION OF LIFT-DRAG RATIO WITH ANGLE OF ATTACK

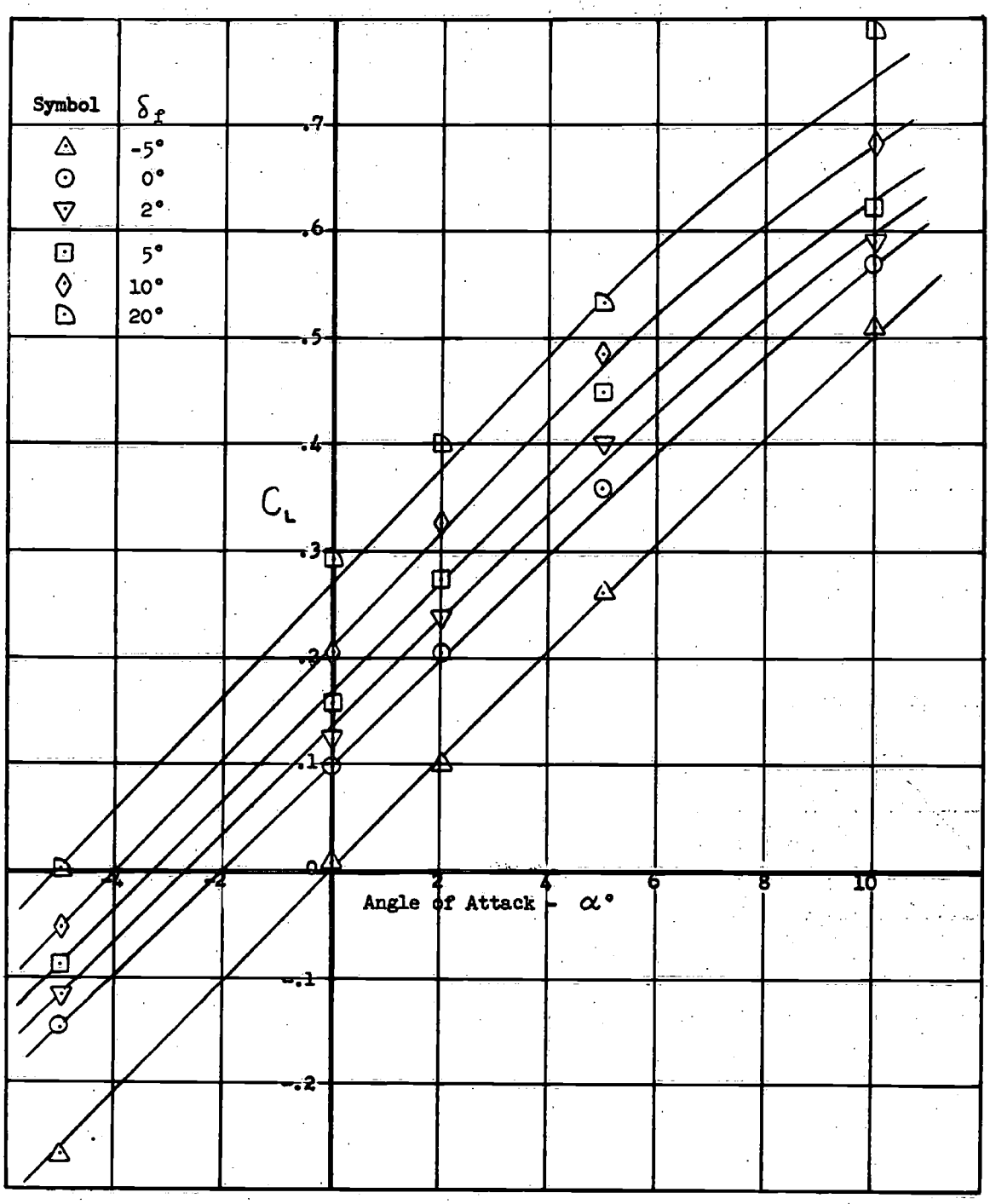

Figure 9. LIFT COEFFICIENT: MODEL CONFIGURATION 1
$c_f/c = 0.3$, $b_f/b = 0.6$, $h/c = 1$

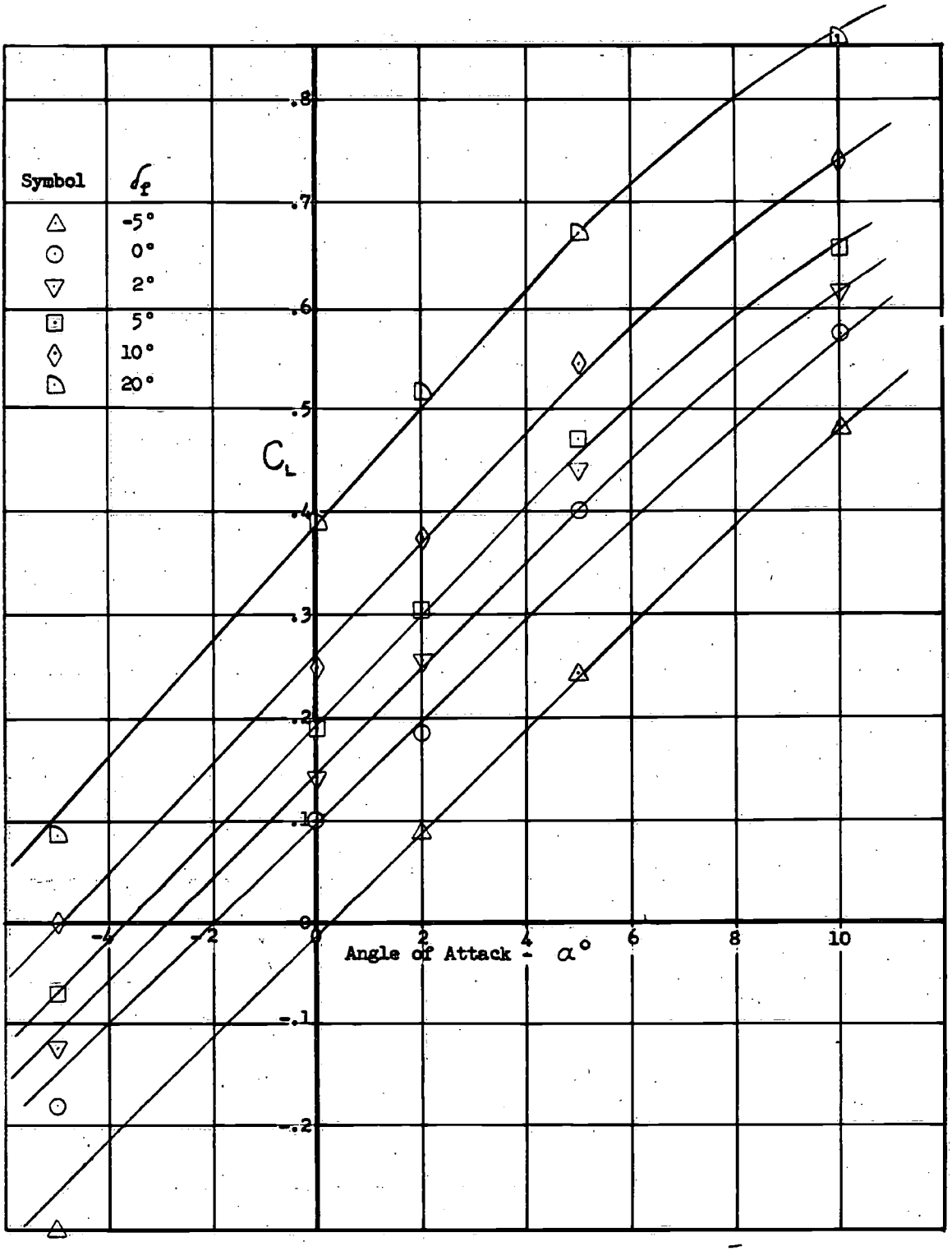

Figure 10. LIFT COEFFICIENT: MODEL CONFIGURATION 2
$c_f/c = 0.3$, $b_f/b = 0.8$, $h/c = 1$

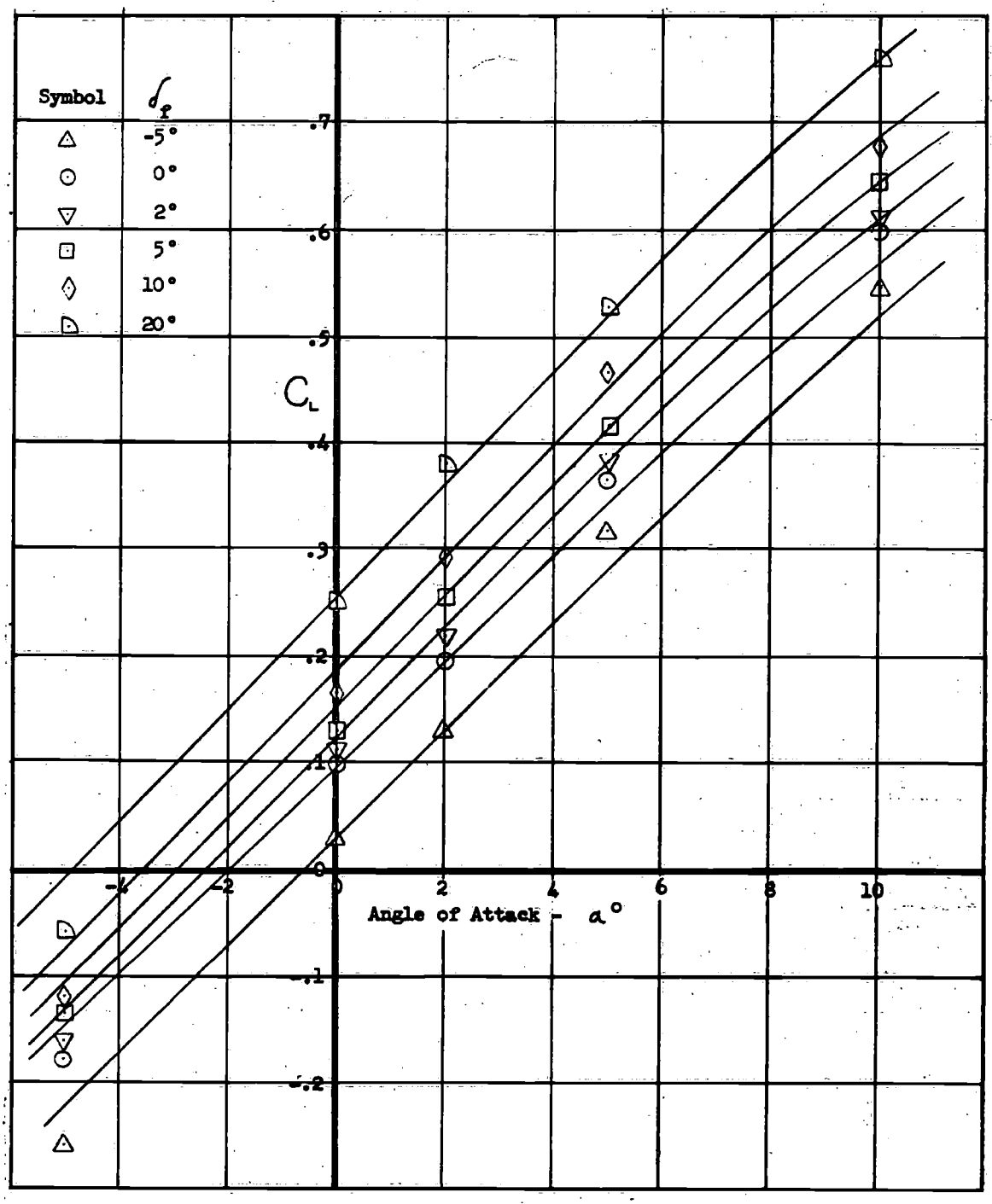

Figure 11. LIFT COEFFICIENT: MODEL CONFIGURATION 3
$c_f/c = 0.2$, $b_f/b = 0.6$, $h/c = 1$

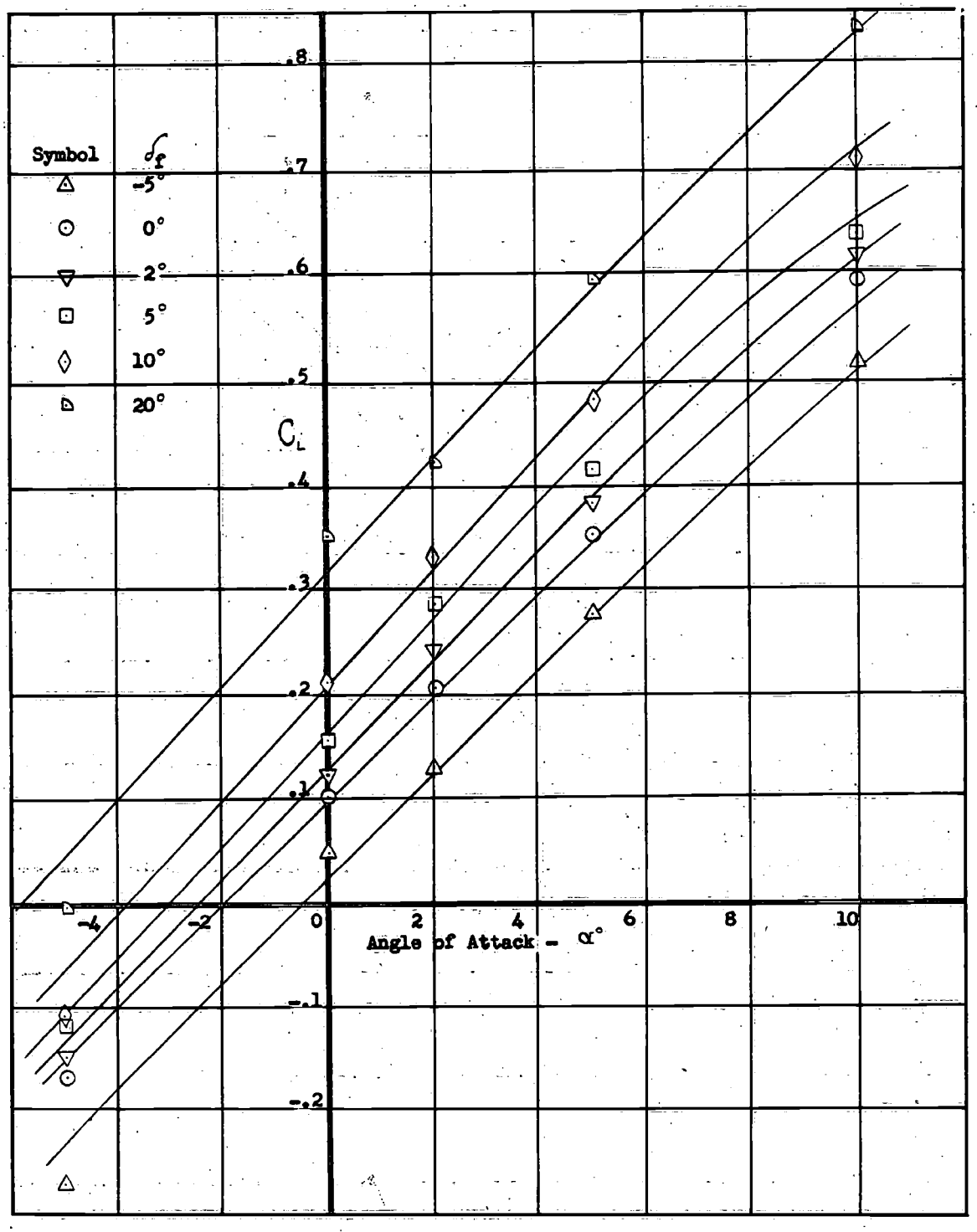

Figure 12. LIFT COEFFICIENT: MODEL CONFIGURATION 4
$c_f/c = 0.2$, $b_f/b = 0.8$, $h/c = 1$

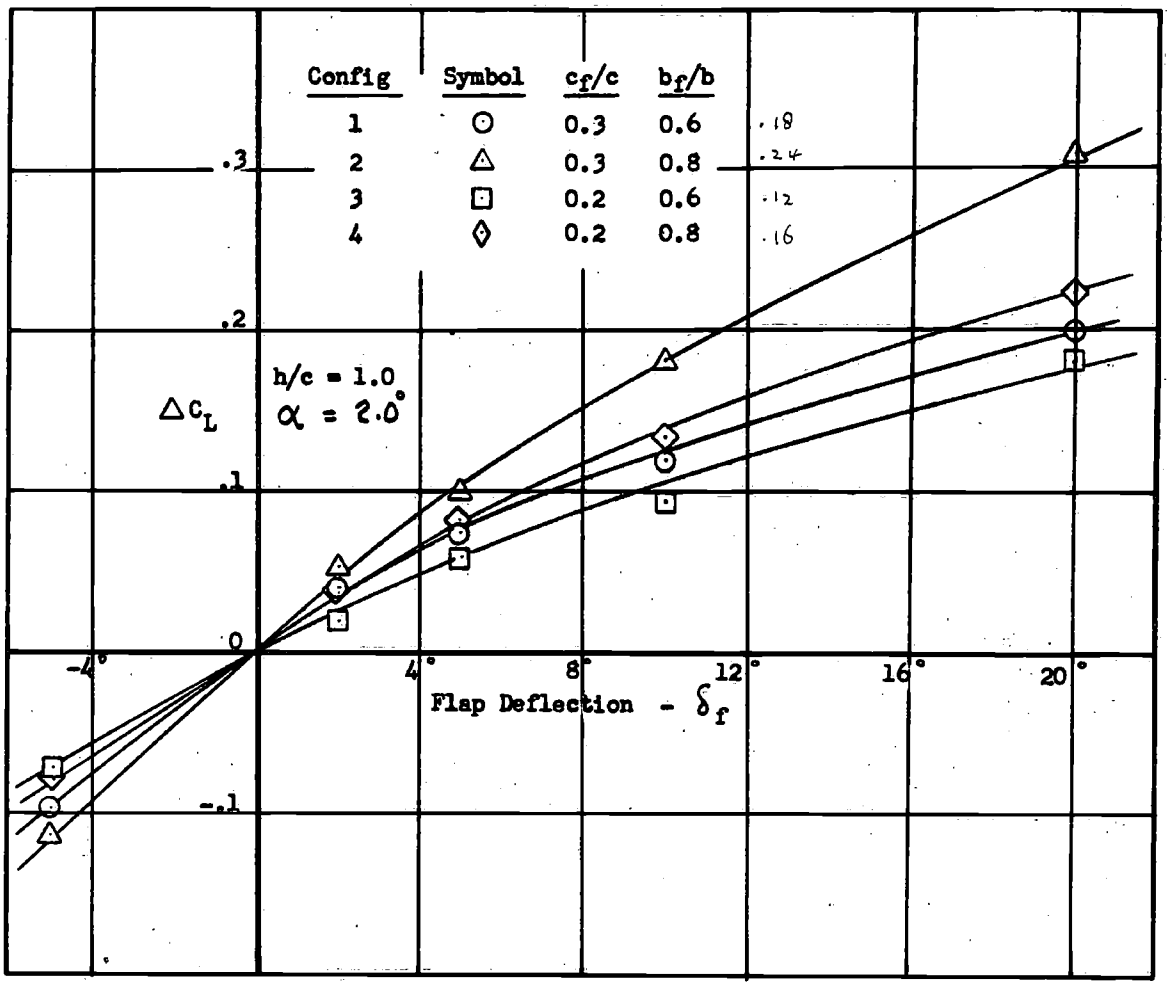

Figure 13. VARIATION OF FLAP EFFECTIVENESS WITH FLAP GEOMETRY

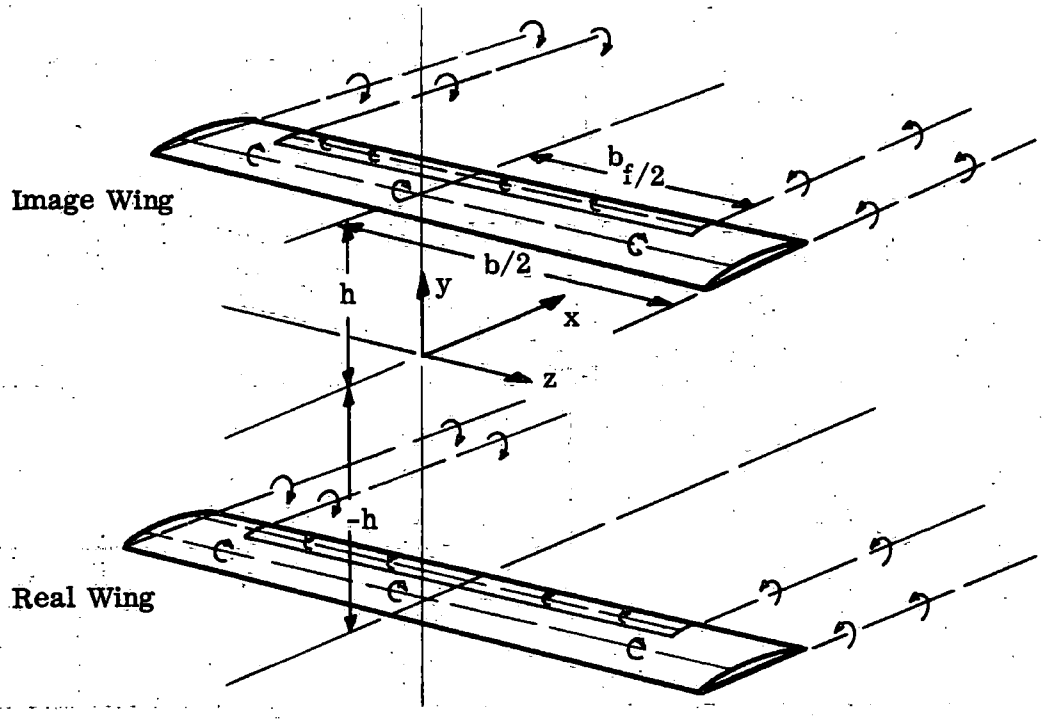

Figure 14. VORTEX ARRANGEMENT REPRESENTING THE REAL AND IMAGE WINGS AND THEIR FLAPS

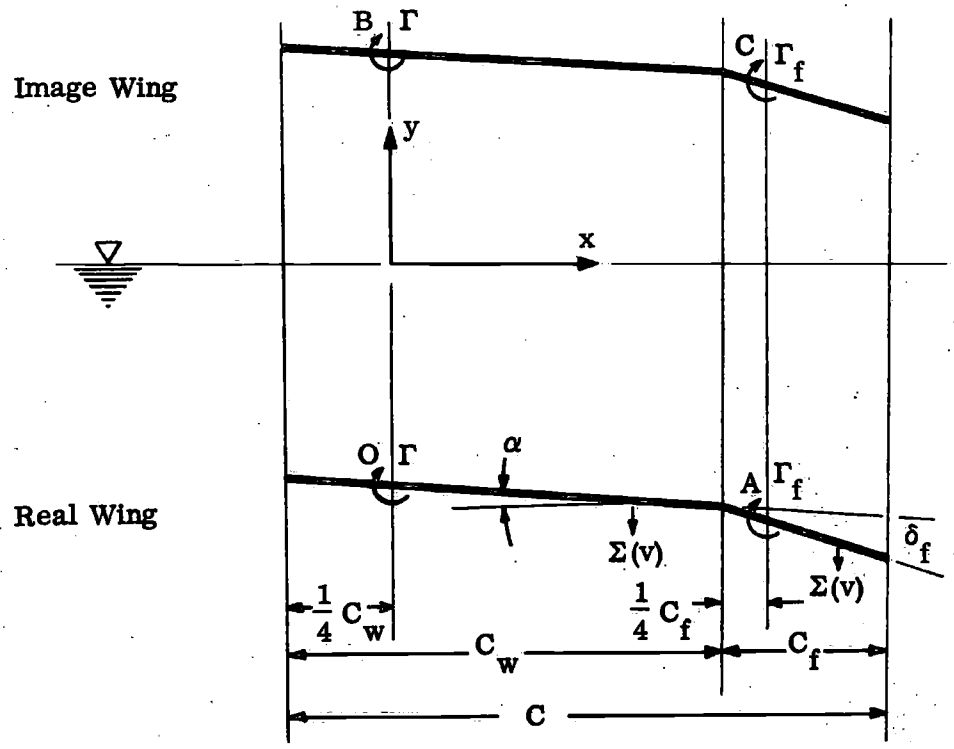

Figure 15. LOCATION OF BOUND VORTICES ON THE WING AND FLAP

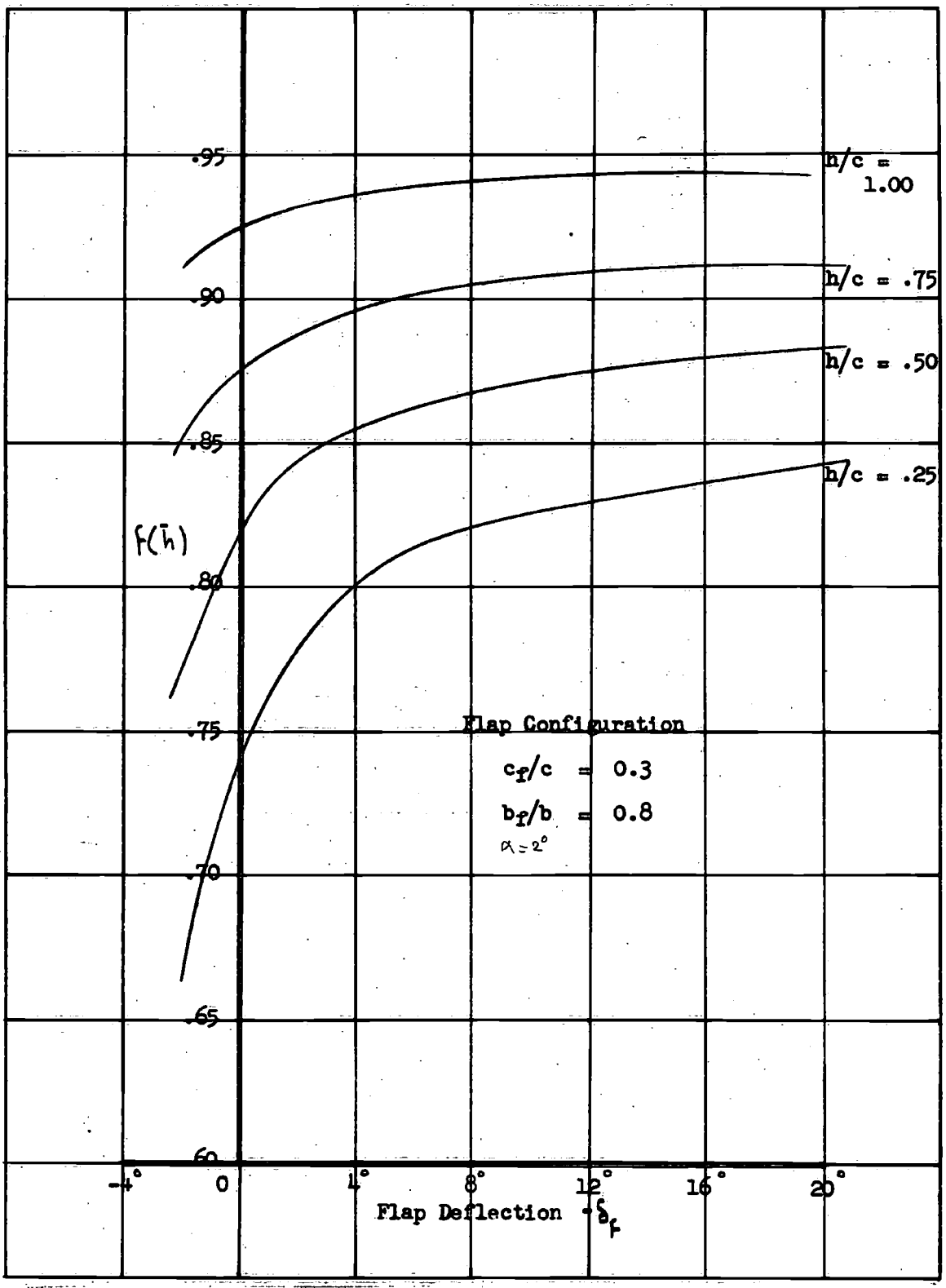

Figure 16. EFFECT OF DEPTH ON FLAP EFFECTIVENESS LINEARIZED THEORY (3-DIMENSIONAL)

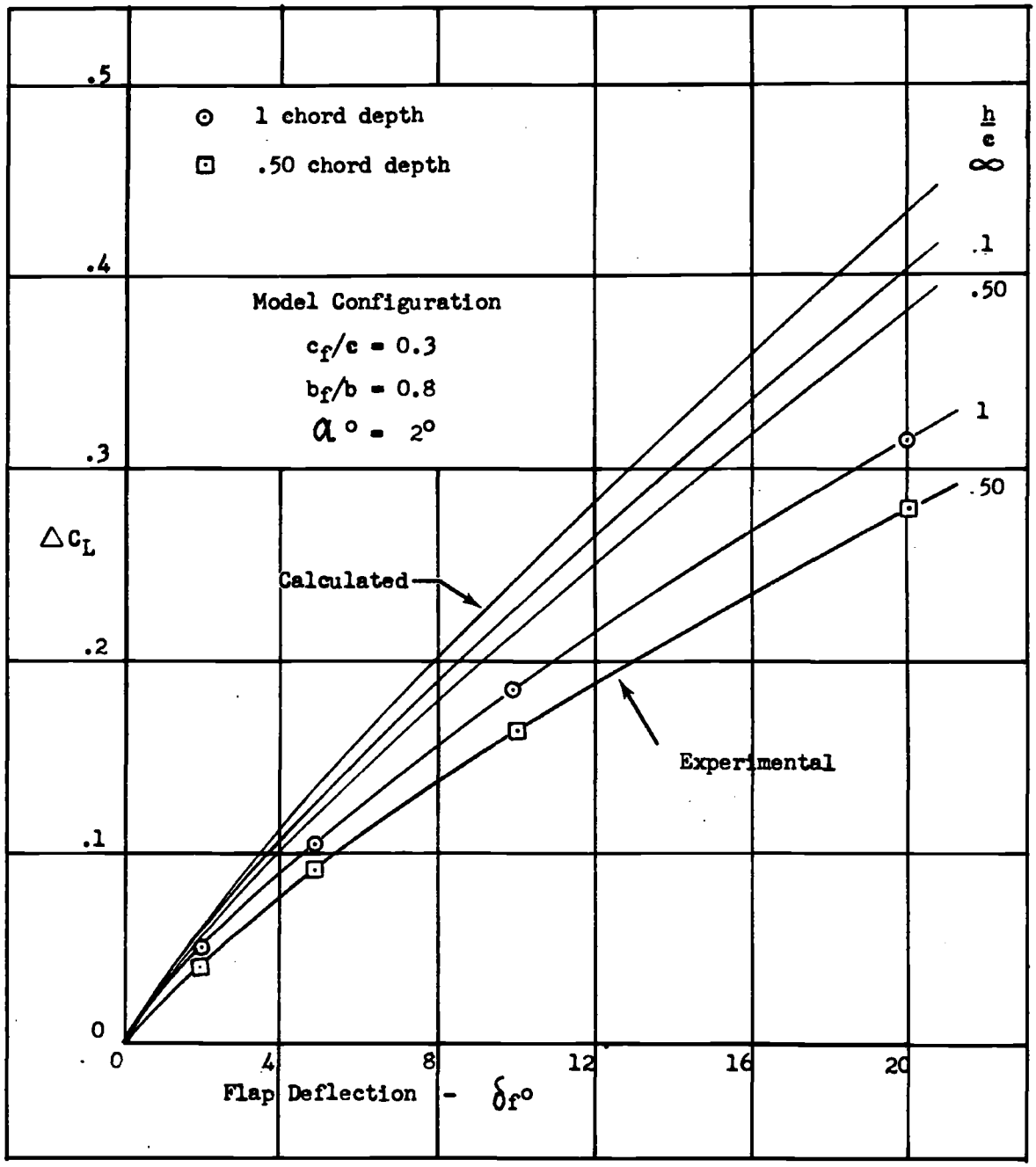

Figure 17. FLAP EFFECTIVENESS AT VARIOUS DEPTHS - COMPARISON OF THEORY WITH EXPERIMENT MODEL CONFIGURATION 2

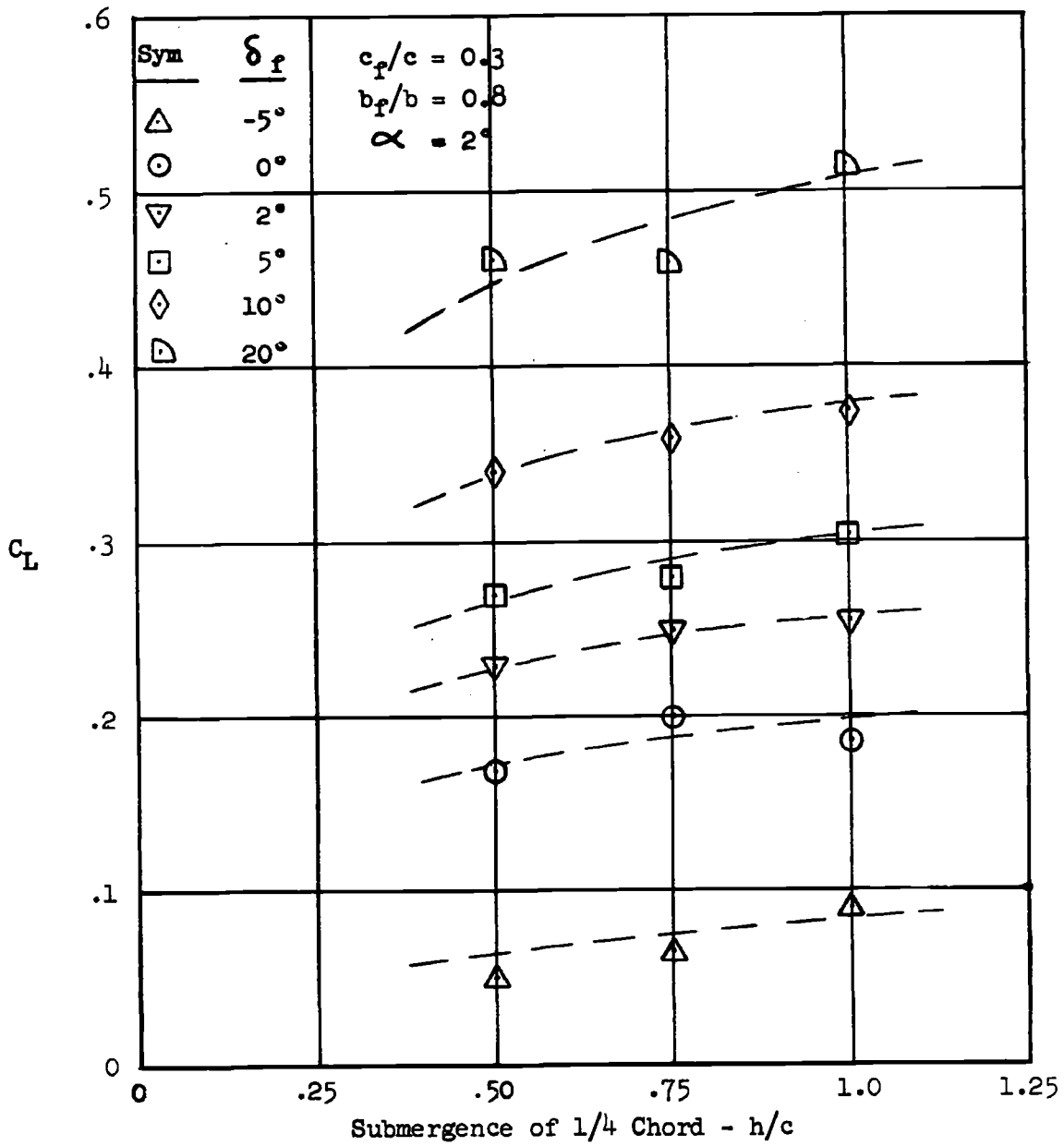

Figure 18. EFFECT OF DEPTH ON C_L. MODEL CONFIGURATION 2

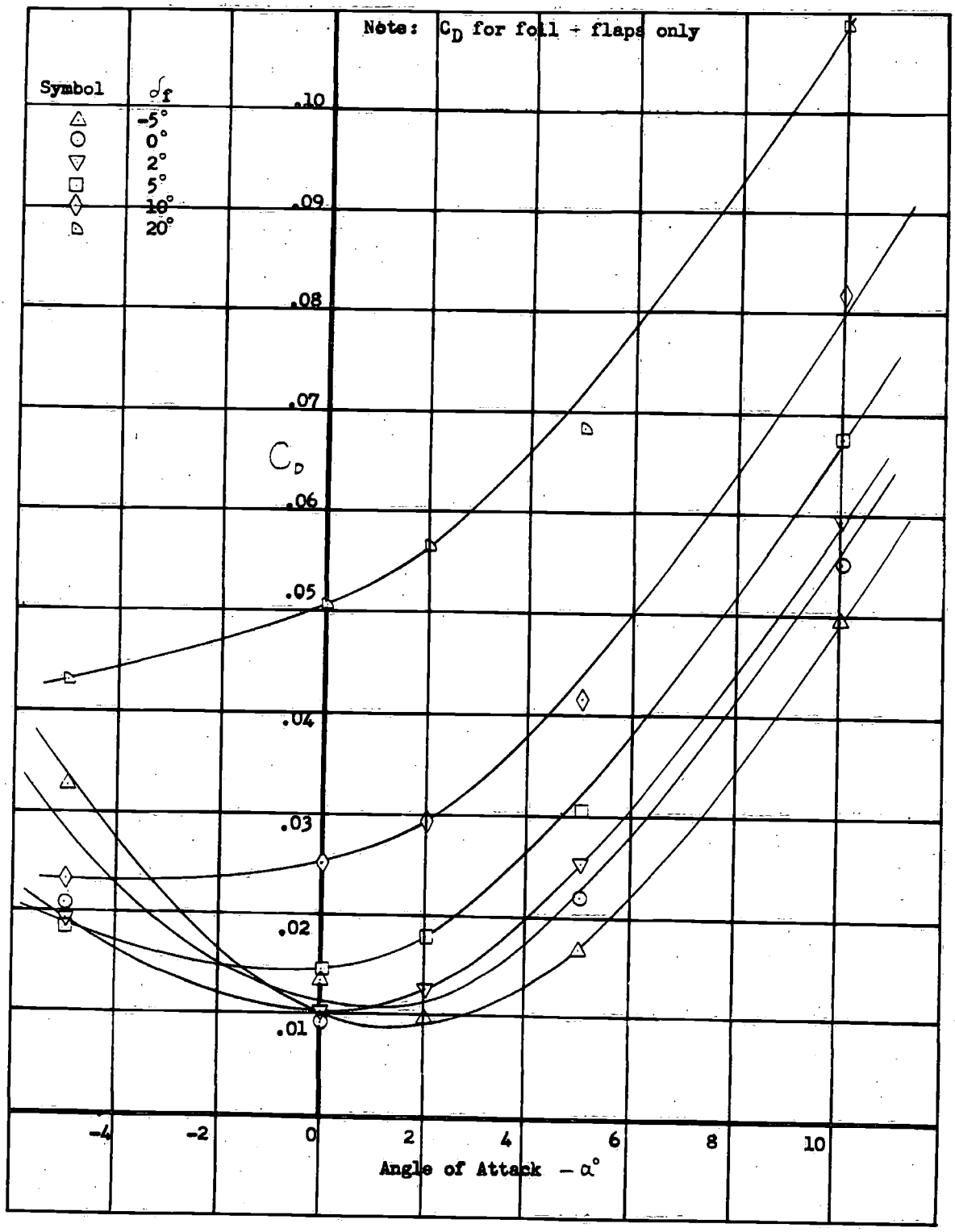

Figure 19. DRAG COEFFICIENT: MODEL CONFIGURATION 1
$c_f/c = 0.3$, $b_f/b = 0.6$, $h/c = 1$

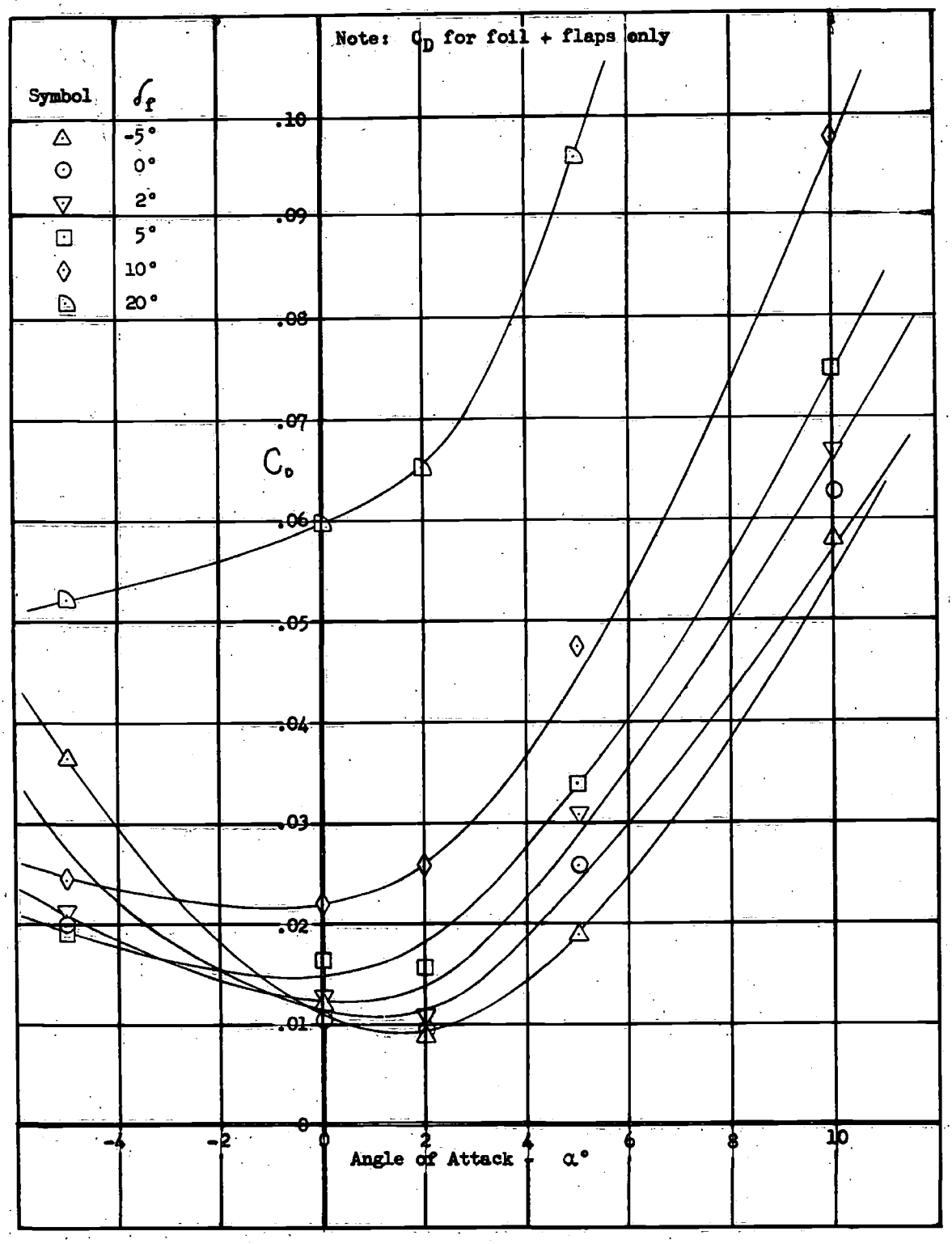

Figure 20. DRAG COEFFICIENT: MODEL CONFIGURATION 2
$c_f/c = 0.3$, $b_f/b = 0.8$, $h/c = 1$

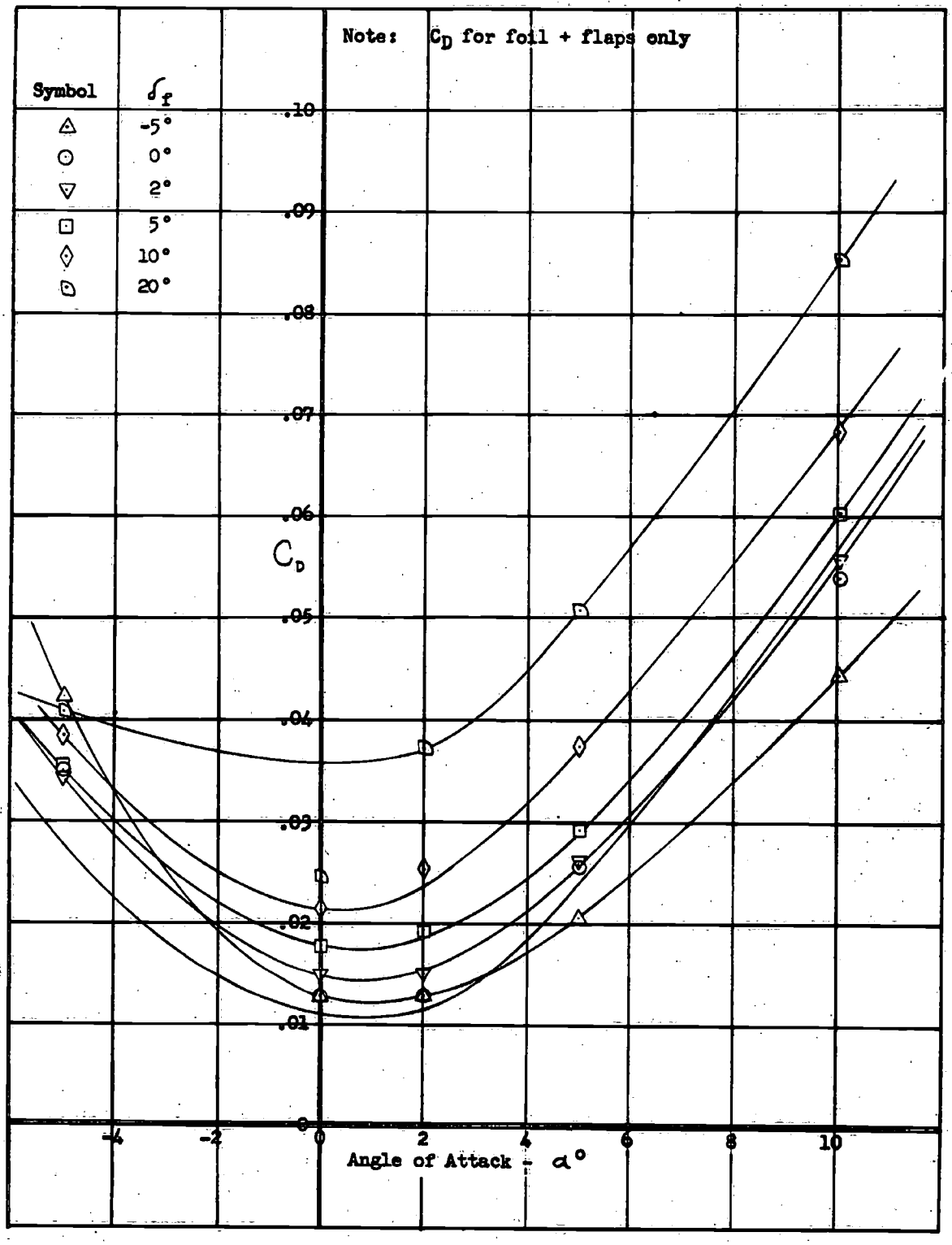

Figure 21. DRAG COEFFICIENT: MODEL CONFIGURATION 3
$c_f/c = 0.2$, $b_f/c = 0.6$, $h/c = 1$

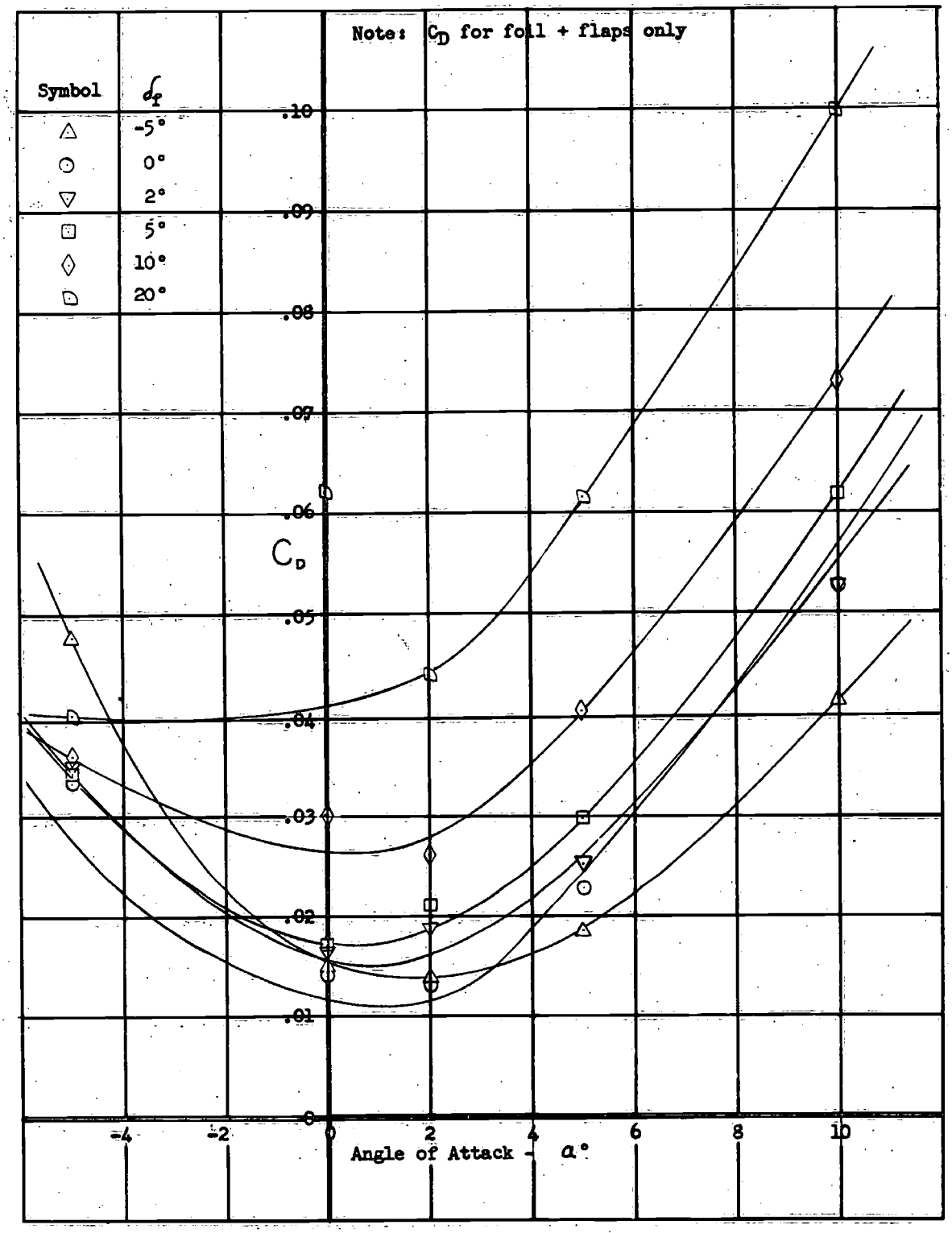

Figure 22. DRAG COEFFICIENT: MODEL CONFIGURATION 4
$c_f/c = 0.2$, $b_f/b = 0.8$, $h/c = 1$

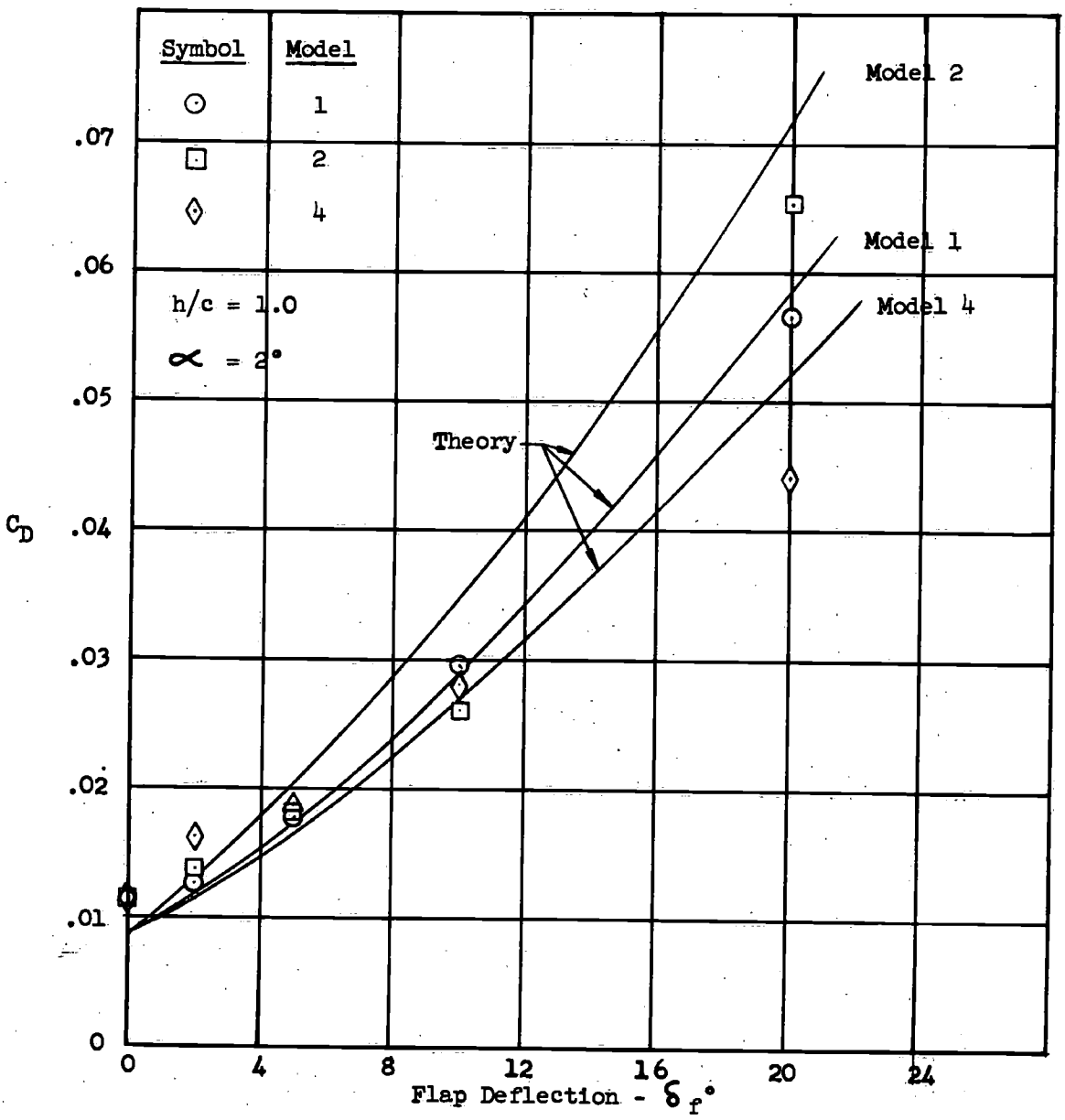

Figure 23. DRAG COEFFICIENT - COMPARISON BETWEEN THEORY AND EXPERIMENT

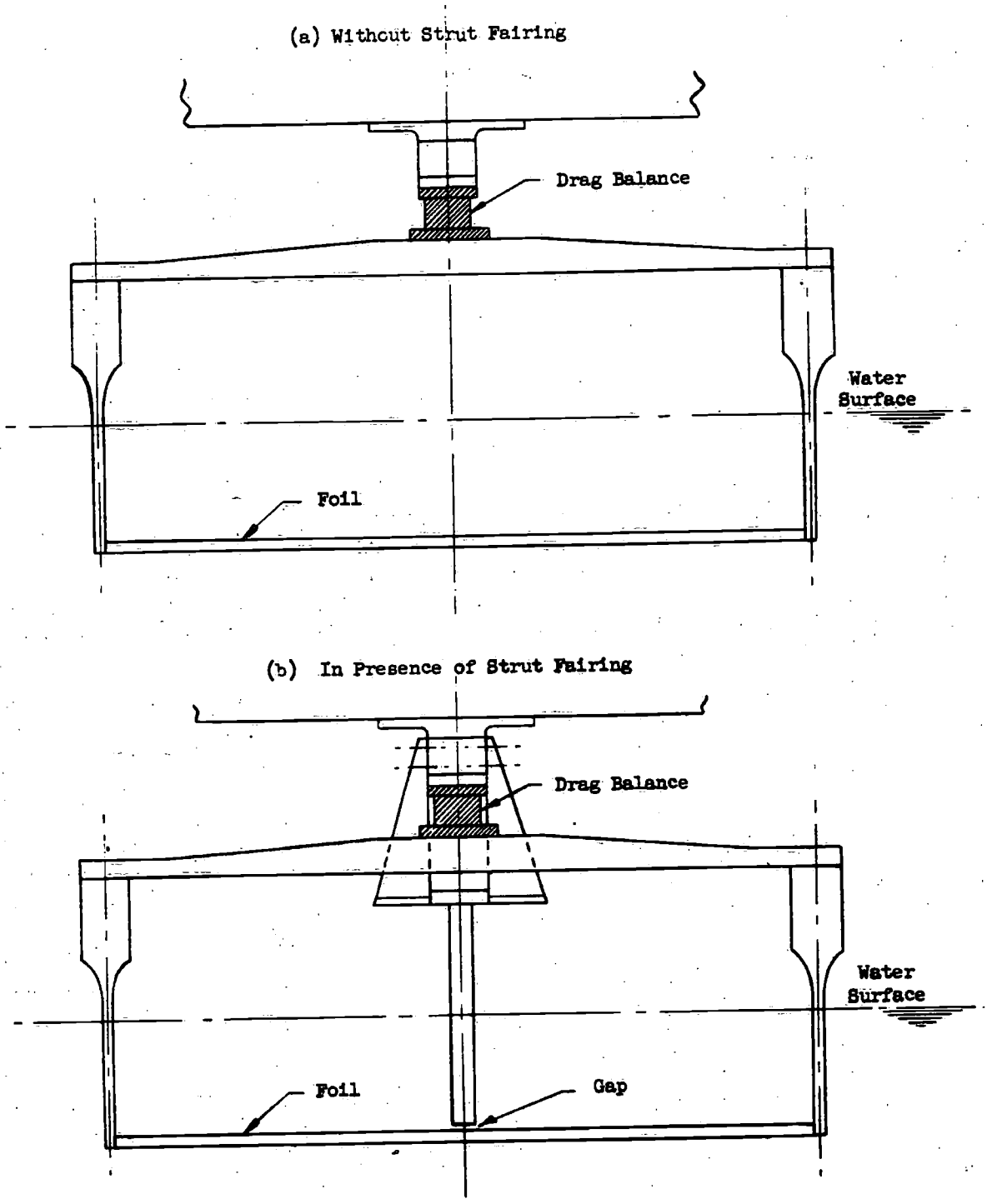

Figure 24. MOUNTING ARRANGEMENT FOR DETERMINING STRUT-WING INTERFERENCE DRAG

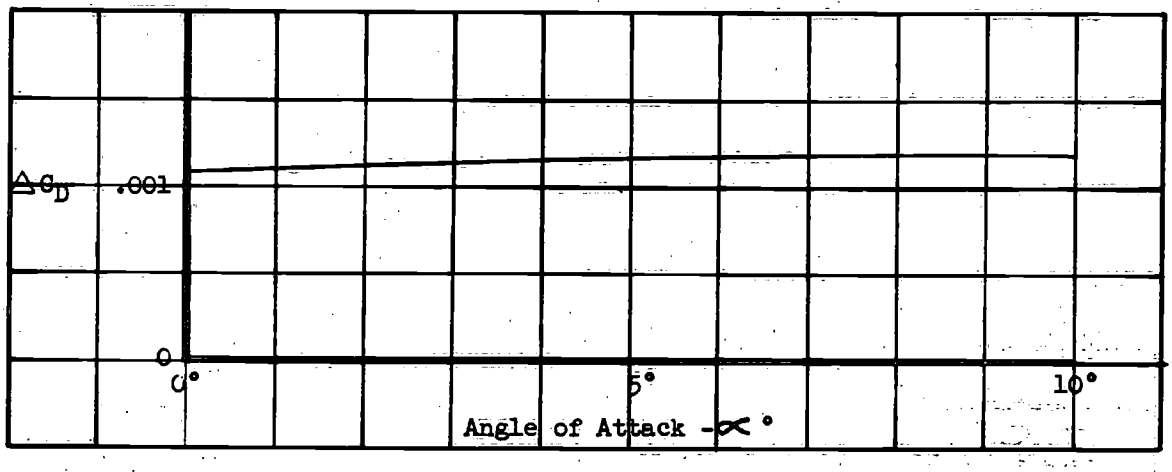

Figure 25. STRUT-WING INTERFERENCE DRAG COEFFICIENT

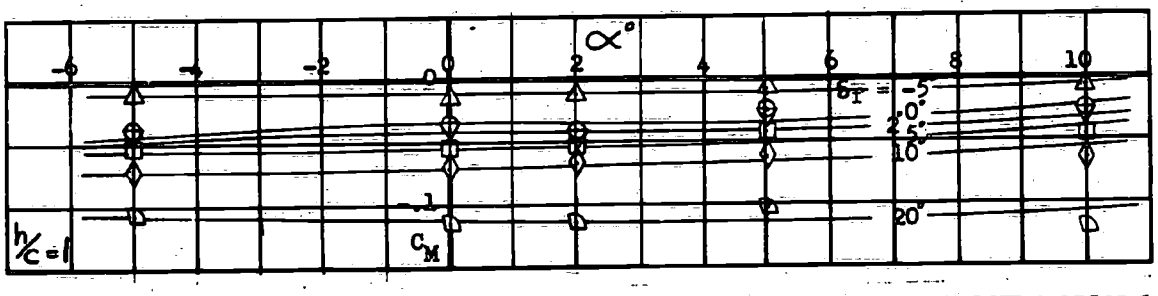

Figure 26. PITCHING MOMENT COEFFICIENT - MODEL CONFIGURATION 1
$c_f/c = 0.3$, $b_f/b = 0.6$

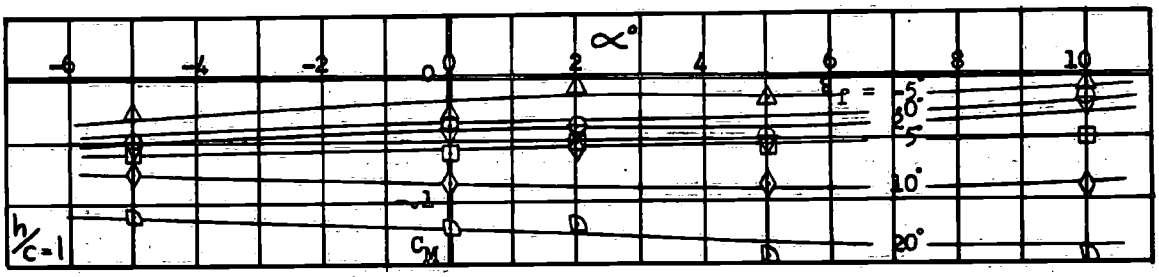

Figure 27. PITCHING MOMENT COEFFICIENT - MODEL CONFIGURATION 2
$c_f/c = 0.3$, $b_f/b = 0.8$

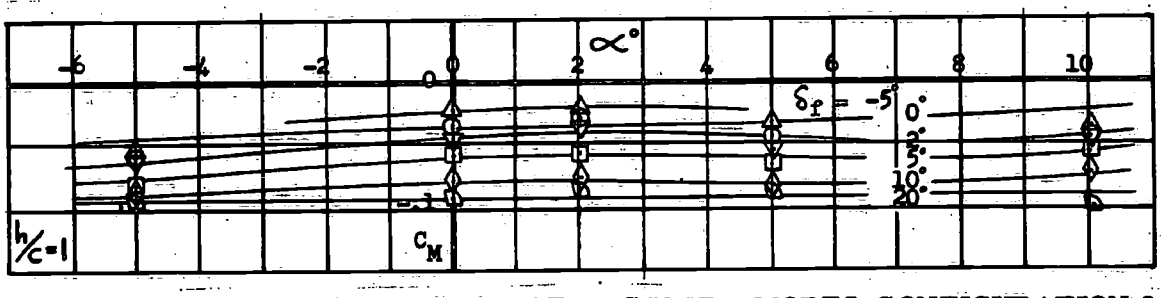

Figure 28. PITCHING MOMENT COEFFICIENT - MODEL CONFIGURATION 3
$c_f/c = 0.2$, $b_f/b = 0.6$

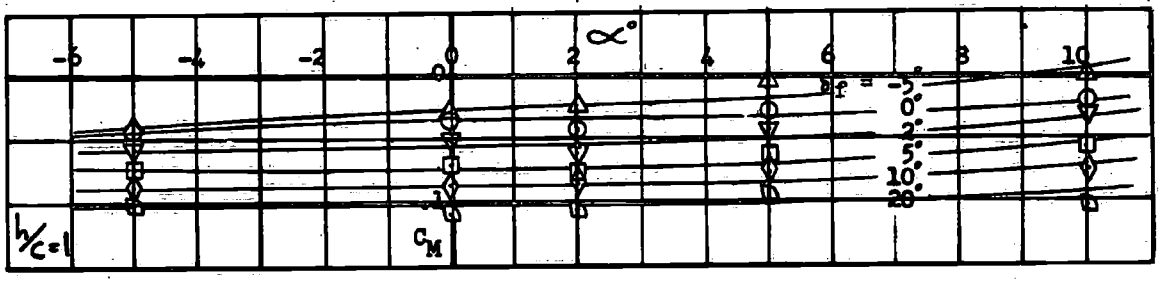

Figure 29. PITCHING MOMENT COEFFICIENT - MODEL CONFIGURATION 4
$c_f/c = 0.2$, $b_f/b = 0.8$

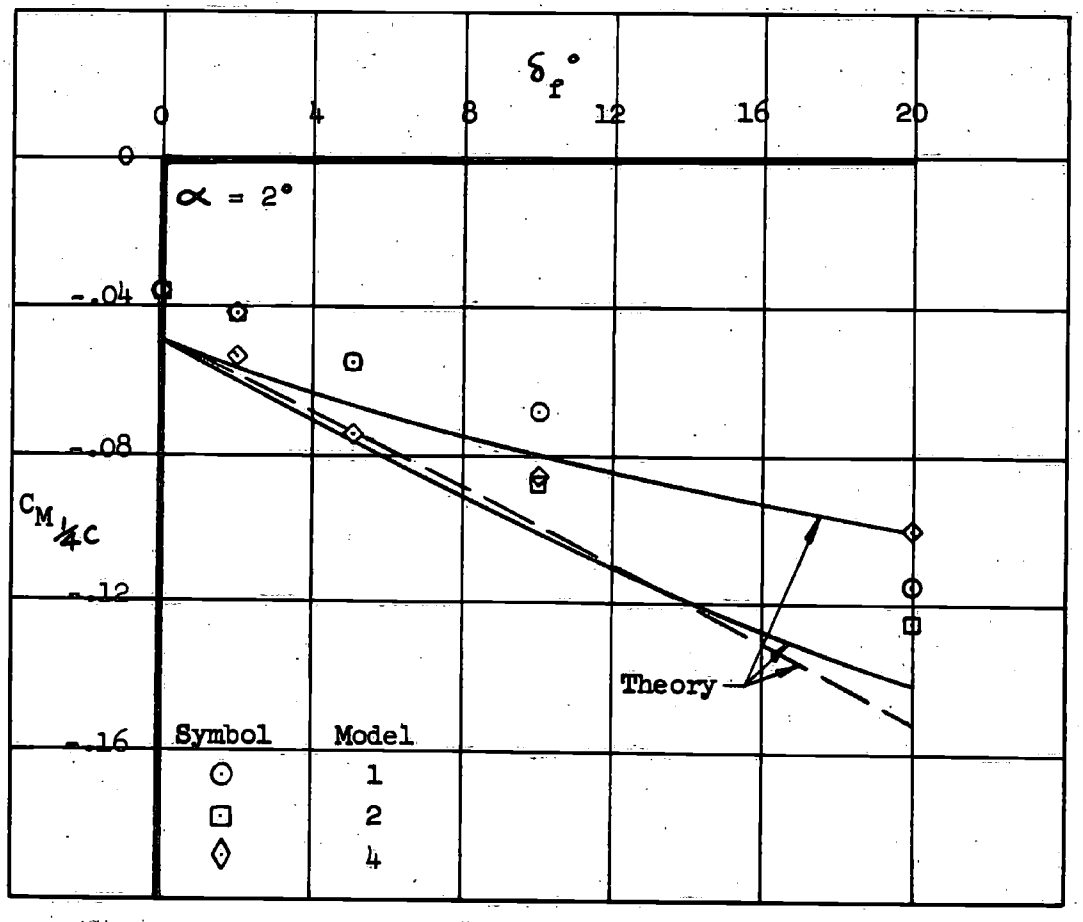

Figure 30. PITCHING MOMENT COEFFICIENT - COMPARISON WITH THEORY

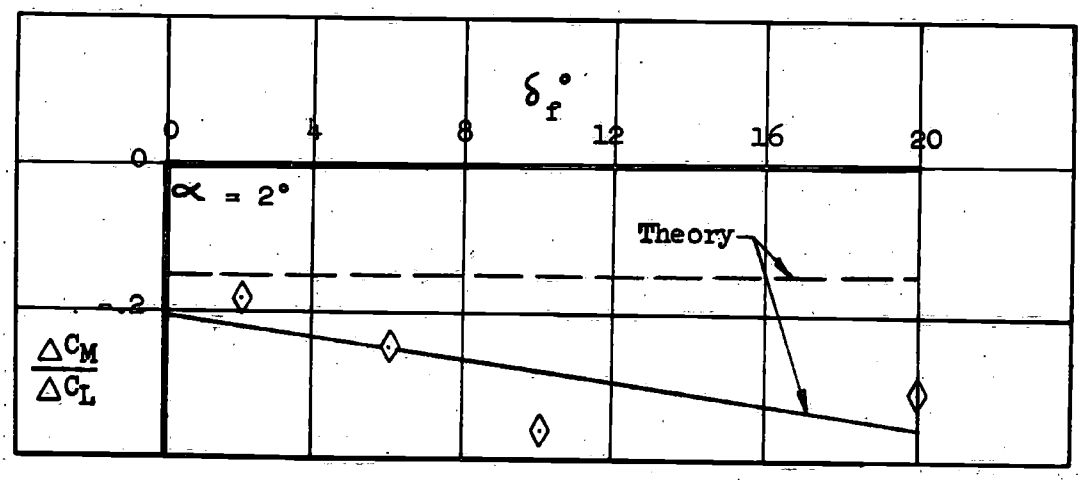

Figure 31. RATIO OF CHANGE OF PITCHING MOMENT COEFFICIENT WITH CHANGE IN LIFT COEFFICIENT

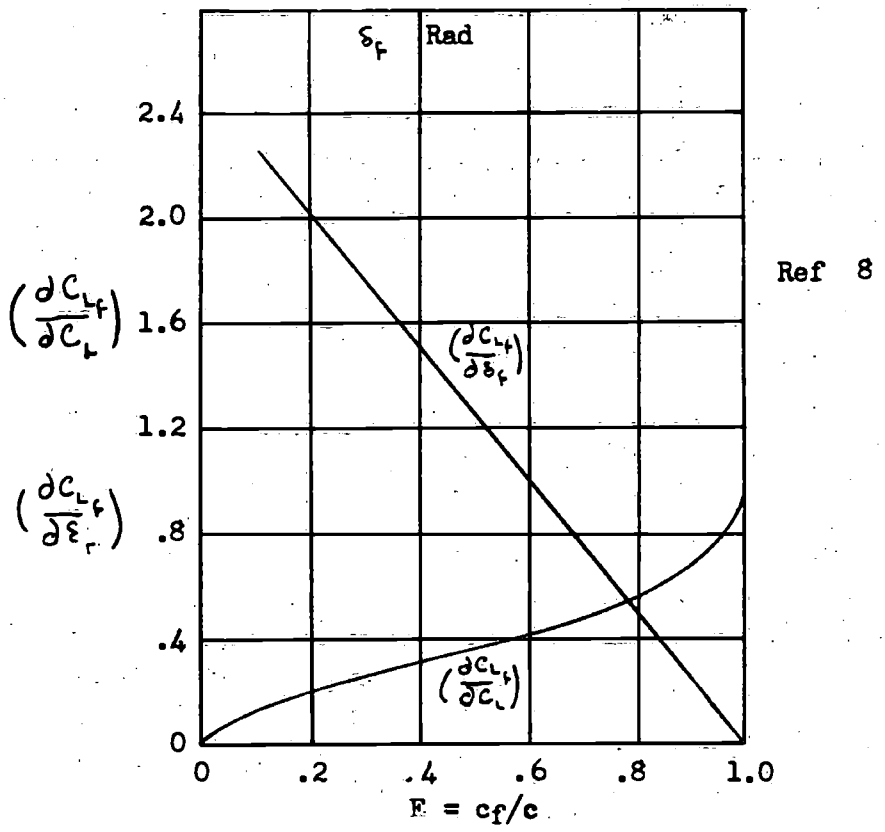

Figure 32. VARIATION OF FLAP LIFT COEFFICIENT PARAMETERS WITH FLAP CHORD RATIO

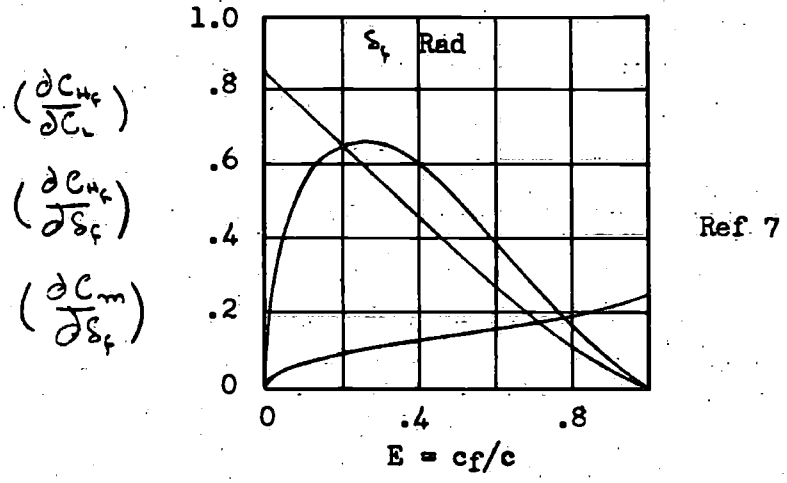

Figure 33. VARIATION OF FLAP HINGE MOMENT COEFFICIENT AND THIN WING MOMENT COEFFICIENT PARAMETERS WITH FLAP CHORD RATIO

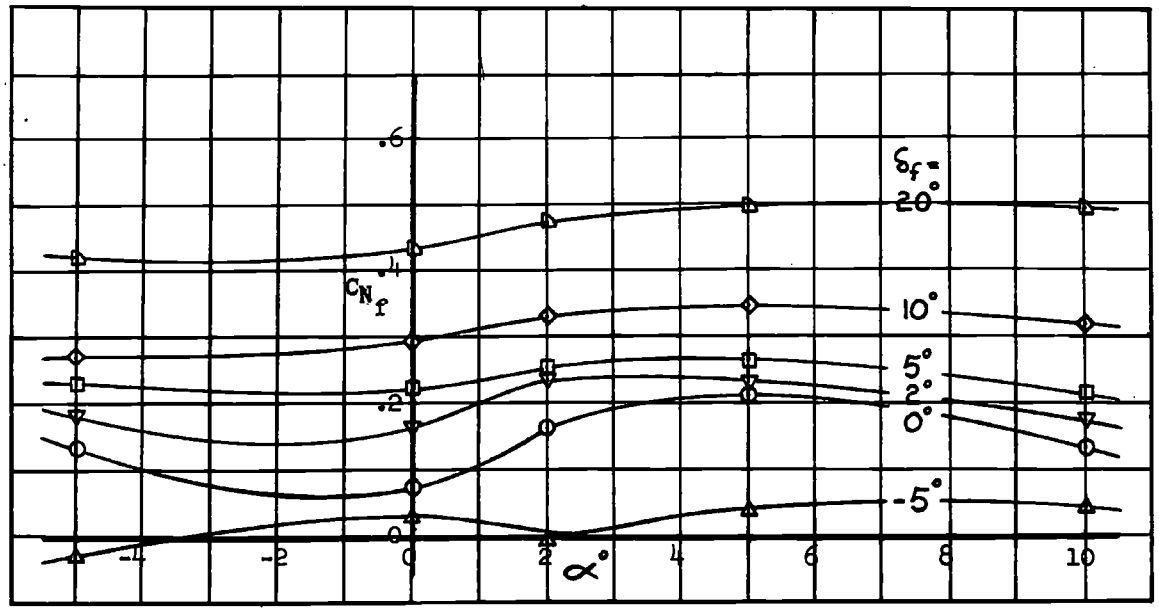

Figure 34. FLAP NORMAL FORCE COEFFICIENT - CONFIGURATION 1
$c_f/c = 0.3$, $b_f/b = 0.6$, $h/c = 1$

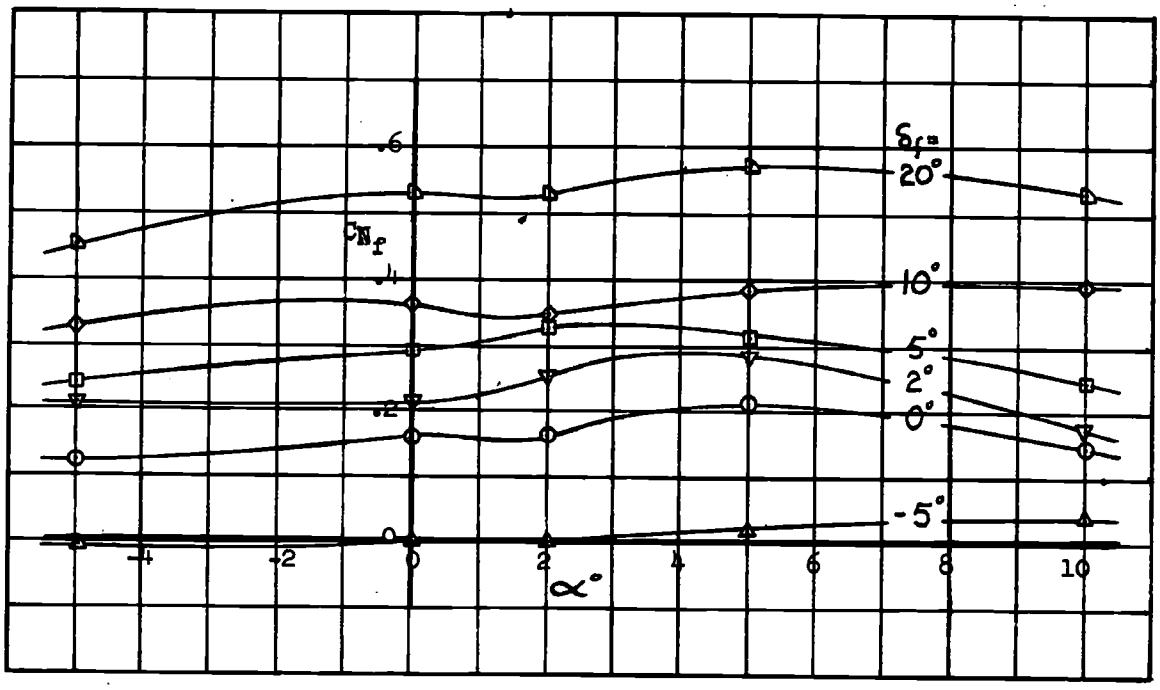

Figure 35. FLAP NORMAL FORCE COEFFICIENT - CONFIGURATION 2
$c_f/c = 0.3$, $b_f/b = 0.8$, $h/c = 1$

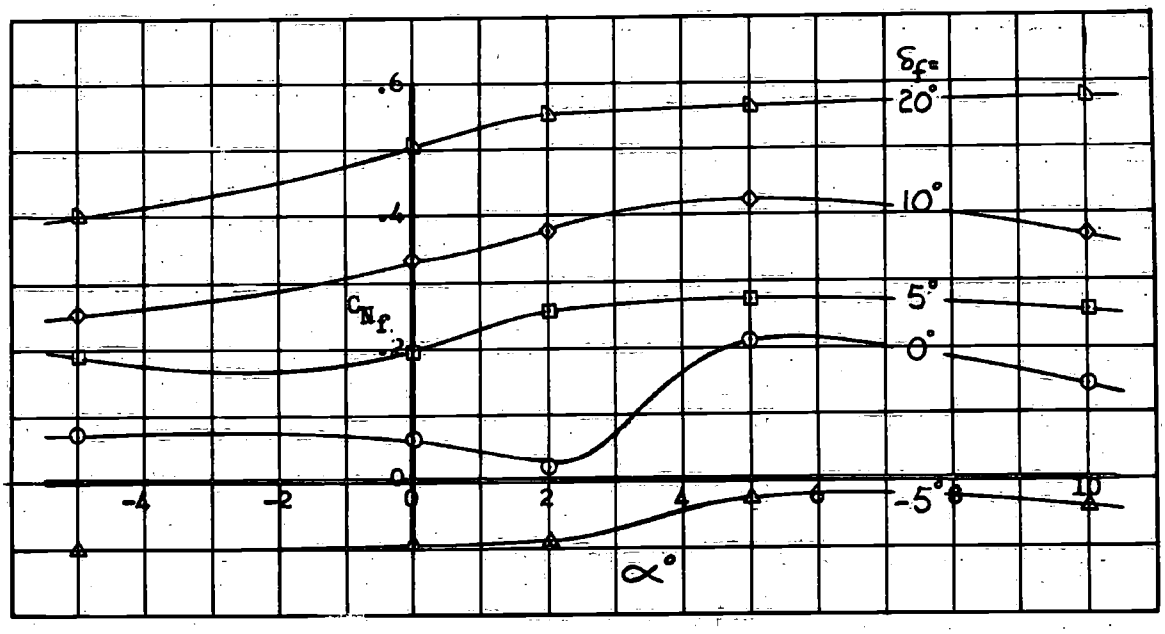

Figure 36. FLAP NORMAL FORCE COEFFICIENT - CONFIGURATION 3
$c_f/c = 0.2$, $b_f/b = 0.6$, $h/c = 1$

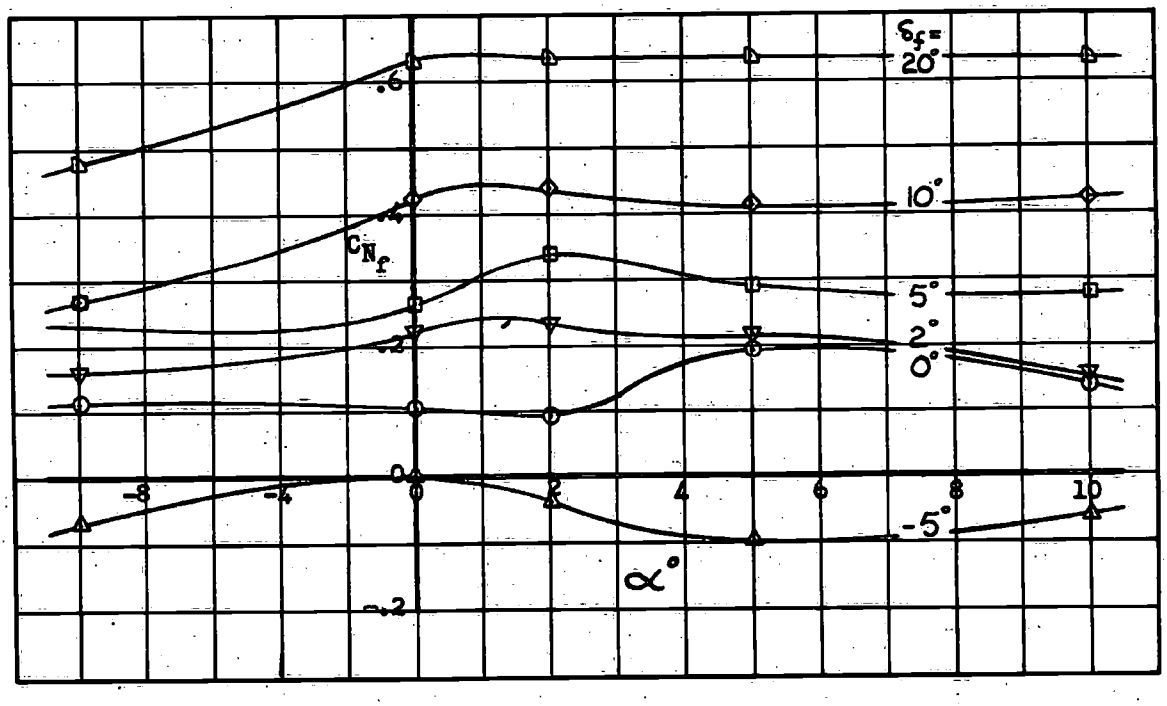

Figure 37. FLAP NORMAL FORCE COEFFICIENT - CONFIGURATION 4
$c_f/c = 0.2$, $b_f/b = 0.8$, $h/c = 1$

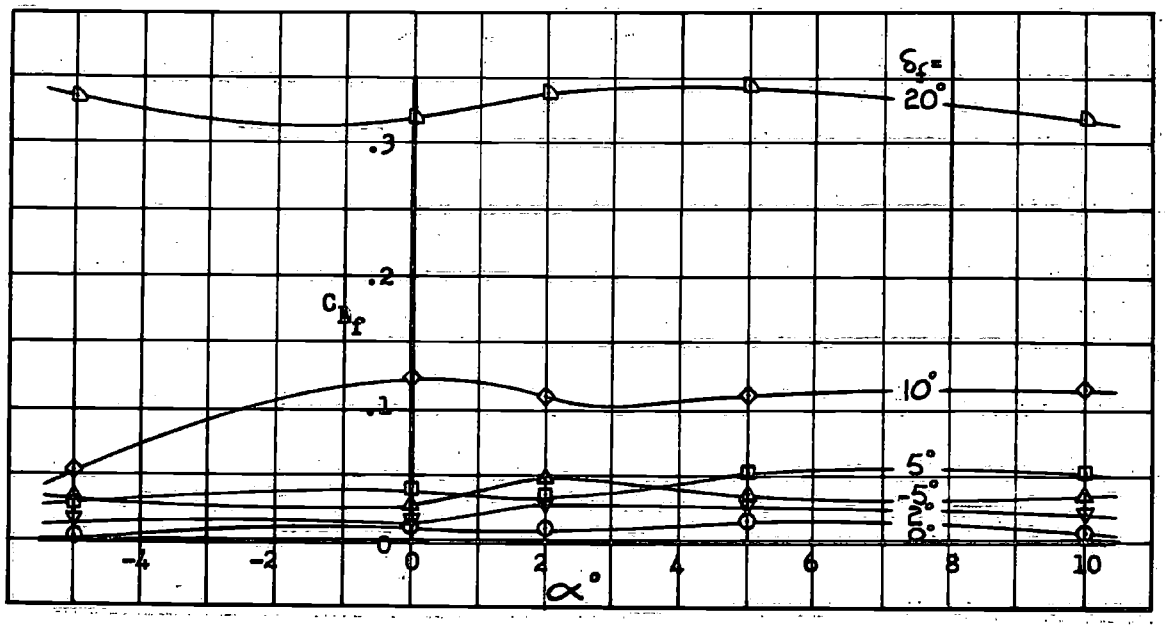

Figure 38. FLAP AXIAL FORCE COEFFICIENT - CONFIGURATION 1
$c_f/c = 0.3$, $b_f/b = 0.6$, $h/c = 1$

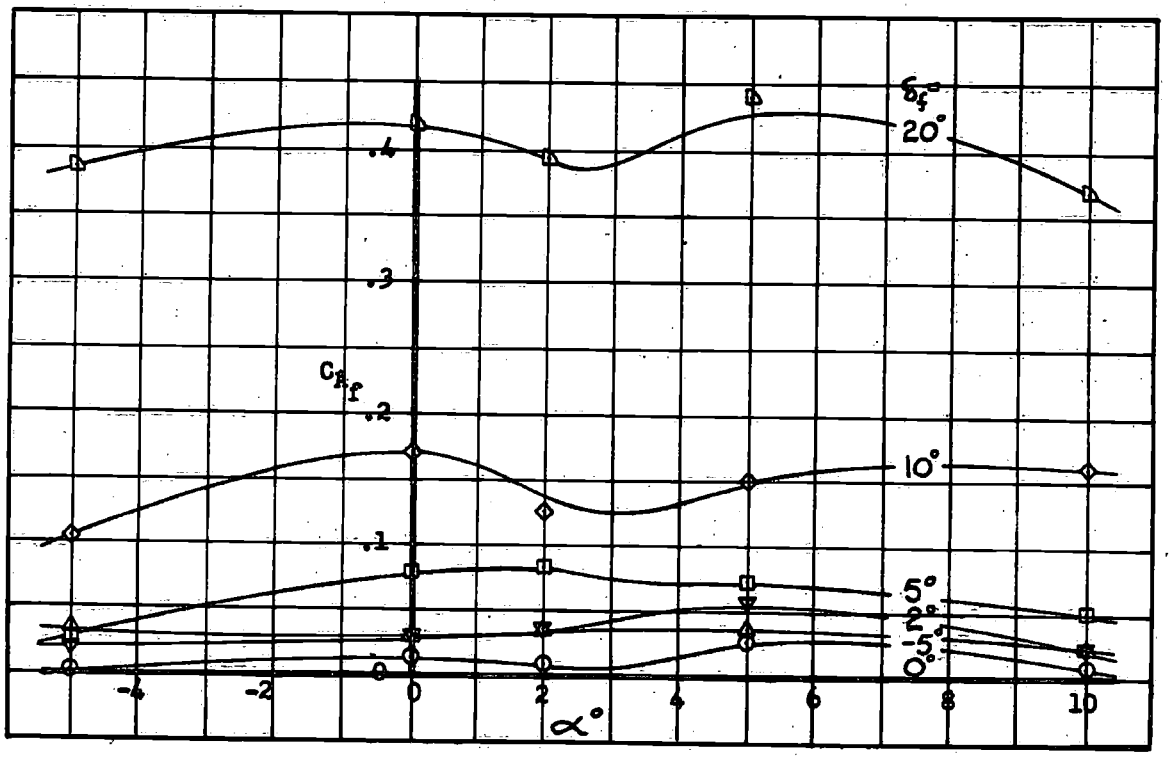

Figure 39. FLAP AXIAL FORCE COEFFICIENT - CONFIGURATION 2
$c_f/c = 0.3$, $b_f/b = 0.8$, $h/c = 1$

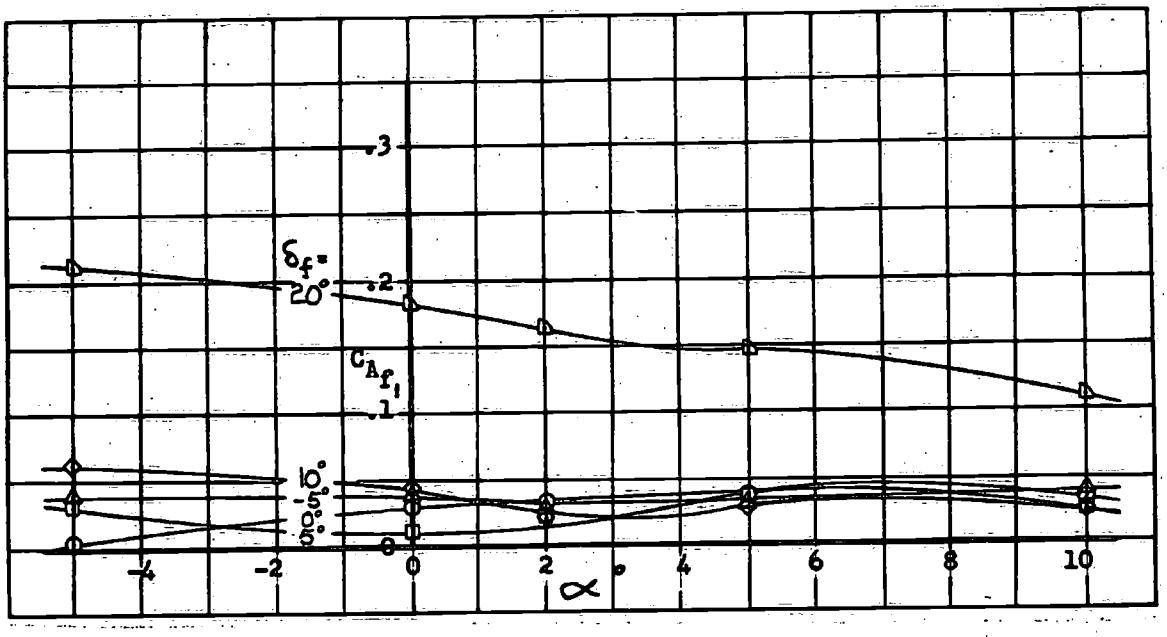

Figure 40. FLAP AXIAL FORCE COEFFICIENT - CONFIGURATION 3
$c_f/c = 0.2$, $b_f/b = 0.6$, $h/c = 1$

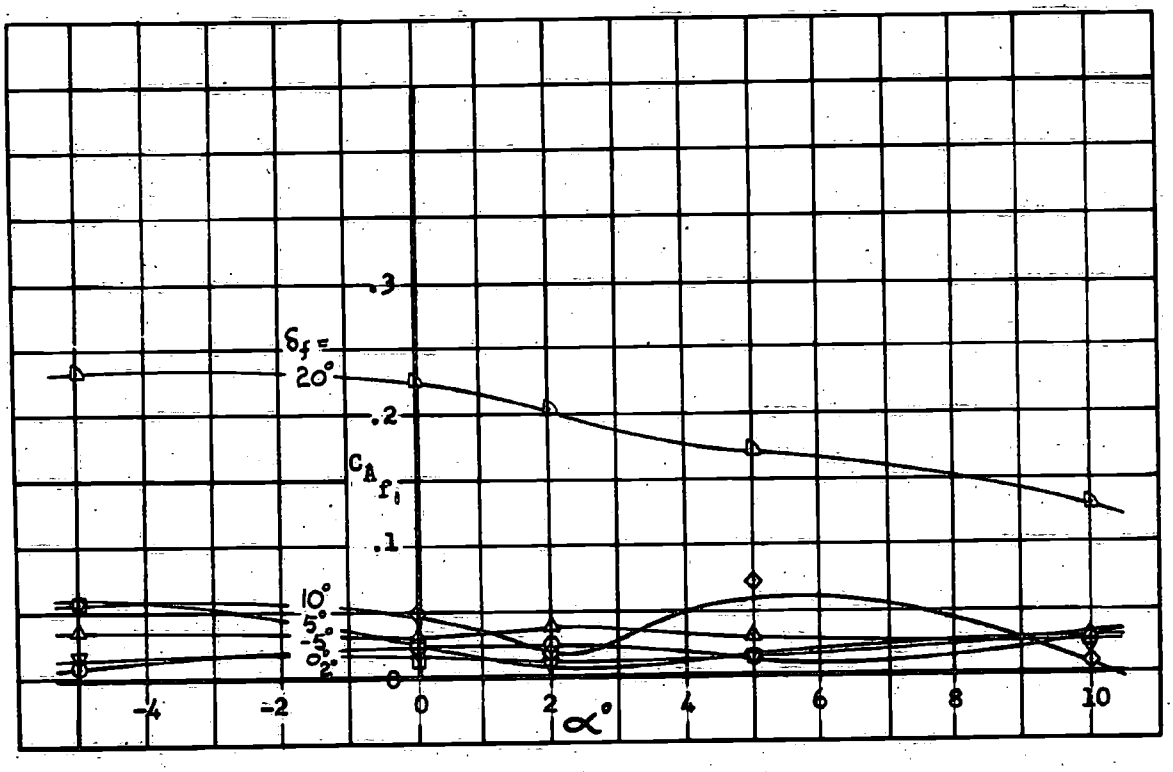

Figure 41. FLAP AXIAL FORCE COEFFICIENT - CONFIGURATION 4
$c_f/c = 0.2$, $b_f/b = 0.8$, $h/c = 1$

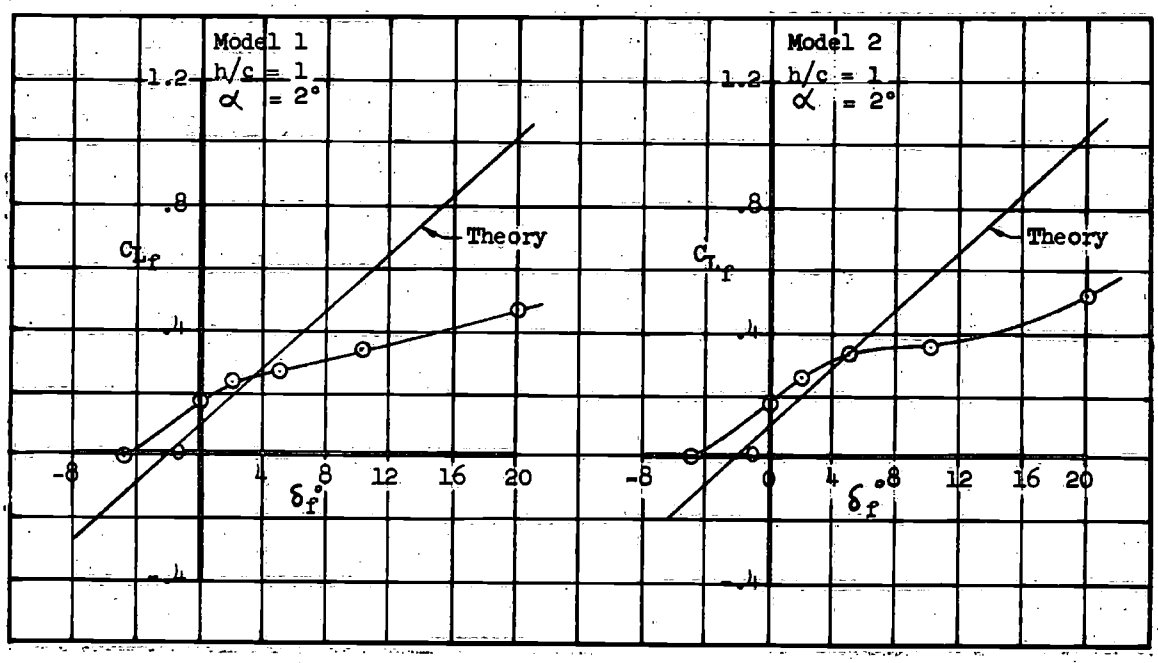

Figure 42. FLAP LIFT COEFFICIENT - COMPARISON WITH THEORY MODEL CONFIGURATIONS 1 AND 2

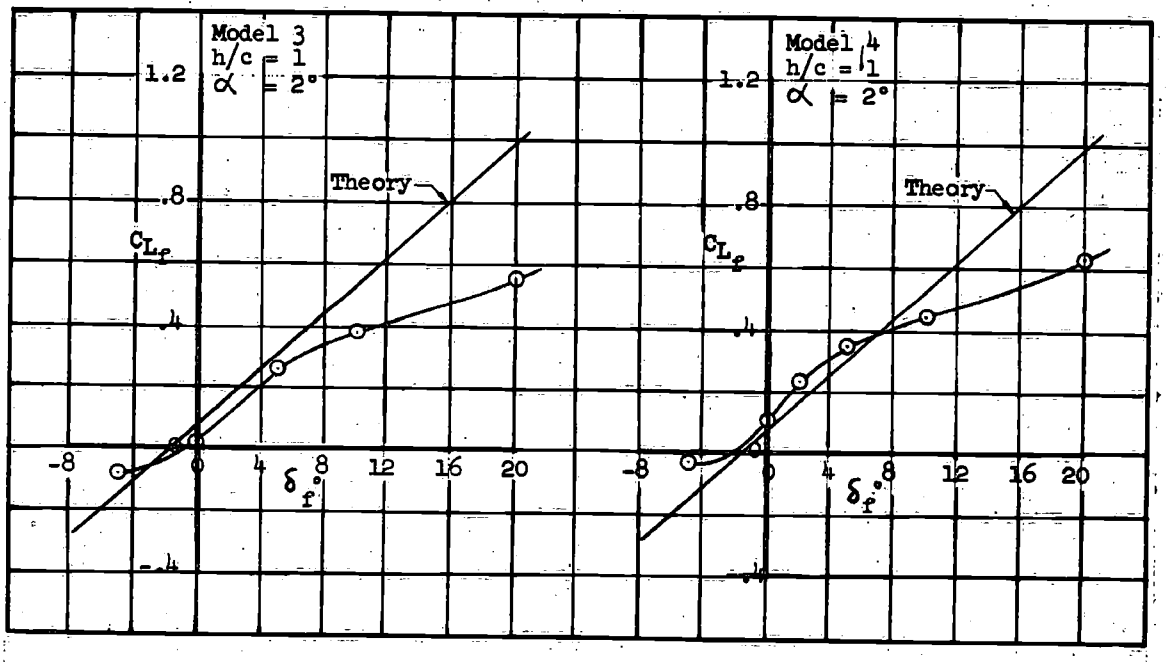

Figure 43. FLAP LIFT COEFFICIENT - COMPARISON WITH THEORY MODEL CONFIGURATIONS 3 AND 4

FLAP HINGE MOMENT COEFFICIENT

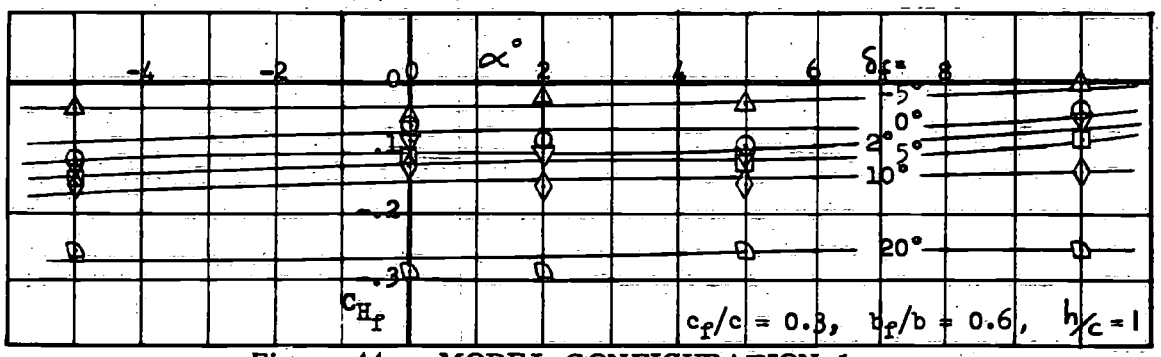

Figure 44. MODEL CONFIGURATION 1
$c_f/c = 0.3$, $b_f/b = 0.6$, $h/c = 1$

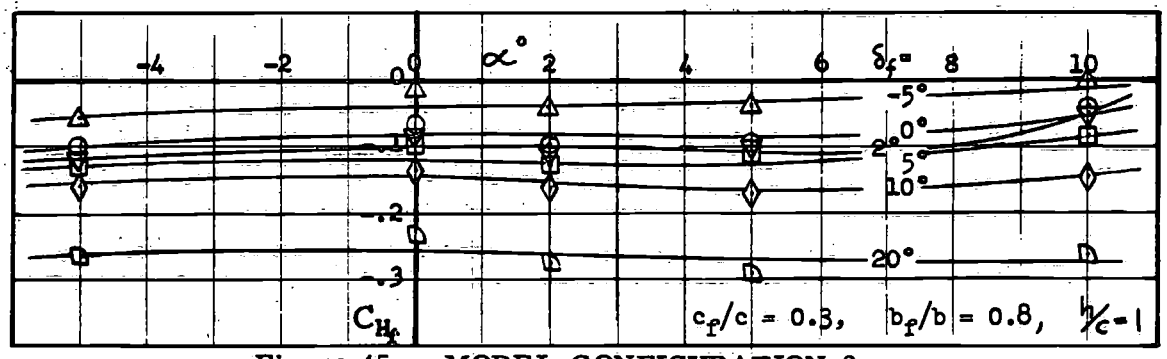

Figure 45. MODEL CONFIGURATION 2
$c_f/c = 0.3$, $b_f/b = 0.8$, $h/c = 1$

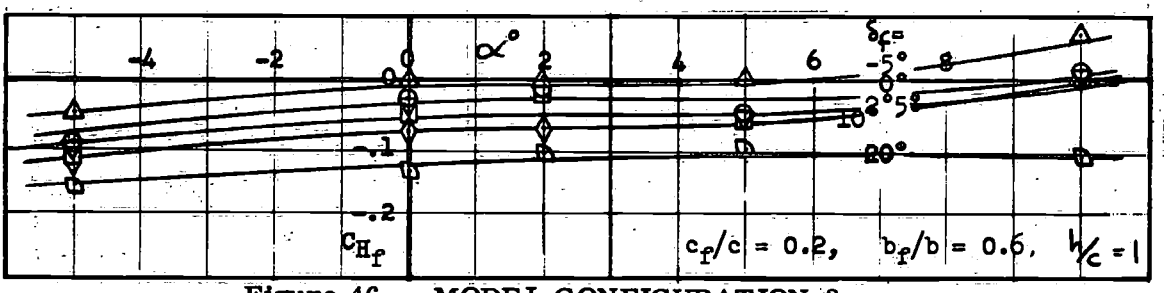

Figure 46. MODEL CONFIGURATION 3
$c_f/c = 0.2$, $b_f/b = 0.6$, $h/c = 1$

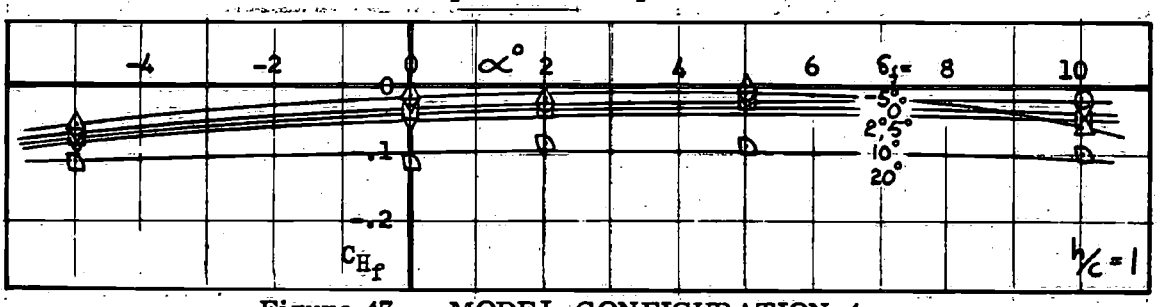

Figure 47. MODEL CONFIGURATION 4
$c_f/c = 0.2$, $b_f/b = 0.8$, $h/c = 1$

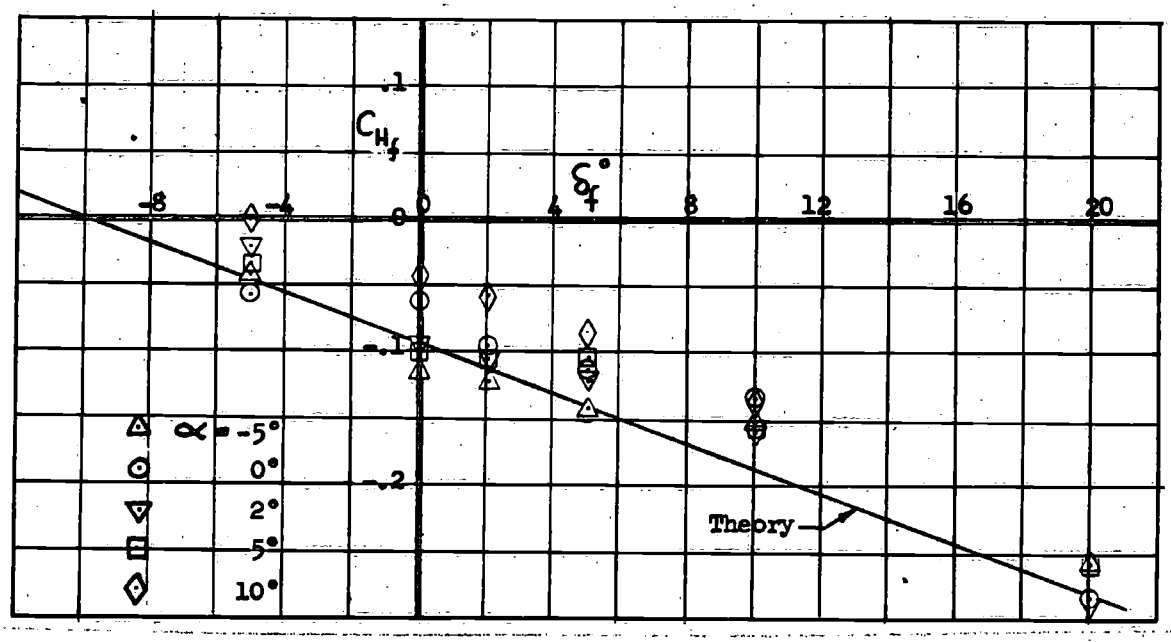

Figure 48. HINGE MOMENT COEFFICIENT - MODEL CONFIGURATION 1
$h/c = 1.0$, $c_f/c = 0.3$, $b_f/b = 0.6$

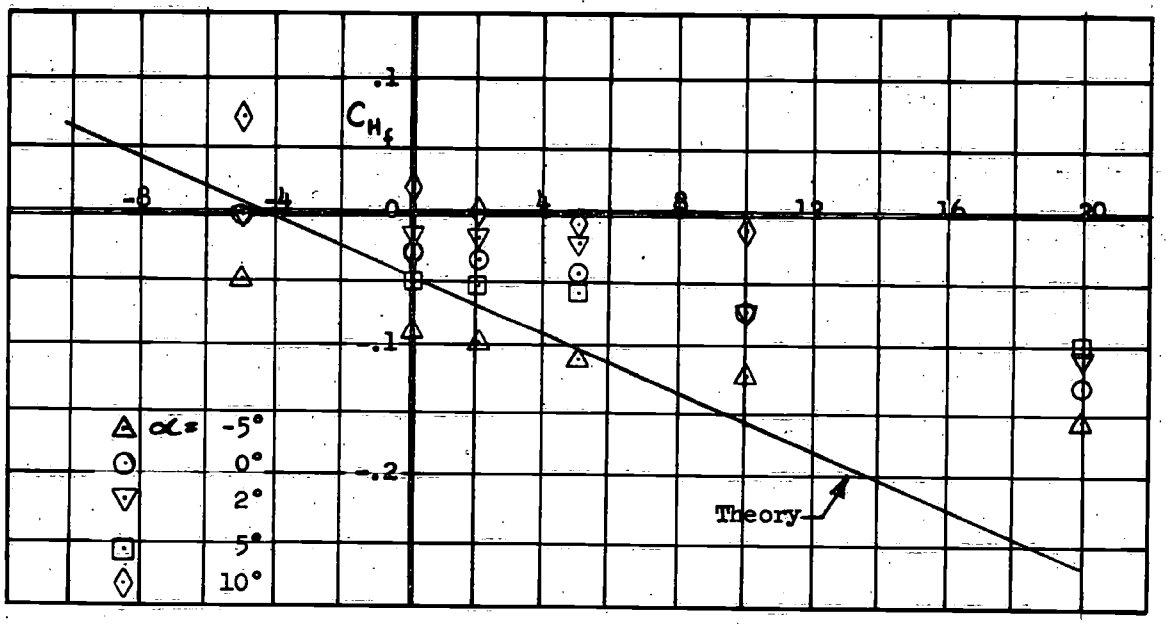

Figure 49. HINGE MOMENT COEFFICIENT - MODEL CONFIGURATION 3
$h/c = 1.0$, $c_f/c = 0.2$, $b_f/b = 0.6$

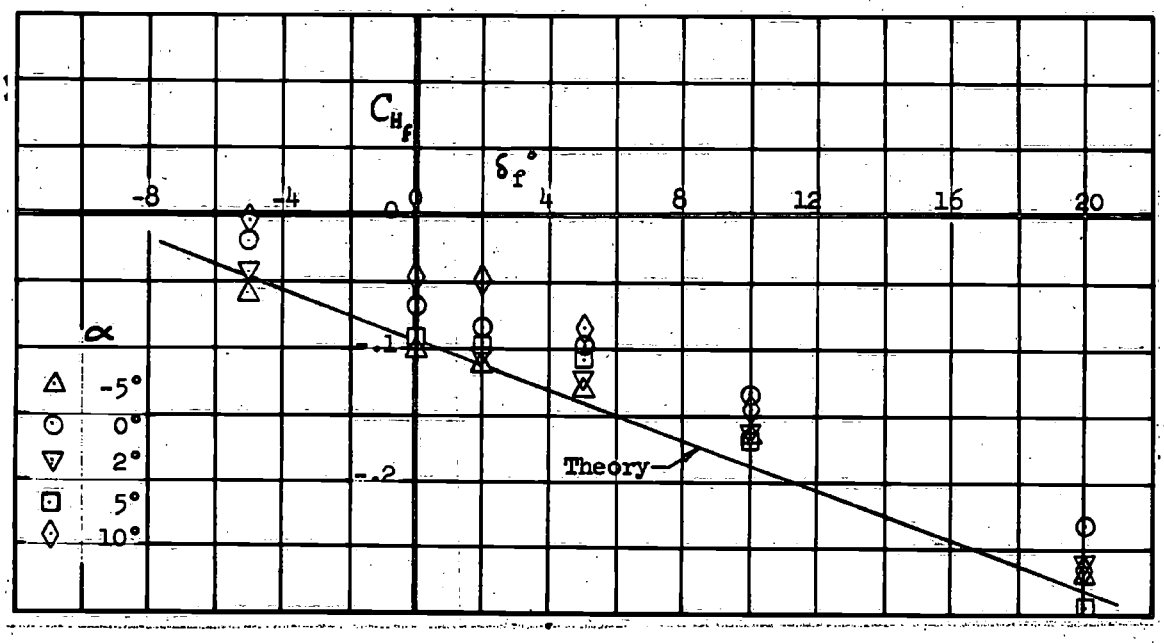

Figure 50. HINGE MOMENT COEFFICIENT - MODEL CONFIGURATION 2
$c_f/c = 0.3$, $b_f/b = 0.8$, $h/c = 1$

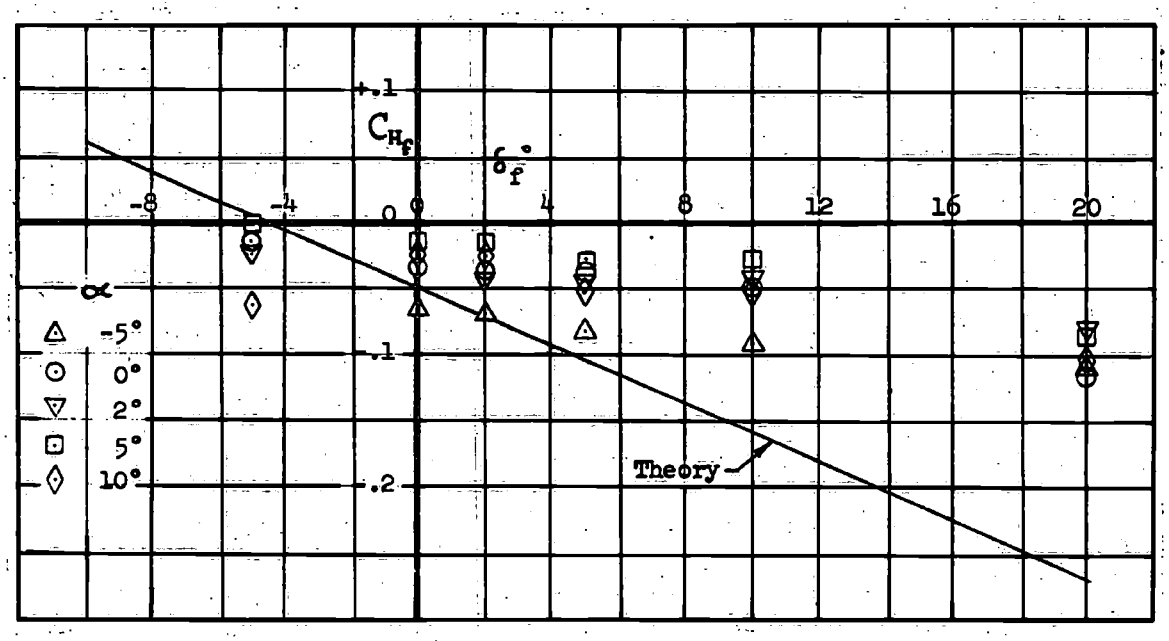

Figure 51. HINGE MOMENT COEFFICIENT - MODEL CONFIGURATION 4
$c_f/c = 0.2$, $b_f/b = 0.8$, $h/c = 1$

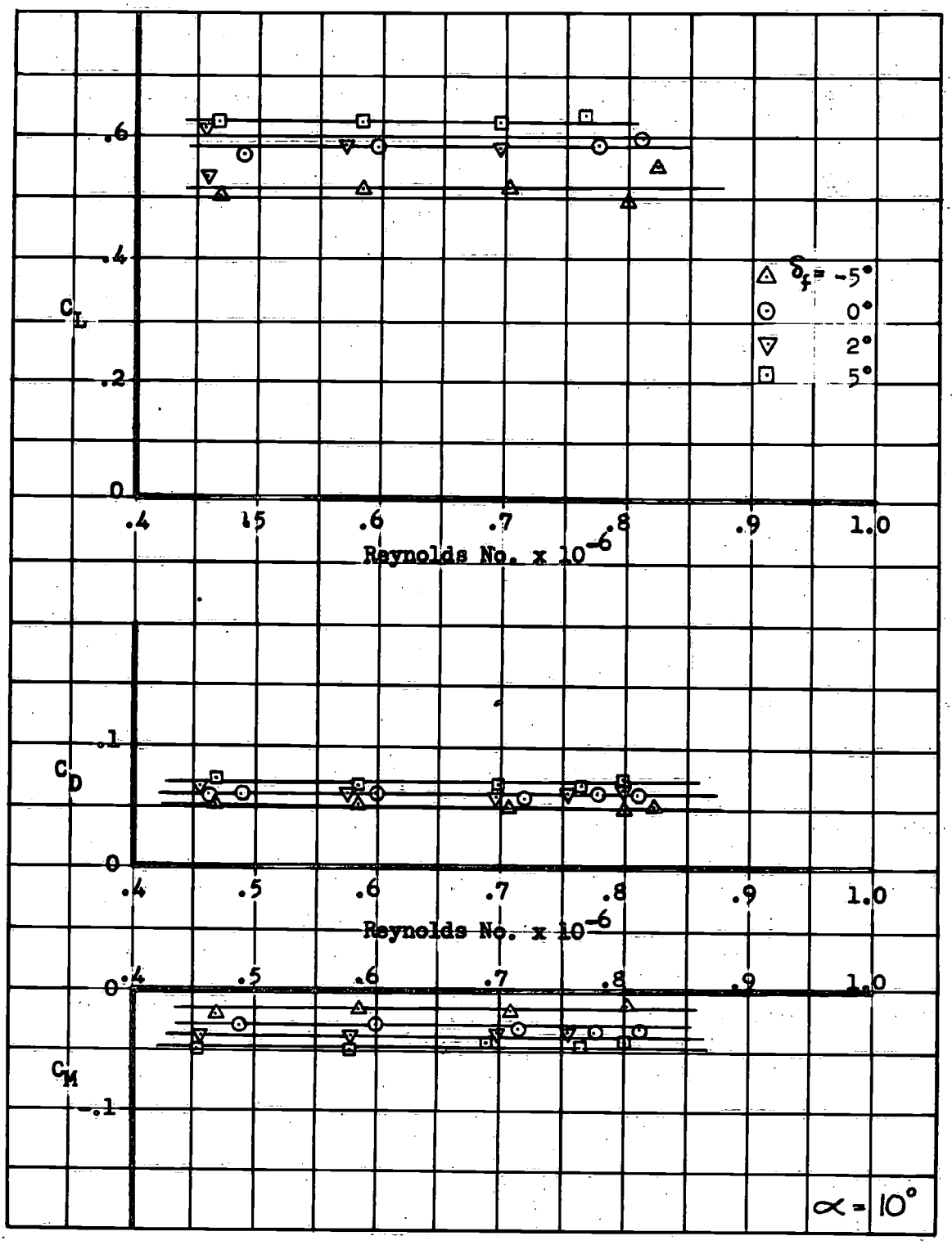

Figure 52. VARIATION OF COEFFICIENTS WITH SPEED

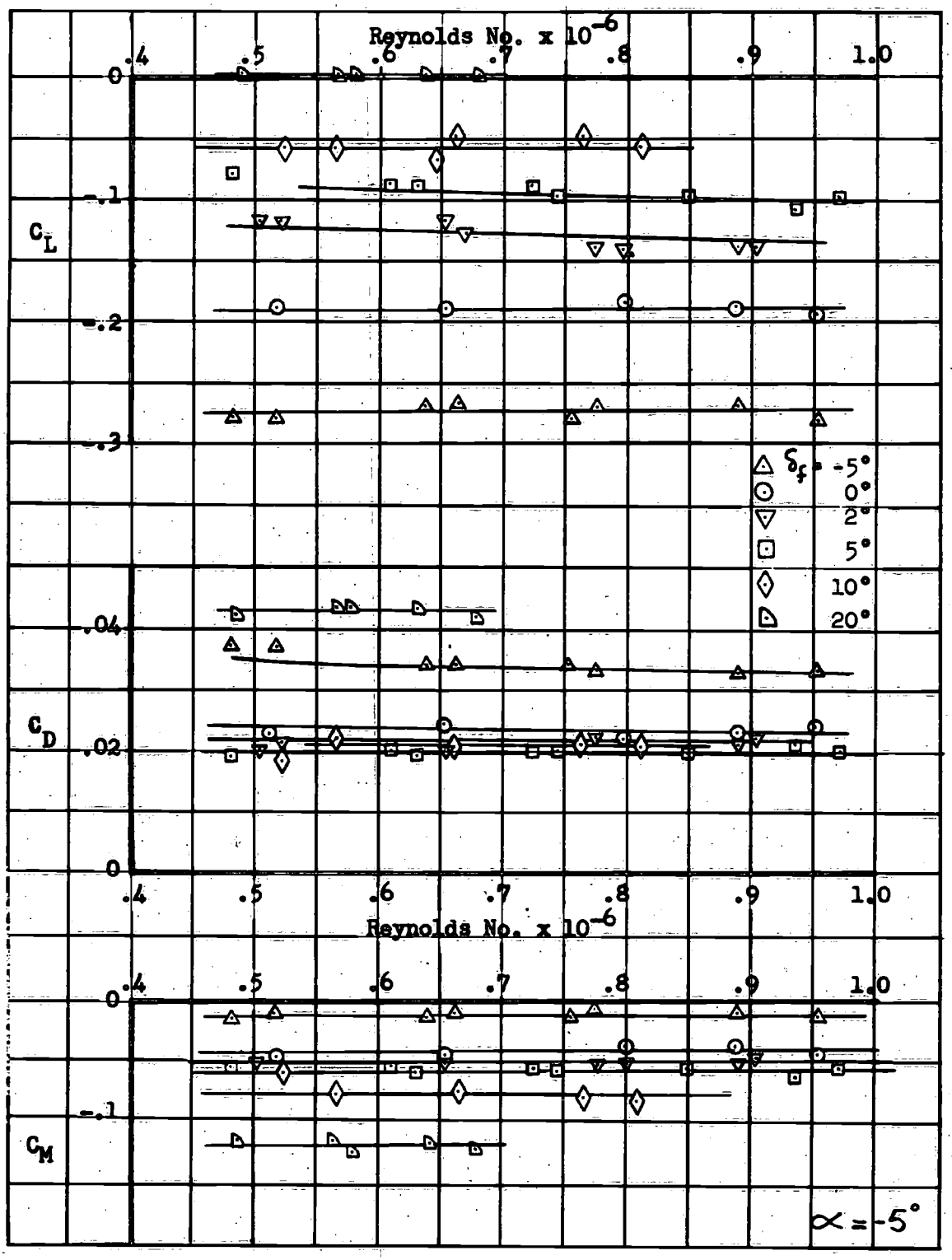

Figure 53. VARIATION OF COEFFICIENTS WITH SPEED

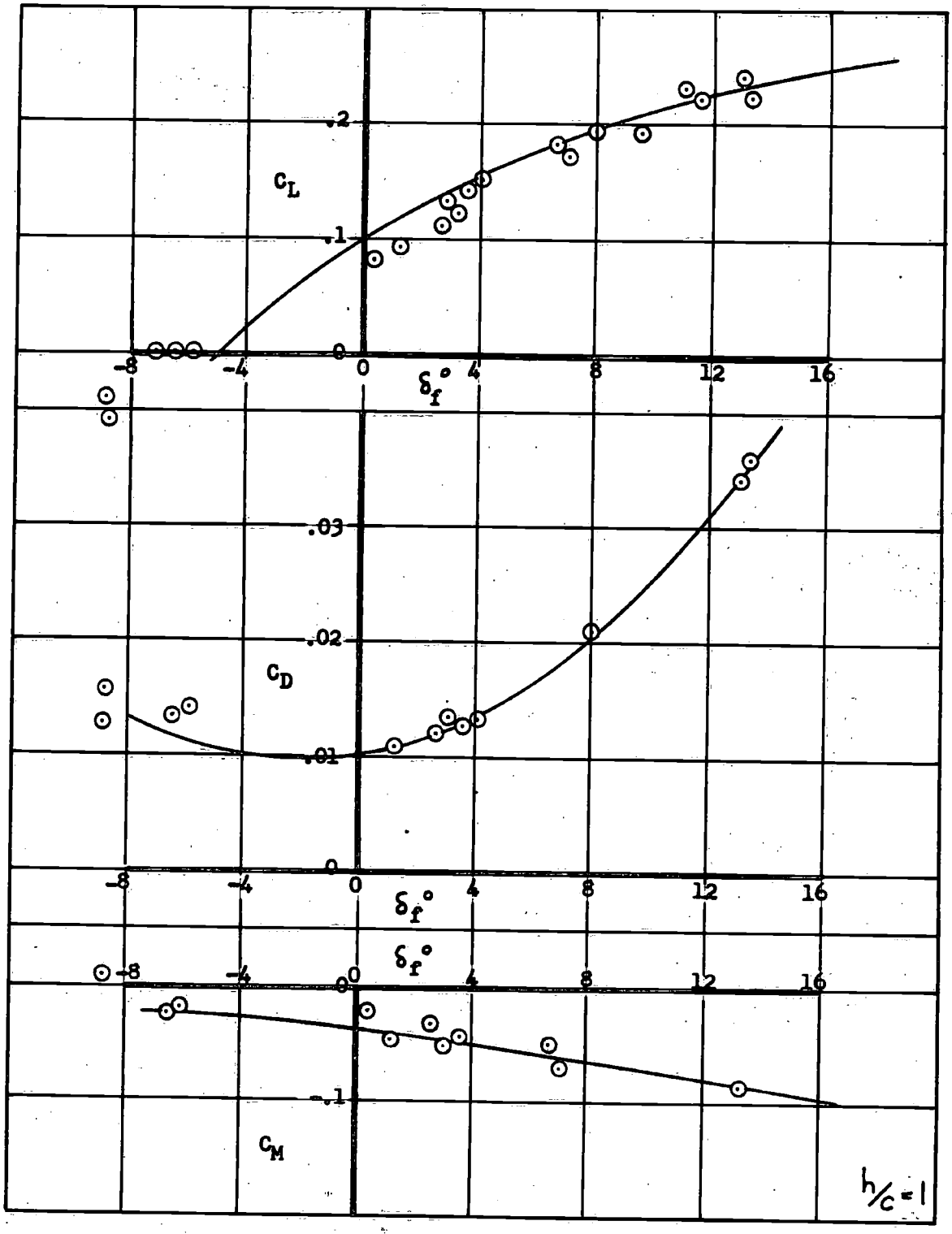

Figure 54. MODEL CONFIGURATION 1 - FLAPS CYCLED
FREQUENCY = 0.5 cps

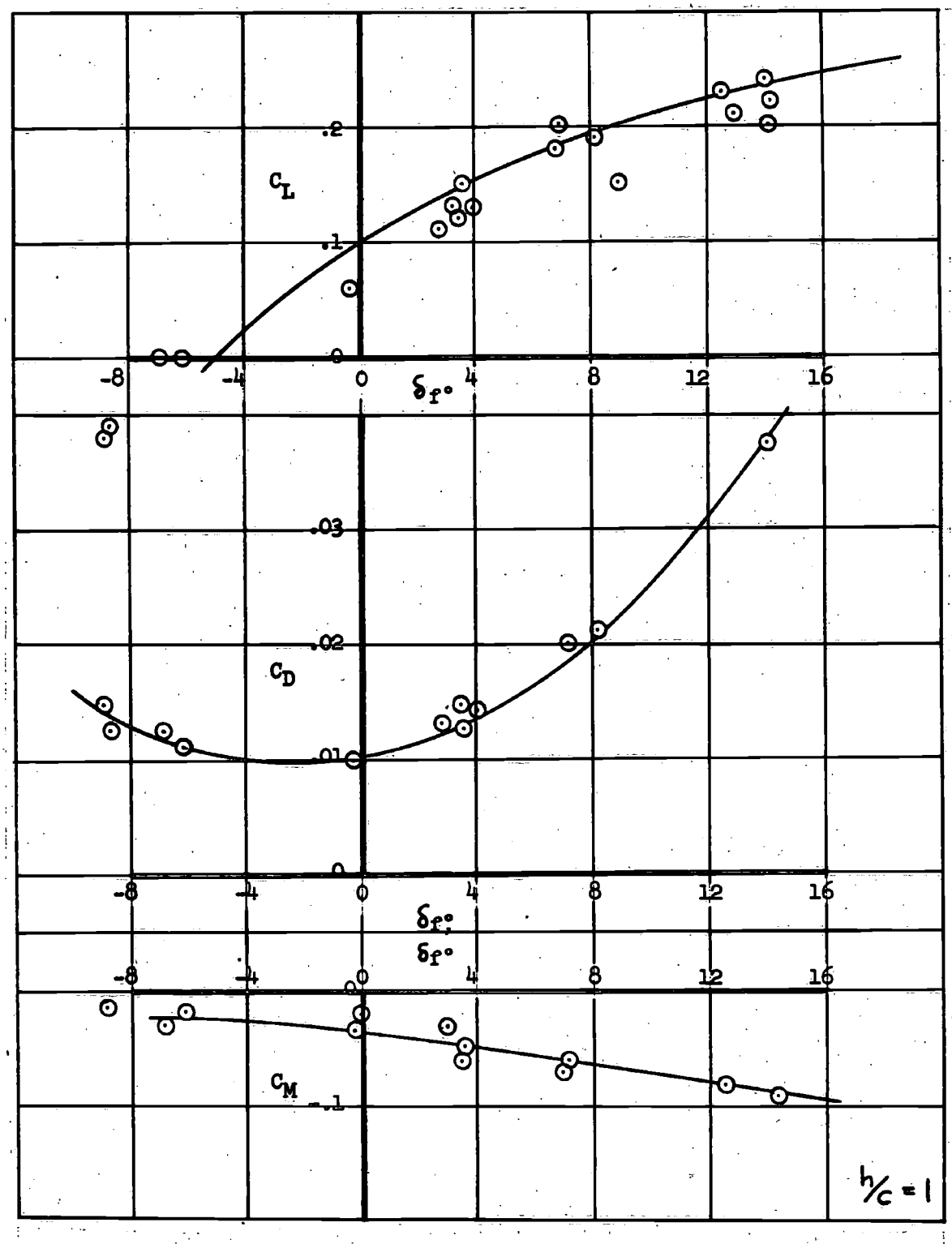

Figure 55. MODEL CONFIGURATION 1 - FLAPS CYCLED
FREQUENCY = 0.83 cps

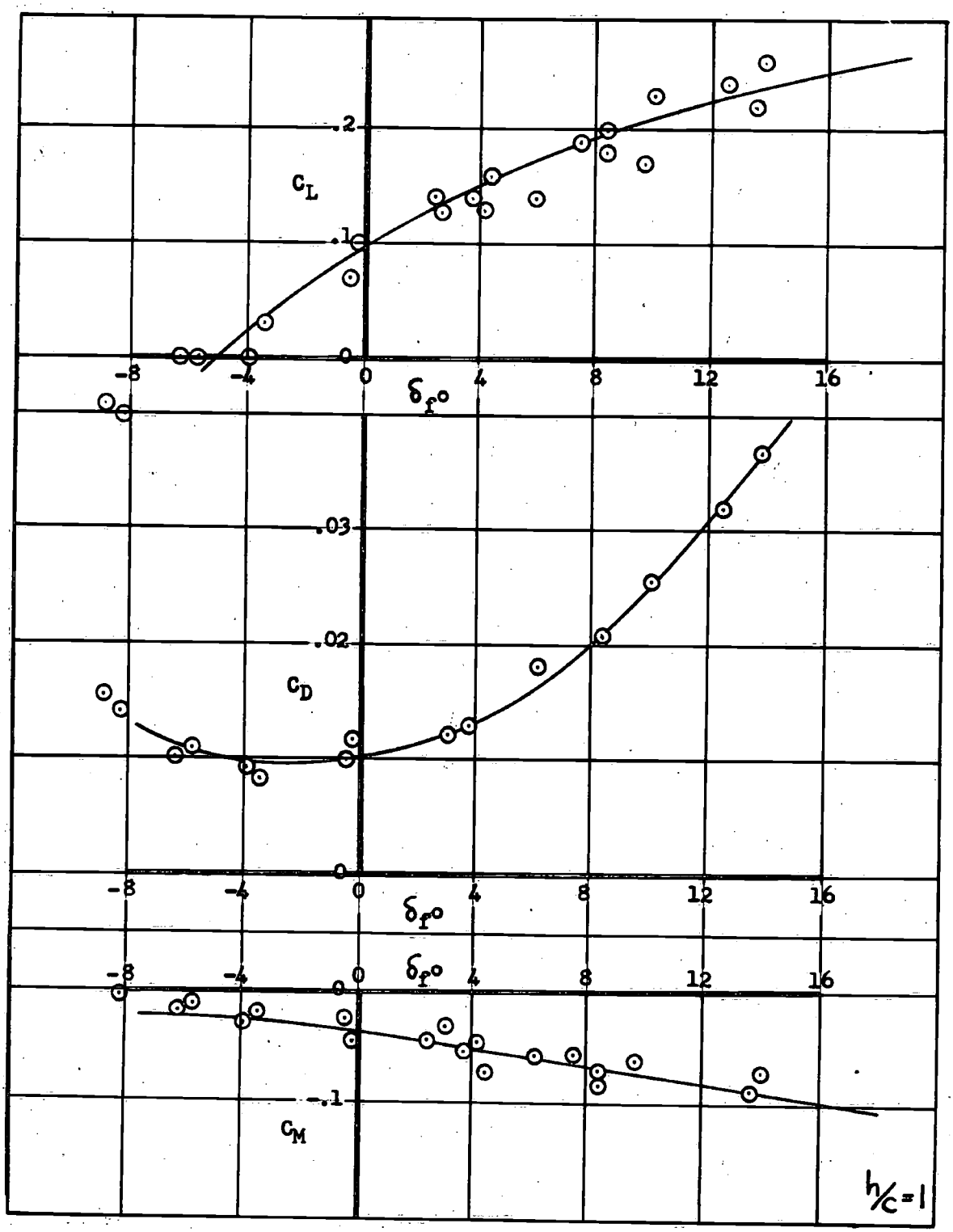

Figure 56. MODEL CONFIGURATION 1 - FLAPS CYCLED
FREQUENCY = 1.66 cps

Table I

DATA FOR MODEL CONFIGURATION 1

Flaps Fixed
Smooth Water
$c_f/c = 0.3$
$b_f/b = 0.6$
$h/c = 1.0$

α	δ_f	C_L	C_D	C_M	C_{L_f}	C_{D_f}	C_{H_f}
degrees							
-5	-5	-.270	.0329	-.010	-.03	.0305	-.042
	0	-.145	.0210	-.039	.13	.0015	-.115
	2	-.118	.0191	-.041	.18	.012	-.125
	5	-.088	.0190	-.053	.23	.026	-.142
	10	-.053	.0235	-.072	.27	.050	-.150
	20	+.003	.0433	-.1065	.42	.032	-.246
0	-5	.008	.0136	-.016	.025	.025	-.057
	0	.100	.0093	-.0345	.07	.010	-.059
	2	.125	.0102	-.039	.16	.013	-.093
	5	.157	.0147	-.056	.22	.0345	-.111
	10	.199	.0252	-.071	.30	.122	-.125
	20	.292	.0509	-.116	.43	.317	-.259
2	-5	.10	.0101	-.013	-.015	.046	-.021
	0	.205	.0099	-.042	.16	.0065	-.087
	2	.236	.0127	-.049	.23	.0265	-.114
	5	.274	.0180	-.054	.26	.031	-.121
	10	.327	.0295	-.068	.33	.108	-.156
	20	.399	.0567	-.114	.47	.036	-.276
5	-5	.262	.0170	-.0082	.04	.0325	-.034
	0	.36	.0226	-.0265	.21	.014	-.094
	2	.400	.0251	-.0335	.23	.026	-.100
	5	.450	.0307	-.044	.265	.050	-.105
	10	.485	.0418	-.0635	.335	.110	-.152
	20	.532	.0687	-.104	.49	.340	-.269
10	-5	.511	.0496	-.0075	.035	.030	-.002
	0	.570	.0553	-.0265	.13	.004	-.042
	2	.592	.0597	-.034	.17	.020	-.053
	5	.625	.0677	-.046	.21	.047	-.080
	10	.682	.0818	-.065	.31	.113	-.137
	20	.789	.1088	-.120	.49	.315	-.243

Table II

DATA FOR MODEL CONFIGURATION 2

Flaps Fixed
Smooth Water
$c_f/c = 0.3$
$b/b = 0.8$
$h/c = 1.0$

α	δ_f	C_L	C_D	C_M	C_{L_f}	C_{D_f}	C_{H_f}
degrees							
-5	-5	-.30	.0365	-.029	-.01	.0315	-.061
	0	-.18	.0199	-.050	.125	.002	-.095
	2	-.125	.0210	-.056	.21	.022	-.116
	5	-.07	.0191	-.059	.24	.028	-.130
	10	0	.0248	-.075	.33	.101	-.157
	20	+.085	.0522	-.112	.45	.384	-.250
0	-5	-	.0119	-.029	0	.028	-.057
	0	.10	.0104	-.0365	.16	.011	-.064
	2	.140	.0123	-.045	.215	.029	-.079
	5	.189	.0161	-.061	.29	.074	-.094
	10	.250	.0218	-.086	.36	.168	-.130
	20	.389	.0596	-.122	.535	.416	-.220
2	-5	.09	.0089	-.0075	0	.034	-.042
	0	.185	.0094	-.041	.16	.007	+.090
	2	.255	.0108	-.047	.25	.036	-.110
	5	.305	.0158	-.053	.33	.078	-.124
	10	.376	.0258	-.059	.34	.124	-.160
	20	.515	.0651	-.119	.525	.39	-.258
5	-5	.245	.0188	-.019	.015	.035	-.038
	0	.40	.0258	-.050	.21	.024	-.092
	2	.440	.0308	-.0545	.28	.054	-.098
	5	.470	.0338	-.057	.31	.068	-.098
	10	.544	.0474	-.088	.38	.146	-.162
	20	.671	.0956	-.146	.56	.438	-.276
10	-5	.481	.0580	-.007	.04	.021	-.005
	0	.572	.0628	-.014	.145	.005	-.043
	2	.613	.0667	+.025	.175	.021	-.055
	5	.655	.0748	-.050	.24	.047	-.080
	10	.742	.0976	-.092	.39	.156	-.150
	20	.863	.1356	-.146	.53	.363	-.258

Table III

DATA FOR MODEL CONFIGURATION 3

Flaps Fixed
Smooth Water
c_f/c = 0.2
b_f/b = 0.6
h/c = 1.0

α	δ_f	C_L	C_D	C_M	C_{L_f}	C_{D_f}	C_{H_f}
	degrees						
-5	-5	-.261	.0422	-.044	-.10	.038	-.052
	0	-.179	.0350	-.0455	.07	.003	-.090
	2	-.165	.0345	-.053			
	5	-.138	.0350	-.069	.195	.028	-.113
	10	-.119	.0384	-.0812	.25	.062	-.123
	20	-.058	.0409	-.083	.40	.213	-.158
0	-5	.028	.0129	-.008	-.085	.037	-.004
	0	.100	.0129	-.0256	.06	.033	-.032
	2	.111	.0149	-.034			
	5	.130	.0176	-.0483	.195	.010	-.037
	10	.166	.0210	-.0682	.335	.042	-.075
	20	.250	.0246	-.082	.50	.182	-.132
2	-5	.136	.0129	-.012	-.09	.031	-.005
	0	.196	.0129	-.0175	.015	.031	-.015
	2	.219	.0150	-.027			
	5	.256	.0193	-.0475	.25	.025	-.022
	10	.298	.0254	-.067	.375	.023	-.074
	20	.381	.0371	-.078	.555	.162	-.110
5	-5	.319	.0206	-.0217	-.035	.030	-.000
	0	.369	.0257	-.0344	.21	.033	-.051
	2	.387	.0259	-.041			
	5	.417	.0292	-.053	.27	.033	-.060
	10	.468	.0374	-.074	.42	.029	-.072
	20	.530	.0508	-.078	.56	.147	-.100
10	-5	.546	.0444	-.0258	-.04	.038	+.072
	0	.599	.0539	-.0304	.14	.032	+.020
	2	.612	.0557	-.036			
	5	.646	.0602	-.047	.25	.025	+.010
	10	.679	.0684	-.0638	.365	.025	-.010
	20	.761	.0851	-.089	.575	.108	-.110

Table IV

DATA FOR MODEL CONFIGURATION 4

Flaps Fixed
Smooth Water
$c_f/c = 0.2$
$b_f/b = 0.8$
$h/c = 1.0$

α	δ_f	C_L	C_D	C_M	C_{L_f}	C_{D_f}	C_{H_f}
degrees							
-5	-5	-.27	.0477	-.040	-.07	.035	-.056
	0	-.17	.0334	-.045	.115	.009	-.057
	2	-.15	.0340	-.058	.165	.017	-.077
	5	-.12	.0339	-.0738	.265	.057	-
	10	-.112	.0359	-.0864	.25	.056	-.095
	20	-.006	.0398	-.101	.47	.232	-.105
0	-5	.047	.0153	-.0294	.005	.029	-.017
	0	.10	.0144	-.037	.10	.021	-.032
	2	.121	.0166	-.0505	.215	.018	-.034
	5	.154	.0169	-.071	.26	.010	-.035
	10	.210	.0301	-.088	.425	.048	-.058
	20	.350	.0619	-.1085	.625	.222	-.112
2	-5	.129	.0139	-.0257	-.04	.034	-.020
	0	.205	.0134	-.044	.12	.021	-.031
	2	.240	.0187	-.065	.235	.010	-.035
	5	.284	.0211	-.076	.34	.018	-
	10	.330	.0261	-.0864	.44	.021	-.047
	20	.421	.0440	-.1073	.63	.199	-.083
5	-5	.277	.0186	-.0047	-.095	.027	-.002
	0	.350	.0228	-.031	.195	.013	-.010
	2	.378	.0253	-.044	.215	.012	-.023
	5	.412	.0298	-.0625	.29	.012	-.032
	10	.481	.0403	-.0775	.41	.066	-.055
	20	.596	.0615	-.0927	.645	.166	-.085
10	-5	.517	.0415	-.0022	-.065	.027	+.062
	0	.595	.0527	-.0215	.135	.023	-.018
	2	.615	.0528	-.033	.145	.025	-.034
	5	.641	.0618	-.057	.275	.026	-.045
	10	.711	.0731	-.0753	.42	.005	-.059
	20	.835	.0999	-.103	.625	.124	-.100

DISTRIBUTION LIST

Copies

3 Chief of Naval Research
Department of the Navy
Washington 25, D.C.
Attn: Code 438
1 Code 461

1 Commanding Officer
Office of Naval Research
Branch Office
495 Summer Street
Boston 10, Massachusetts

1 Commanding Officer
Office of Naval Research
Branch Office
346 Broadway
New York 13, New York

1 Commanding Officer
Office of Naval Research
Branch Office
1030 East Green Street
Pasadena, California

1 Commanding Officer
Office of Naval Research
Branch Office
1000 Geary Street
San Francisco 9, California

25 Commanding Officer
Office of Naval Research
Branch Office
Navy 100, Fleet Post Office
New York, New York

Copies

6 Director
Naval Research Laboratory
Washington 25, D.C.
Attn: Code 2027

Chief, Bureau of Naval Weapons
Department of the Navy
Washington 25, D.C.
1 Attn: Code RUAW-4
1 RRRE
1 RAAD
1 DIS-42

Chief, Bureau of Ships
Department of the Navy
Washington 25, D.C.
1 Attn: Codes 106
310
1 312
1 420
1 421
1 440
1 442
1 449

1 Chief, Bureau of Yards and Docks
Department of the Navy
Washington 25, D.C.
Attn: Code D-400

1 Commanding Officer and Director
David Taylor Model Basin
Washington 7, D.C.
1 Attn: Codes 142
1 500

1 Commanding Officer and Director
David Taylor Model Basin
Washington 7, D.C.
1 Attn: Codes 513
1 520
1 526A
1 530
1 533
1 580
1 585
1 591
1 591A

1 Commander
U.S. Naval Ordnance Test Station
Pasadena Annex
3202 E. Foothill Blvd
Pasadena 8, California

1 Commander
U.S. Naval Ordnance Test Station
China Lake, California
Attn: Code 753

1 Commander
Planning Department
Portsmouth Naval Shipyard
Portsmouth, New Hampshire

1 Commander
Planning Department
Boston Naval Shipyard
Boston 29, Massachusetts

1 Commander
Planning Department
Pearl Harbor Naval Shipyard
Navy 128, Fleet Post Office
San Francisco, California

1 Commander
Planning Department
San Francisco Naval Shipyard
San Francisco 24, California

1 Commander
Planning Department
Mare Island Naval Shipyard
Vallejo, California

1 Commander
Planning Department
New York Naval Shipyard
Brooklyn 1, New York

1 Commander
Planning Department
Puget Sound Naval Shipyard
Bremerton, Washington

1 Commander
Planning Department
Philadelphia Naval Shipyard
U.S. Naval Base
Philadelphia 12, Pennsylvania

1 Commander
Planning Department
Norfolk Naval Shipyard
Portsmouth, Virginia

1 Commander
Planning Department
Charleston Naval Shipyard
U.S. Naval Base
Charleston, South Carolina

1 Commander
Planning Department
Long Beach Naval Shipyard
Long Beach 2, California

1 Commander
Planning Department
U.S. Naval Weapons Laboratory
Dahlgren, Virginia

1 Dr. A. V. Hershey
Computation & Exterior Ballistics Laboratory
U.S. Naval Weapons Laboratory
Dahlgren, Virginia

1 Superintendent
U.S. Naval Academy
Annapolis, Maryland
Attn: Library

1 Superintendent
U.S. Naval Postgraduate School
Monterey, California

1 Commandant
U.S. Coast Guard
1300 E Street, N.W.
Washington, D.C.

1 Secretary Ship Structure Committee
U.S. Coast Guard Headquarters
1300 E Street, N.W.
Washington, D.C.

1 Commander
Military Sea Transportation Service
Department of the Navy
Washington 25, D.C.

U.S. Maritime Administration
GAO Building
441 G Street, N.W.
1 Attn: Division of Ship Design
1 Division of Research

1 Superintendent
U.S. Merchant Marine Academy
Kings Point, Long Island, New York
Attn: Capt. L.S. McCready (Dept of Engineering)

2 U.S. Army Transportation Research & Development Command
Fort Eustis, Virginia
Attn: Marine Transport Division

1 Director of Research
National Aeronautics and Space Administration
1512 H Street, N.W.
Washington 25, D.C.

2 J. B. Parkinson
National Aeronautics & Space Administration
Langley Aeronautical Laboratory
Langley Field, Virginia

1 Director
Engineering Sciences Division
National Science Foundation
1951 Constitution Avenue, N.W.
Washington 25, D.C.

Director
National Bureau of Standards
Washington 25, D.C.
Attn: Fluid Mechanics Division
1 (Dr. G. B. Schubauer)
1 Dr. G. H. Keulegan

10 Armed Services Technical Information Agency
Arlington Hall Station
Arlington 12, Virginia

1 Office of Technical Services
Department of Commerce
Washington 25, D.C.

California Institute of Technology
Pasadena 4, California
1 Attn: Professor M. S. Plesset
1 Prof. T. Y. Wu
1 Prof. A. J. Acosta

3 University of California
Berkeley 4, California
Attn: Division of Engineering

1 University of California
Department of Engineering
Los Angeles 24, California
Attn: Dr. A. Powell

1 Director
Scripps Institute of Oceanography
University of California
La Jolla, California

1 Professor M. L. Albertson
Department of Civil Engineering
Colorado A&M College
Fort Collins, Colorado

1 Professor J. E. Cermak
Department of Civil Engineering
Colorado State University
Fort Collins, Colorado

1 Professor W. R. Sears
Graduate School of Aeronautical
Engineering
Cornell University
Ithaca, New York

3 State University of Iowa
Iowa Institute of Hydraulic Research
Iowa City, Iowa

Harvard University
Cambridge 38, Massachusetts
1 Attn: Prof. G. Birkhoff (Dept of
Mathematics)
1 Prof. G. F. Carrier (Dept
of Mathematics)

Massachusetts Institute of
Technology
Cambridge 39, Massachusetts
1 Attn: Department of Naval
Architecture and Marine
Engineering
1 Prof. A. T. Ippen

University of Michigan
Ann Arbor, Michigan
2 Attn: Prof. R. B. Couch (Dept of
Naval Architecture)
1 Prof. W. W. Willmarth
(Aero Engr Department)
1 Prof. M. S. Uberoi
(Aero Engr Department)

1 Dr. L. G. Straub, Director
St. Anthony Falls Hydraulic
Laboratory
University of Minnesota
Minneapolis 14, Minnesota

1 Professor J. J. Foody
Engineering Department
New York State University
Maritime College
Fort Schulyer, New York

New York University
Institute of Mathematical Sciences
25 Waverly Place
New York 3, New York
1 Attn: Prof. J. Keller
1 Prof. J. J. Stoker
1 Prof. R. Kraichnan

The Johns Hopkins University
Department of Mechanical Engineering
Baltimore 18, Maryland
1 Attn: Prof. S. Corrsin
2 Prof. O. M. Phillips

1 Massachusetts Institute of Technology
Department of Naval Architecture and Marine Engineering
Cambridge 39, Massachusetts
Attn: Prof. M. A. Abkowitz, Head

1 Dr. G. F. Wislicenus
Ordnance Research Laboratory
Pennsylvania State University
University Park, Pennsylvania

1 Professor R. C. DiPrima
Department of Mathematics
Rensselaer Polytechnic Institute
Troy, New York

Stevens Institute of Technology
Davidson Laboratory
Castle Point Station
Hoboken, New Jersey
1 Attn: Prof. E. V. Lewis
1 D. Savitsky

1 Webb Institute of Naval Architecture
Crescent Beach Road
Glen Cove, New York
Attn: Technical Library

1 Director
Woods Hole Oceanographic Institute
Woods Hole, Massachusetts

Hamburgische Schiffbau-Versuchsanstalt
Bramfelder Strasse 164
Hamburg 33, Germany
1 Attn: Dr. O. Grim
1 Dr. H. W. Lerbs

1 Institut für Schiffbau der Universität Hamburg
Berliner Tor 21
Hamburg 1, Germany
Attn: Prof. G. P. Weinblum, Director

1 Max-Planck Institut für Strömungsforschung
Bottingerstrasse 6/8
Göttingen, Germany

1 Hydro-og Aerodynamisk Laboratorium
Lyngby, Denmark
Attn: Prof. Carl Prohaska

1 Skipsmodelltanken
Trondheim, Norway
Attn: Prof. J. K. Lunde

1 Versuchsanstalt für Wasserbau and Schiffbau
Schleuseninsel im Tiergarten
Berlin, Germany

1 Technische Hogeschool
Institut voor Toegepaste Wiskunde
Julianalaan 132
Delft, Netherlands
Attn: Prof. R. Timman

1 Bureau D'Analyse et de Recherche
Appliquees
2 Rue Joseph Sansboeuf
Paris 8, France
Attn: Prof. L. Malavard

1 Netherlands Ship Model Basin
Wageningen, Netherlands
Attn: Dr. Ir. J. D. van Manen

1 Allied Research Associates, Inc.
43 Leon Street
Boston 15, Massachusetts
Attn: Dr. T. R. Goodman

1 General Dynamics/Convair
San Diego 12, California
Attn: R. H. Oversmith

1 Dynamic Developments Inc.
Midway Avenue
Babylon, New York
Attn: W. P. Carl

1 Dr. S. F. Hoerner
148 Busteed Drive
Midland Park, New Jersey

1 Hydronautics, Incorporated
200 Monroe Street
Rockville, Maryland
Attn: Phillip Eisenberg

1 Rand Development Corporation
13600 Deise Avenue
Cleveland 10, Ohio
Attn: Dr. A. S. Iberall

1 U.S. Rubber Company
Research and Development
Department
Wayne, New Jersey
Attn: L. M. White

Technical Research Group, Inc.
2 Aerial Way
Syosset, Long Island, New York
1 Attn: Jack Kotik
Dr. Paul Kaplan

1 C. Wigley
Flat 102
6-9 Charterhouse Square
London, E.C.1, England

1 AVCO Corporation
Lycoming Division
1701 K Street, N.W.
Apt 904
Washington, D.C.
Attn: T. A. Duncan

1 Mr. J. G. Baker
Baker Manufacturing Company
Evansvile, Wisconsin

1 Curtiss-Wright Corporation
Research Division
Turbomachinery Division
Quehanna, Pennsylvania
Attn: George H. Pedersen

1 Hughes Tool Company
Aircraft Division
Culver City, California
Attn: M. S. Harned

2 National Research Council
Montreal Road
Ottawa 2, Canada
Attn: E. S. Turner

1 The RAND Corporation
1700 Main Street
Santa Monica, California
Attn: Blaine Parkin

1 Stanford University
Department of Civil Engineering
Stanford, California
Attn: Dr. Byrne Perry

1 Waste King Corporation
5550 Harbor Street
Los Angeles 22, California
Attn: Dr. A. Schneider

1 Lockheed Aircraft Corporation
California Division
Hydrodynamics Research
Burbank, California
Attn: Kenneth E. Hodge